Silicon thin film transistor based on PbS nano-particles : an efficient phototransistor for the detection of infrared light

Xiang Liu

ANNÉE (2016)

THÈSE / UNIVERSITÉ DE RENNES 1
sous le sceau de l'Université Bretagne Loire

en Cotutelle Internationale avec
UNIVERSITÉ du SUD-EST (SOUTHEAST UNIVERSITY), NANJING, CHINE

pour le grade de

DOCTEUR DE L'UNIVERSITÉ DE RENNES 1

Mention : (Electronique)

Ecole doctorale (MATISSE)

présentée par

Xiang LIU

préparée à l'unité de recherche IETR- UMR CNRS 6164
Institut d'Electronique et de Télécommunication de Rennes
UFR Informatique – Electronique
et au Display Center, School of Electronic Science and Engineering,
Southeast University

Intitulé de la thèse :
Transistor silicium en couche mince à base de nano-particules de PbS : Un efficace phototransistor pour la détection de lumière infrarouge.

Thèse soutenue à Nanjing (Chine)
le 27 décembre 2016

devant le jury composé de :

Olivier DURAND
Professeur, INSA Rennes / *rapporteur*

Li LI
Professeur, Nanjing University of Science and Technology, Chine / *rapporteur*

Emmanuel JACQUES
Maître de Conférences, Université Rennes 1 / *examinateur*

Qing LI
Professeur, South-East University Nanjing, Chine / *examinateur*

Wei LEI
Professeur, South-East University Nanjing, Chine / co-*directeur de thèse*

Tayeb MOHAMMED-BRAHIM
Professeur Université Rennes 1 / *directeur de thèse*

Table of Content

Introduction

This thesis is realized in the framework of a collaboration between the Institute of Electronics and Telecommunications of Rennes (IETR) and Display Research Center of Southeast University. The topic of this thesis is to integrate the low-dimensional material Quantum dots (QDs) into Thin Fim Transistors (TFTs) which can be used as Near-Infrared (NIR) photodetectors.

Nowadays, the photodetectors are the key technology in many application fields as opto-communication, sensor touch panel, IR imaging and navigation. However, for the conventional photodetectors such as photoconductors and photodiodes, complicated peripheral circuits are needed for the signal output, signal synchronous and connection with the display pixel. Self-amplification by transistors can simplify the future design for photo-electric systems where transistors are used as phototransistors.

The present work uses the well known low-temperature-poly-silicon (LTPS) thin film transistor to fabricate phototransistors thanks to the integration of QDs in the gate insulator. This integration is possible thanks to the use of organic solution deposited insulator. The purpose of the work is to combine nanoscience and TFTs to fabricate phototransistors with excellent electrical performance, highly sensitive optical-electrical conversion and quick response to pulsed photo-signals. The thesis is organized as follows:

(1) Firstly, the state-of-the-art of the photodetectors will be presented with special attention to broaden IR photodetectors. Afterward the photodetecting mechanism and important parameters are introduced in deep. Finally, the novel phototransistors with self-amplifying properties and signal self-output capabilities are illustrated and reviewed in detail.

(2) Afterwards, the technological process of common planar top-gate TFT that is chosen to fabricate the future FET-based phototransistor, is described. The deposition technologies for the LTPS TFTs' active layer are introduced. Except for the undoped poly-silicon active layer, the N doped and P-doped contact layer will also be detailed

which can determine the type of the TFTs. Afterwards, the important gate insulator deposition technologies are described where the inorganic SiO_2 and organic SU8 insulator are utilized to verify the performance of this LTPS TFT respectively. Particularly, the SU8 insulator is mainly studied to explore the electrical properties of the future phototransistors.

(3) In order to broaden the detecting wavelengths of this phototransistor, PbS QDs were synthesized to blend SU8 organic solution insulator. The quality and characters of PbS QDs were characterized by the typical material properties measurements such as Tunneling Electron Microscope (TEM), Scanning Electron Microscope (SEM), Vis-NIR absorbance, X-ray Diffraction (XRD), and Energy Dispersive Spectrometer (EDS). PbS QDs show 1.4 μm centered absorption band, strong absorbance and uniform dispersion in SU8 solution. Effective charges transfer between QDs and SU8 insulator was proven also.

(4) Since incorporation of QDs influences the insulating quality of SU8 that will act as gate insulator, Metal-mixed QDs-SU8 insulator-Semiconductor (MIS) structure devices with different QDs' concentration were fabricated and characterized. The purpose was to find the maximum QDs concentration (leading to high sensitivity) compatible with acceptable gate insulator quality. Optimum concentration was found to be 2.5 mg/ml QDs that can combine excellent electrical performance and efficient optical-electrical conversion Finally, photo-Thin Film Transistors using SU8 embedded with PbS QDs as gate insulator ware fabricated and characterized from electrical properties, sensing sensitivity and answer time points of view.

Chapter 1 Quantum dots based NIR Phototransistor: application and fabrication

1. Introduction

Photodetectors become now the core of the optical communication technology, which is the important foundation industry of the future informatics society [1-6]. The rising of the Nano technology aroused the interest of the researchers: when the size of solid reduced to a certain dimension, which is the critical physic dimension of certain information carrier (or elementary excitation), emerging problems occur such as quantum confinement effect and coherence [7-10]. The Nano-optoelectronic is the science to research the generation, the conversion, the amplification and the capture of photonics and electronics in nanosized materials [11, 12]. It is the interdisciplinary science combining Nano-technology and photonics, which create many new phenomena and materials [13, 14], for example, photonic crystals [15, 16], Quantum dots (QDs) [17, 18], negative reflective index [19, 20] and so on. Thus, this technology broadens the physics depth and application range.

One of particular interest is the devices working in Infrared (IR) wavelength band that are the main subject of present PhD thesis. These devices are used in a large range of applications: IR imaging [21, 22], remote sensing [23, 24], communication [25] and navigation [26].

Conventional IR photodetectors need higher lattice match up, higher material consumption, complex array connection of the different components. Envisaging all these disadvantages, the new colloidal quantum dots were involved due to a unique material property which attracted many focuses, for example bandgap's continually tunable, sensitive to vertical incident light and non-lattice match up [27-30]. Meanwhile, the fabrication's superiority for QD provide a possibility to use easy technology such as spin-coating, hot spray, printing, to deposit thin film and roll-to-roll process on the flexible substrate by large-scale processes.

Finally, the Field-Effect Transistor (FET) structure was brought in photodetector to overcome the drawbacks for instance, excitons' rapid annihilation and weak photo-

current gain in device [31, 32]. Besides, this FET structure can possess higher gain, responsivity and excellent signal-noise ratio with extra signal amplifying functions, which also can be easily integrated in the Nano-micro-level optical-electrical circuits [33, 34]. Through importing QDs into FET structure photodetectors, the QDs based phototransistors will be obtained, which defy those difficulties and obstacles in traditional photodetectors' fabrication, such as complex connection process, rigor processing circumstance, unachievable large-scale process and incompatible to flexible substrate. The emerge of phototransistors has a substantial realistic significance for the acquisition of high performance photodetectors with integrated optical-electrical circuits.

2. State-of-the-arts of Infrared photodetector

Scientists have done many researches on the detection and application of the electromagnetic wave at IR regions. The development roadmap for IR photodetector is depicted in figure 1.1 [35].

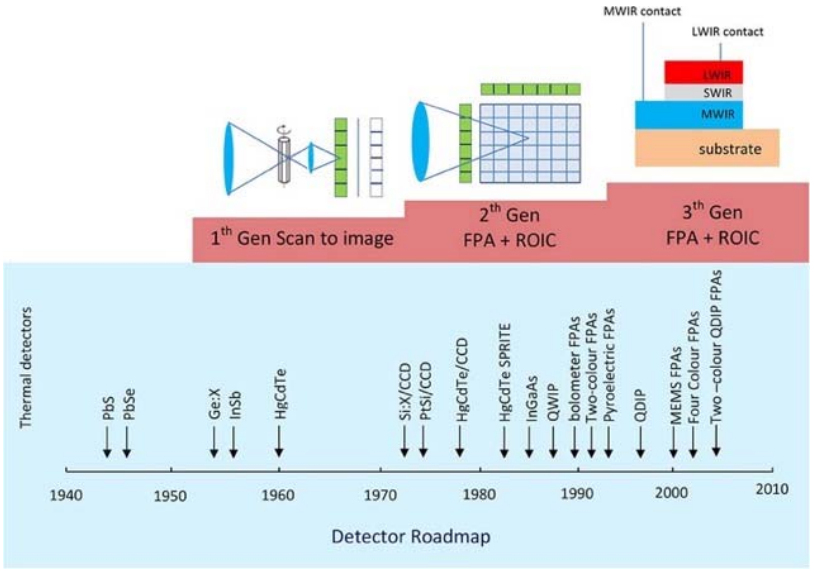

Figure 1.1 The IR photodetectors and the systems' development roadmap [35]

From 1940s to present, the IR photodetectors have experienced three generations' developments. The first generation photodetectors are the traditional simple photodiodes utilized III-V, IV-VI and II-VI compound semiconductor alloy material.

The second generation photodetectors are the Charge-coupled Device (CCD) detecting arrays with some high efficiency infrared materials such as InSb, HgCdTe and PtSi. Nowadays, the emphasis of the research is put on the research on third generation focal plane (FPA) photodetectors' material and device from "bandgap engineering" to promote device's capability and lower down the cost.

Though there are plenty of photodetecting materials for IR waveband, the real appropriate material possessing flexible wavelength-tunable ability is not so many. Presently, the main materials and the structures are conventional HgCdTe [35-38], quantum well photodetectors (QWIP) [39-44], type II strained-layer superlattices (SLS) [45-48] and quantum dot photodetectors (QDIP) [49-53]. Herein, the HgCdTe, QWIP, strained-layer superlattices and of course the novel type QDIP are introduced in this chapter.

2.1 HdCdTe Infrared photodetector

Figure 1.2 illustrate the schematic and SEM image of the two-color HgCdTe detector pixel [35]. Because of the realization of the dual and multi-colors photodetectors are difficult, it must create dual or multi vacuum chambers and cool down systems. Thus to settle this problem, the introduced two-color HdCdTe infrared photodetectors are fabricated with one stack structure separated by the shared electrode.

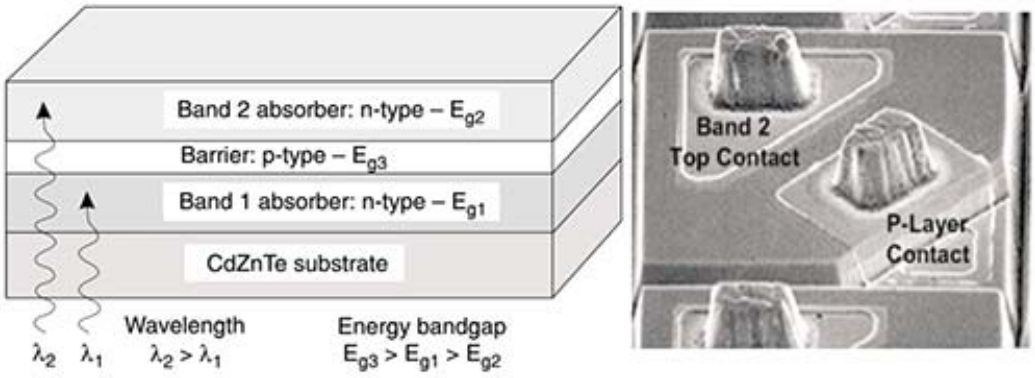

Figure 1.2 HgCdTe two-colour detector pixel's structure schematic and the SEM image of the pixels [36].

The anisotropic dry etching was used to grow the three-layer HgCdTe structure. This HgCdTe photodetector has three advantages [37, 38]: (1) The absorbance range shifts from 1-30 μ m by adjusting the content of Cd in this alloy; (2) Intrinsic absorbance provide high quantum efficiency for photodetectors. (3) It has high carrier lifetime. Vacuum epitaxy technology is often used to fabricate high quality HgCdTe IR photo-electrical thin film. Herein, the molecular beam epitaxy (MBE) and metal organic chemical vapor deposition (MOCVD) are the two frequently used vacuum deposition technology. Though HgCdTe material is of many virtues, the heavy and expensive vacuum systems, huge surface leakage current and other fatal problems determined that it is impossible to integrate it in the large-area photodetectors.

2.2 Quantum well Infrared photodetector

Quantum well photodetector is composed of two different semiconductor materials and in opposite arrangement. A quantum well is a potential well with only discrete energy values. The electron's transition theory in energy level of quantum well explains the IR radiation detection in a wavelength range that can cover 6-20 μ m [39].

In 2014, M. Oehme and D. Widmann fabricate by epitaxy GeSn/Ge multi-quantum well photodetector on the Si substrate [40]. MBE semiconductor growth system was used on the Si substrate. Different annealing steps form the multi-layer MQW photodetectors with tensile strain in the Ge buried layer. By adopting this technology, this solution can break the limitation of the critical epitaxial layer thickness.

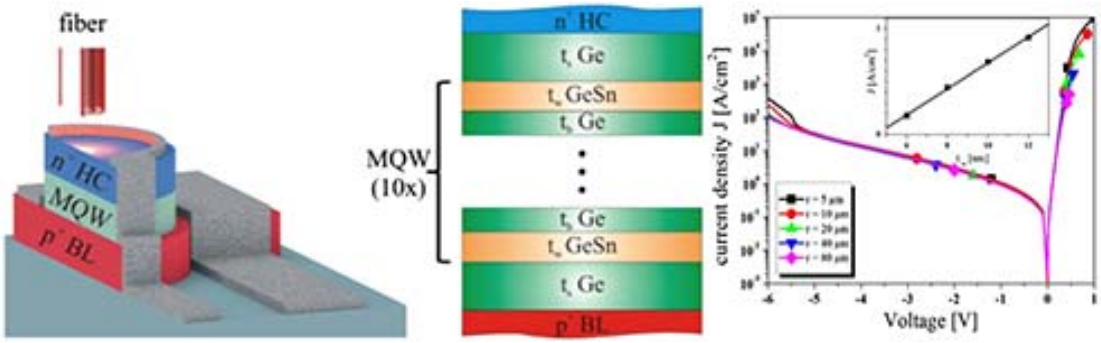

Figure 1.3 Schematic cross section of a GeSn Multi-layer Quantum Well

photodetector and the IV curve of this MQW photodetectors [40].

Quantum well has excellent IR photodetecting performance, but the zero-absorbance toward the vertical light create a complex fabrication process to produce photonic grating in view of augmenting the absorption of the device [41-44], which increase the cost and difficulties.

2.3 Strained superlattices Infrared photodetector

Type-II SLS Infrared photodetectrors have some unique optical-electrical performances [45], which is becoming the developing direction of the three generation FPA device.

Figure 1.4 shows the schematic of the strained superlattices IR phtotodetector as reported in 2010 by J. B. Rodriguez and E. Plis [46]. As illustrated in the bandgap alignment, the InAs/GaSb has a straddle structure bandgap, and with the type-II SLS material, it demonstrated promising results with excellent optical-electrical properties.

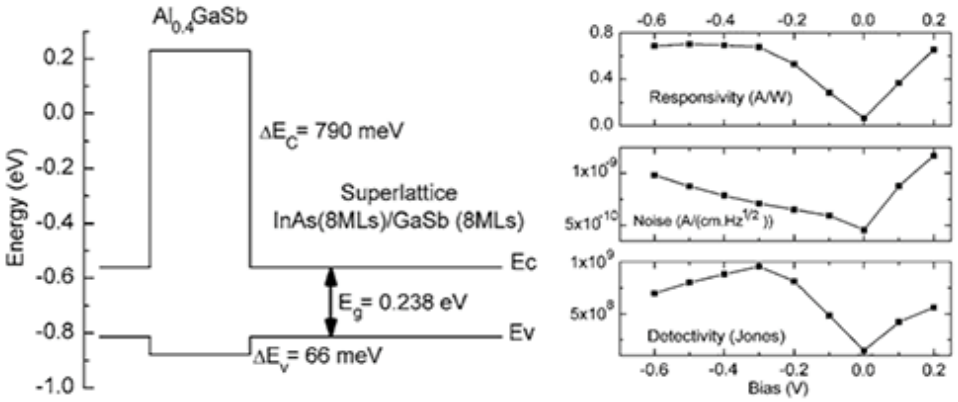

Figure 1.4 Heterostructure schematic of the nBn structure along with the calculated offsets and the optical-electrical parameters verse applied bias.

However, even if SLS photodetector has well IR sensitive properties, the high quality thin film's growth and the passivation of thin film are hard to realize [47, 48], which are the biggest challenge for the fabrication processes.

2.4 Quantum dots Infrared photodetector

The above HgCdTe, QWIP and SLS materials based third generation photodetector has excellent IR sensitive characters. However, the drawbacks are obvious particularly with the use of expensive MBE and MOCVD techniques. QDIP has advantages, such as sensitivity to vertical incident light, high responsivity, high detectivity, tunable detecting wavelengths and low-temperature fabrication. Figure 1.5 shows the structure of the most popular QDIP 10 years ago [49, 50]. This QDIP is focused on the heterostructure with QW embedded with QDs (DWELL, Dot in a well). With DWELL heterostructure, photodetectors combined the features of QWIP and QDIP, which leads to high responsivity and other electrical performance, as shown in figure 1.4. Nevertheless, the fabrication process is hard to reach obtain size-tunable, morphology-controllable QDs' material, which also needs complex instruments and expensive experimental conditions.

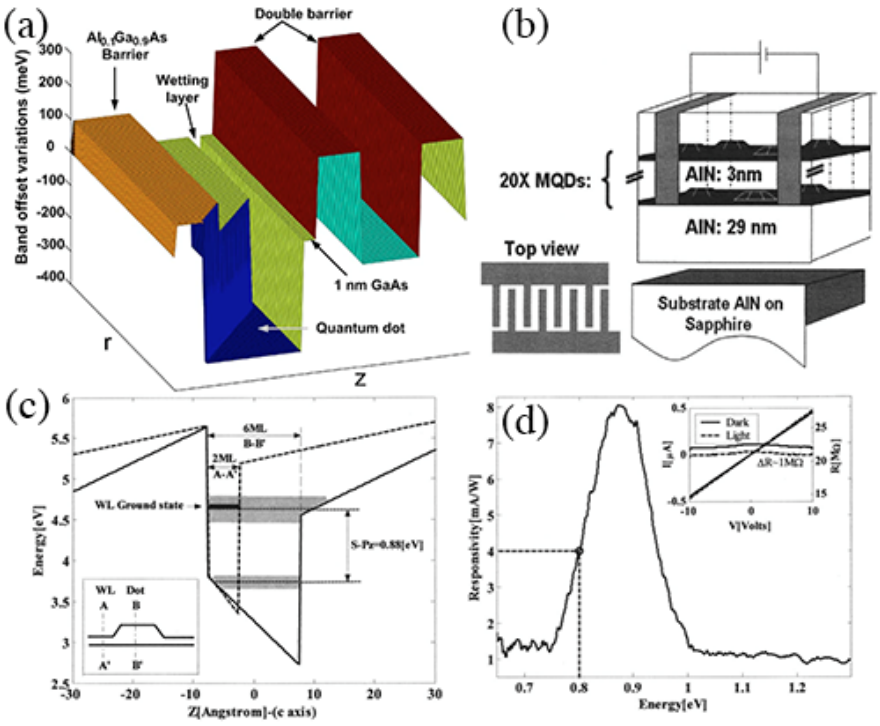

Figure 1.5 Model (a) and device structure (b) of QDIP device. (c) Bandgap diagram showing the carrier transport. (d) Electrical performance of this QDIP. [49, 50]

After that, the research on the QDs sandwiched structure photodetector got the

attention of the scientific field. Figure 1.6 illustrated the InP QDs fabricated by low-temperature MOCVD process. Through this process, the size of the QDs can be controlled by adjusting the conditions of the synthesis. Moreover, the stability, reproducibility and device performance benefit from this structure and fabrication process. But the disadvantage of this QDIP is that fabrication process can not form a thick QDs layer; annealing process can not provide a continuous and uniform QDs layer; and of course the synthesis temperature is too high (the temperature of the reaction is 500-590 ℃) for any flexible substrate.

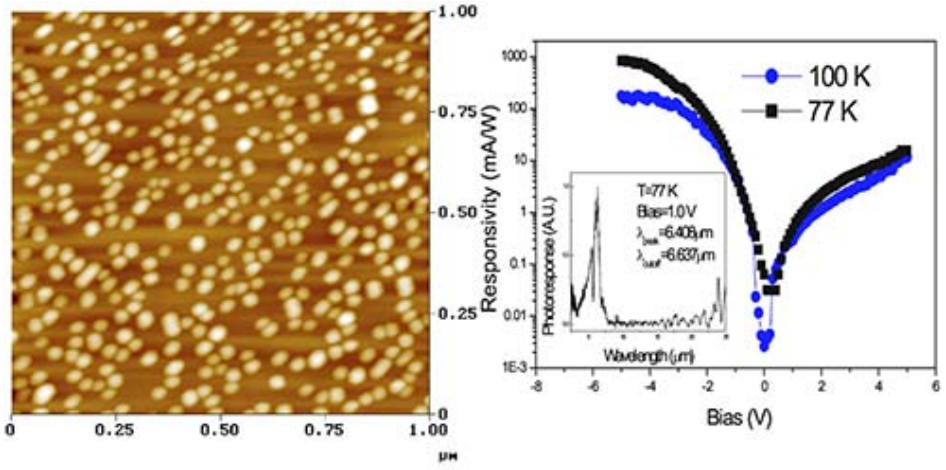

Figure 1.6 Atomic force microscopy image of a single layer of InAs quantum dots on the GaAs/InP matrix and the responsivity as a function of bias for the QDIP at 77 and 100k. The inset image is the spectrum of the surface at 1V bias [51].

Colloidal QDs' jumped the drawbacks of the previous MBE and LP-MOCVD high temperature processes. The chemical synthesis method has many classifications, which can be applied in QDs' size control, chemical components and morphology. These synthesis technologies can produce high-quality, narrow-distribution, uniform morphology QDs. The low-temperature solution-process such as spin-coated, hot-spray and printing technologies can fabricate large-scale thin film in all the substrate. It can be transferred to other CMOS, MOSFET and other optical-electrical technologies with high performance in flexible substrate.

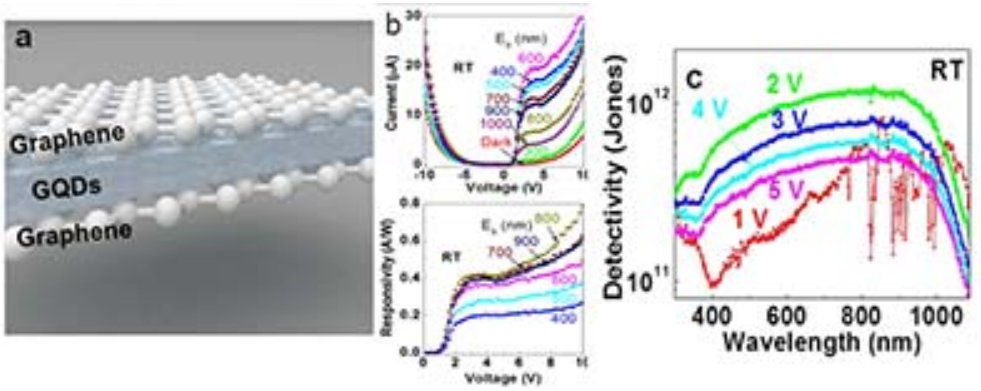

Figure 1.7 (a) Device schematic of the GQDs' graphene sandwiched photodetector's structure. (b) The photocurrent and responsivity of this photodetectror. (c) The detectivity of the photodetectors under different wavelengths [52].

C. O. Kim and S. W. Hwang produced graphene/QDs/graphene sandwiched photodetector at 2014 [52] which possesses high photocurrent, QE and detectivity. With all the low-dimension materials, this photodetector benefits from the quantum confinement effect and unique optical-electrical properties. But this diode structure device doesn't have amplification mechanism, which cause the responsivity and photoelectrical conversion very low. Thus some other nano-technology process are adopted to promote the device's performance. Figure 1.8 shows the QDIP with bulleye's nano-stucture [53]. With this nano-structure in the photodetector, surface plasmon phenomenon around the nano-structure can increase absorption of the diode to promote the photocurrent and responsivity. However, the diode structure QDIP still limit the photosensitivity and responsivity without intrinsic amplifying function. In spite that nanotechnology can enhance the light absorption, the disadvantages such as complicated process, experimental cost and incompatible to large-scale process, will hinder the device's photodetecting application.

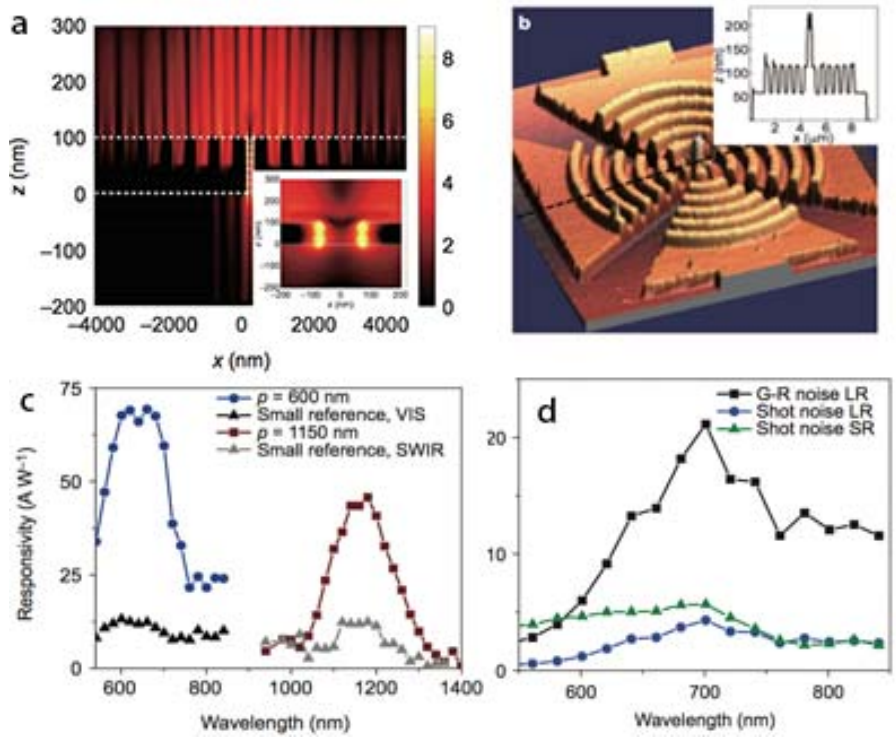

Figure 1.8 (a) Simulated absorption enhancement in a nanovolume of PbS QDs in the center. (b) 3D atomic force micrograph of the nanostructure. (c) Responsivity of this GQDs' photodetector with different wavelengths. (d) Detectivity enhancement variation verse the IR wavelengths [53].

3. Theory and mechanism of photodetection

3.1 The theory of photoconductivity

Photoconductivity is the phenomenon that the semiconductor's conductivity increases under illumination, which is the photodetection mechanism. Figure 1.9 shows the schematic of photoconductivity with the two terminals ohmic contacts device. This chapter will introduce the theory of the photoconductivity in semiconductors [54-57].

If we assume a photon flux (number of photons par area unit and per time unit) Φ_0 arriving on the sample of Figure 1.8, each absorbed photon leads to η free electrons (η is the quantum efficiency), the number of carriers in excess at the surface Δn_S is given by the equality between the flux of carriers in excess and the flux of arriving photons:

$$\frac{\Delta n_S}{\tau} = \eta \Phi_0 \qquad (cm^{-2}\, s^{-1})$$

where τ is the lifetime of the carriers in excess

If we consider a uniform absorption of photons on the thickness t of the sample, the bulk carriers concentration in excess is given by $\Delta n = \frac{\Delta n_S}{t} = \frac{\eta \tau \Phi_0}{t}$

Under the electrical field V/L due to applied bias V, the current density J_L due to these carriers in excess is: $J_L = \Delta n\, e\mu \frac{V}{L}$

The excess current I_L due to these excess electrons is then given by:

$$I_L = \eta e \mu \tau \frac{W}{L} \Phi_0 V \qquad (1.7)$$

where e is the electron charge, μ the mobility of the free carriers, τ their lifetime of the free carriers and V the applied bias between the electrodes.

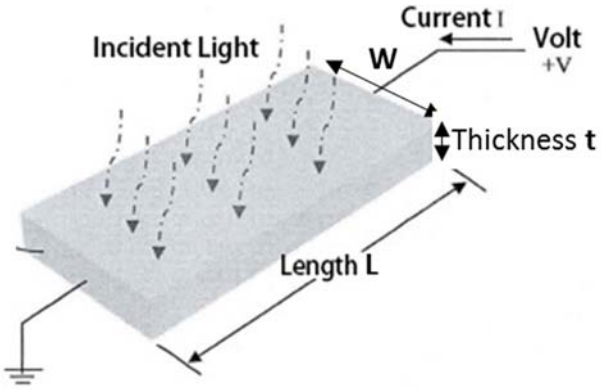

Figure 1.9 Schematic of photoconductivity

3.2 The main parameters of a photodetector

A photodetector has a series of performance parameters, such as responsivity, gain, noise and response time. These parameters determined the quality of the photodetector performance [57, 58]. In this chapter, the photodetector performance parameters are introduced as following:

(1) Responsivity

The responsivity R_P of the detector is its ability to convert an incident light power P_{inc} into a current I_L. It is given by the ratio between these two quantities:

$$R_p = \frac{I_L}{P_{inc}}$$

Taking the example of the sample of Figure 1.8, the incident power is given by:

$$P_{inc} = h\upsilon\, \Phi_0 W t$$

The responsivity is then given by:

$$R_p = \eta \frac{\mu\tau}{L^2} \frac{V}{h\nu/e} \quad (A/W)$$

Present expression shows that the answer of the photodetector depends a lot on the mobility-lifetime product (μτ). It is the only parameter that depends on the intrinsic properties of the photoconducting material.

Responsivity can be written also as : $R_p = \eta g \frac{1}{h\nu/e}$

Where g is the gain of the photodetector. It is given by: $g = \frac{\tau}{\tau_{tr}}$

Where τ_{tr} is the transit time of carriers between the 2 electrodes. It is given by: $\tau_{tr} = \frac{L}{\mu E}$.

Usually the value of the gain g is on the order of 10^5.

The expression of the responsivity as a function of the gain g depends on the photon energy hν. It can be also written as a function of the wavelength λ knowing that

$$h\nu\ (eV) = \frac{\lambda\ (\mu m)}{1.24}$$

The new expression of the responsivity $R_p = \eta g \frac{\lambda\ (\mu m)}{1.24}$ shows a linear variation of the responsivity with the wavelength λ.

Actually, the efficiency η is depending on the absorbance coefficient α and incident light's wavelength. For the practical light photodetector, the long wavelength's cutoff edge is depending on the absorbance edge and energy bandgap of the photoconducting material. The short wave absorbance edge is depending on the material's absorption coefficient and device's structure.

(2) Detectivity

. The detectivity of a photodetector characterize its ability to detect very weak light power or its ability to extract the signal coming from the light absorption from the noise.

Remembering the expression of the photocurrent $I_L=R_PP_{inc}$ and knowing that generally the noise is given by the square root of the product of the current without light I_0 by the pass-band B ($\sqrt{2eI_0B}$), a Noise Equivalent Power (NEP) is defined as the light power inducing a photocurrent equal to the noise current.

$$NEP = \frac{\sqrt{2eI_0B}}{R_P}$$

NEP parameter depends on the photodetector (through I_0 and R_P) but also on its size (through I_0) the measurement system (through B). It does not characterize the photodetector material only.

Another more specific parameter, the detectivity D is then defined by $D = \frac{\sqrt{AB}}{NEP}$ where A is the area of the detector. Then the final expression of the detectivity is written:

$$D = \frac{R_P}{\sqrt{2eJ_0}} \qquad (cmHz^{1/2}W^{-1}\ or\ Jones)$$

where J_0 is the current density under dark.

(3) Response speed

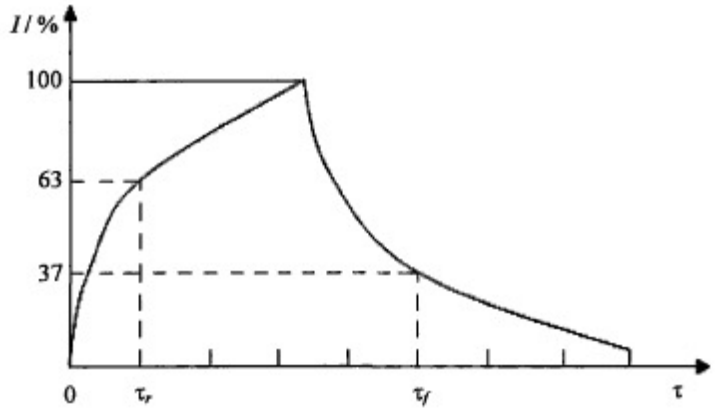

Figure 1.10 The rising time and decay curve of photocurrent

The rising and decreasing time determined the response speed, as shown in figure 1.10. From the semiconductor's theory, the generation and recombination of carriers in photoconductors follow the index variation. When the illumination stops, the time of photocurrent's recovery to the stable photocurrent I/e is called time constant.

4. Main Photodetectors

4.1 Photoconductors

Photoconductors is the device using above introduced theory of the photoconductivity. The most common-used device is the photo-resistor, which is the light-modulated variable resistor. The resistance of a photoresistor decreases with increasing incident light intensity which exhibits photoconductivity. The merits of this device are: the intrinsic photo-electric effect has no relationship with electrode (photodiode usually works when is added reversed applied bias [51]), which can be used in alternating current (AC) source; the photosensitivity is related with semiconductor material and incident light wavelength. However, the photoconductor's performance will be affected a lot by the external temperature and be of very slow response time (from ms to s level) [59].

4.2 Photodiode

In fact, the photodiode's structure is similar to the usual semiconductor diode. The only difference is that photodiode has the photosensing region exposed under the light source to detect light signal. The most popular photodiodes are Schottky diodes [60], p-i-n diodes [61] and avalanche photodiodes [62]. The photodiodes have so many advantages which have gotten widespread research and use in the photodetecting applications. For example, photodiodes have well linearity, quick response time, wide response region (190 nm- 850 nm, Si), low cost, long lifetime and don't need high voltage source. But the structure of photodiode has fatal drawbacks, such as without intrinsic amplifying mechanisms, very low responsivity and so on.

4.2 Phototransistor

Thanks to the field effect, phototransistors can convert absorbed light into a variation of the current with high efficiency even if the absorption coefficient is not so high. Figure 1.11 provides the device schematic of the phototransistor used as

photodetectors, which has similar structure to the usual MOSFET but with the different photosensing materials for gate insulator or active layer. Indeed, under light absorption, the potential at the channel-gate insulator interface changes leading to a modulation of the drain-source current. The effect is equivalent to the important effect on the drain-source current induced by a small variation of the gate voltage. A review of this type of device used as photodetectors is given in the next paragraph.

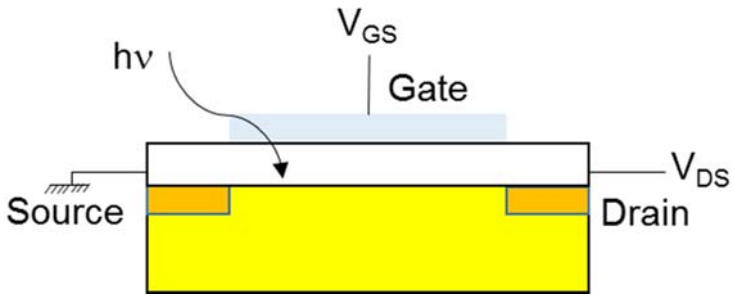

Figure 1.11 The schematic diagram for the typical FET structure phototransistor.

5. Reviews of phototransistors

Phototransistors are a family of photodetectors that have in common a self-amplification. Apart bipolar silicon phototransistor where the light is absorbed in the base region, increasing the base current and then using the amplification of this current to get high sensitivity, the other phototransistors are based on MOS technology and use the field effect imposed by the gate bias to increase the sensitivity. In this last family, the principle of the photo-detection itself changes from an absorption inside the active layer (channel) to an absorption inside photosensitive materials such as quantum dots. Here a brief review of the main MOS phototransistors is given.

5.1 Silicon-based MOS phototransistor

Due to the weak absorption coefficient of single crystalline silicon in visible light, silicon based phototransistors have been developed in bipolar technology. In MOS technology, phototransistors are based on higher absorption coefficient silicon or

silicon alloys as hydrogenated amorphous silicon or silicon-germanium alloy.

Recently, numerous studies have been reported on the α-Si:H and SiGe:H active layer phototransistors. In 2015, Y. Lee and I. Omkaram achieved one α-Si:H phototransistor in Near-Infrared regime. As shown in figure 1.12, this phototransistor has a high response in the visible-NIR wavelength range with a quick response time at 0.1ps. This device can be integrated easily in future sensing/display application.

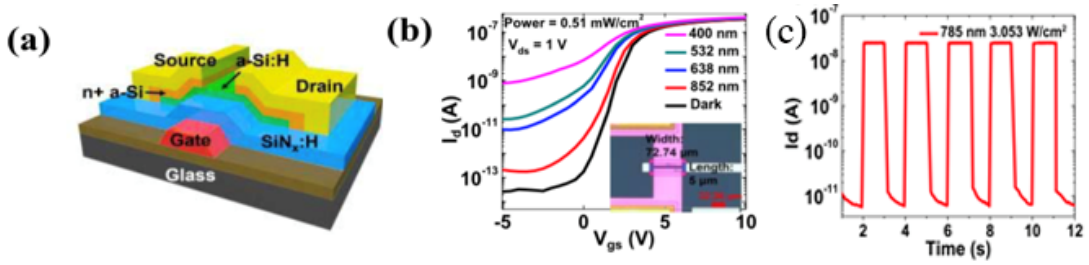

Figure 1.12 Phototransistor with α-Si:H active layer channel, transfer characteristics IV curves under different wavelength and the current response toward the incident IR light [63].

Another possibility was the use of nanostructured silicon. With the confinement of the light in silicon nanowire, the absorption is increased largely. Figure 1.13 shows a suspended silicon nanobridge phototransistor which was fabricated and reported in 2014. Meanwhile, by using this phototransistor, a logic circuit was fabricated to extract the light pulsed signal. This research work provides an option to use the nanobridge structure and easy logic circuits to constitute future photo-modulated switching microelectronic chip.

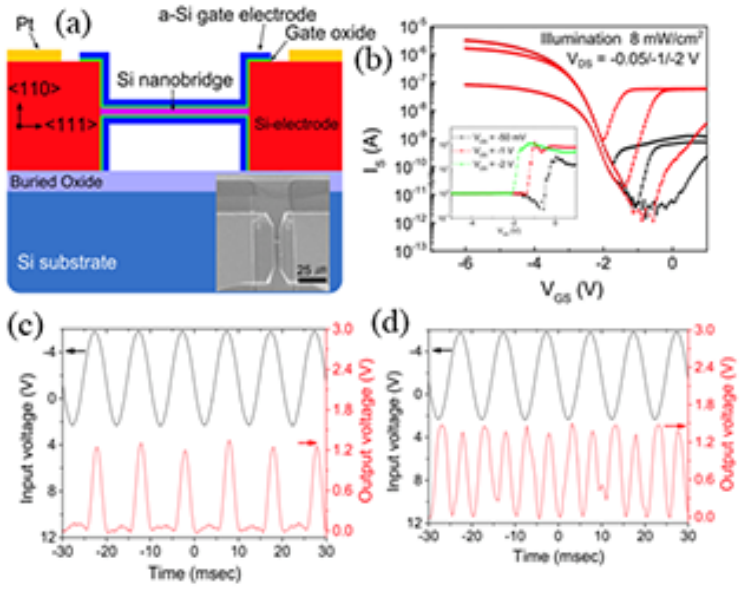

Figure 1.13 (a) The silicon nanobridge TFT's device structure. (b) The transfer IV characteristic of this TFT under illumination. The output signal without (c) and with (d) light [64].

Different other structures of FET were proposed in the purpose to increase the photo-sensitivity. For example, lastly on 2016 Chi Zhang and Zhao Hua Zhang proposed a triboelectric field-effect phototransistor, which is illustrated in the figure 1.14.

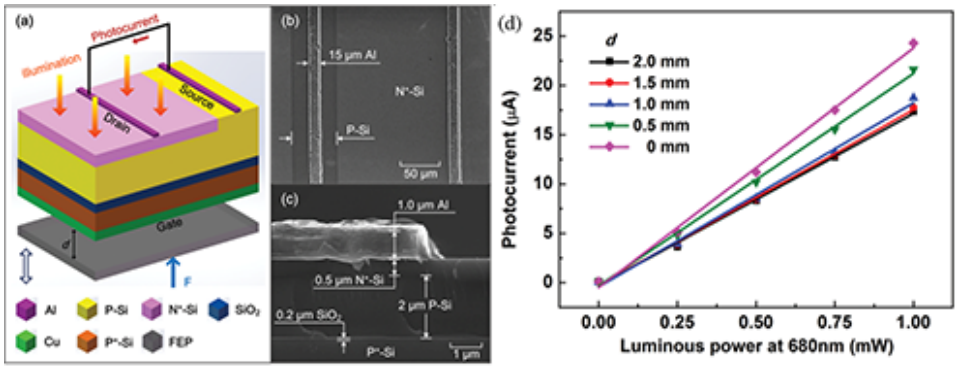

Figure 1.14 The structure of the Nano-structure NPN TFT and the photocurrent under red light [65].

5.2 Oxide-base phototransistors

Due to their highest absorption and largest band-gap, oxide materials are alternative options when wide detecting wavelength range is needed. Figure 1.15

demonstrate the highly-sensitive phototransistor with IZO/IGZO hybrid active layer by the researchers [66]. In this hybrid IZO/IGZO materials' photosensing active layer system, IZO is the photo-sensitive component while IGZO is the electrical semiconductor to transfer current from drain to source. Compared with amorphous silicon material, IZO material has a high absorption coefficient and high mobility to generate large photocurrent for photodetection.

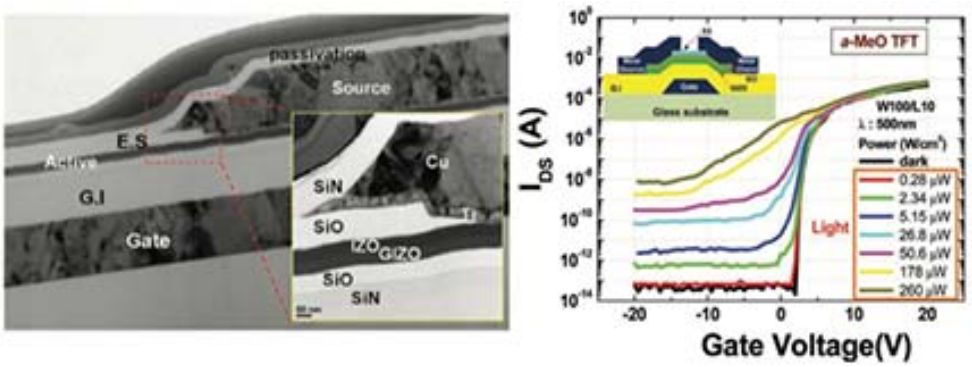

Figure 1.15 Metal-oxide thin film phototransistor' structure and transfer curves under visible incident light [66].

Figure 1.16 are the images of the IGZO/IZO phototransistor which is integrated in to the remote sensor for the touch panel. Due to the photoconductivity effect (PPC) of Zinc-related materials, the rising time and decay time of the device is very high which will influence the application in the future high frequency devices and quick detecting/imaging systems. In figure 1.16, S. Jeon and S. –E. Ahn use the gate pulse signal as resting Synchronization signal to diminish the recovery time of the device. But the slow response of the oxide-based phototransistor is still the biggest drawback for this oxide-based TFT, since we need complicated synchronization signal control circuit as peripheral circuit. Meanwhile, due to the wide-bandgap semiconductor nature of ZnO, the detecting wavelength range is limited in the visible and UV wavelength. These intrinsic drawbacks of Oxide materials presented here indicate that Oxide-based materials maybe are not the ideal choice for phototransistor.

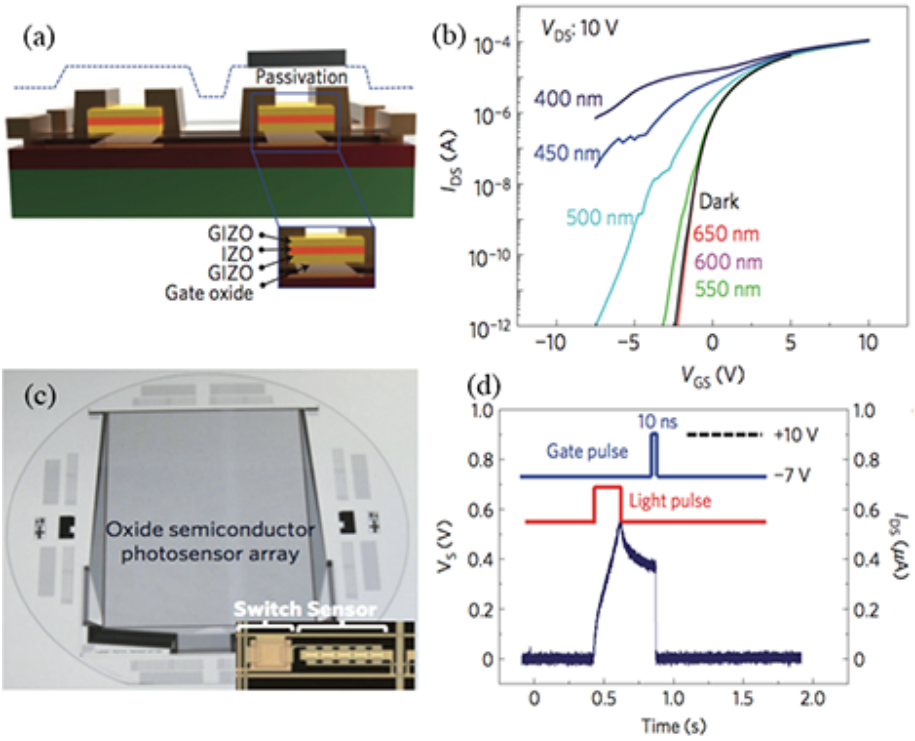

Figure 1.16 Semiconductor photosensing array by IGZO/IZO phototransistors [67].

5.3 Phototransistor with QDs' hybrid active layer

To avoid the disadvantage of bulk materials' weak light absorbance, QDs are selected as the alternative candidate for the photosensing component, sspecially after the emerging of the colloidal chemical synthesized QDs that can be easily transferred and embedded in the large-scale microelectronics. One solution is set the QDs into the active layer to increase the photoconductivity under illumination, and the first easy method is to use the QDs as the active layer directly with the TFT's process. Gerasimos Konstantatos and Lan Howard report this structure in Nature at 2006 [68]. Benefits from the high light absorbance efficiency and the long recombination lifetime, the responsivity of this device is super high, reaching 1000 A/W. But, limited by the poor mobility (<0.01 $cm^2V^{-1}S^{-1}$) and the on/off ratio of the QDs active layer, the electrical property of this device is really poor which even can not be qualified as a transistor.

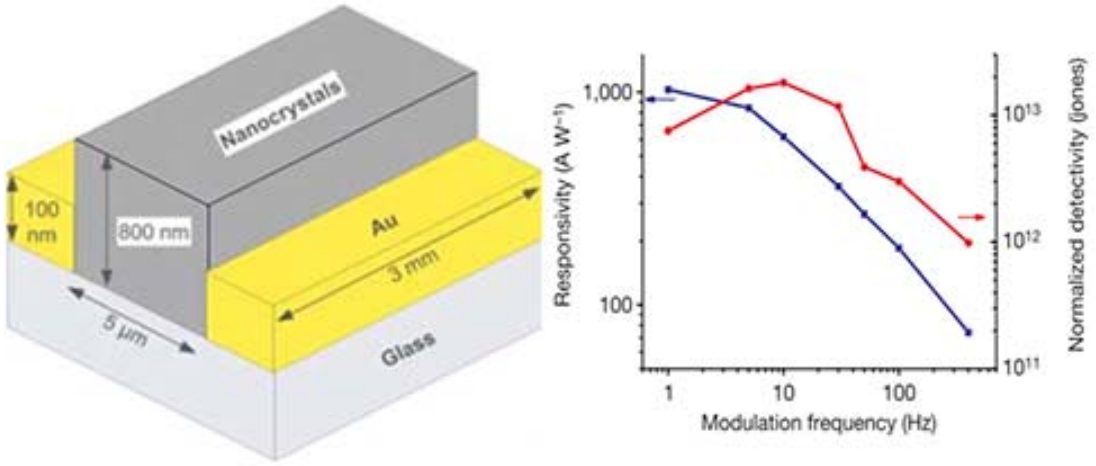

Figure 1.17 The FET device with only-QDs in the channel and the responsivity and detectivity of this device [68].

Therefore, researchers began to mixed QDs with other components which have better electrical properties (for example, IGZO, graphene, Carbon nanotube and so on). To combine the excellent light absorption and the electrical performance of the device [69-71]. S. W. Shin and K. H. Lee blended the QDs/IGZO hybrid as the active layer to achieve one of the device, reported on 2015. Through this technology, the device exhibited an excellent transfer characteristics IV curve and showed highly photo-sensitivity as can be seen in the figure 1.18. Meanwhile the response time of the Oxide-based material's PPC effect is constrained by the QDs to obtain a quick answer toward the pulse incident light. But this method still has some problems such as the bad uniform QDs film and bad quality of the hybrid active layer.

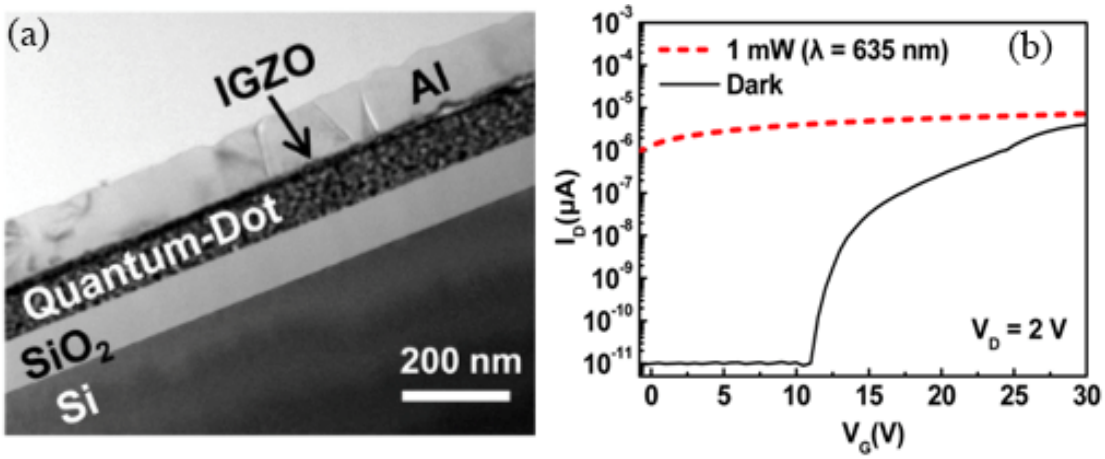

Figure 1.18 The IGZO/QDs hybrid materials in the TFT's channel [69].

Another famous way is to use new graphene material as the active layer for its super high mobility and the good contact between graphene and QDs [72-74]. Figure 1.19 depicts the schematic of this device and its responsivity. The responsivity can reach up to 10^5 A/W due to the high 2000 $cm^2V^{-1}S^{-1}$ mobility. But, graphene is not a stable material now to be used as active layer of transistors. There are so many works to do for opening the bandgap and limiting the off-state current.

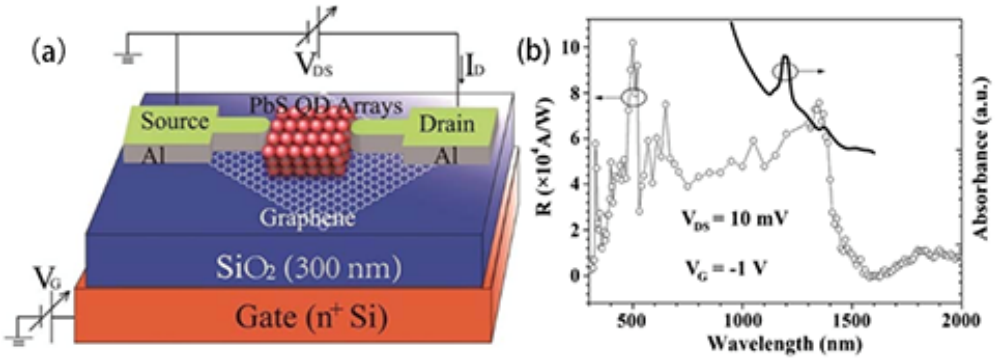

Figure 1.19 Phototransistor with graphene/QDs channel and its responsivity [73].

In summary, although it still exists so many problems inside, this QDs hybrid active layer is a possible solution to integrate QDs into microelectronics. Some researchers and engineers used this device for practical remote sensors and obtained a well performance [75]. Thus, I believe it is still one of the hottest research field.

5.4 Phototransistor with QDs' hybrid insulator

Compared with doping QDs into the channel, hybrid insulator embedded with QDs has a better uniformity and thick photo-sensing layers for the phototransistor. However, the problem is the high potential to block the electron's injection from insulator which cause a low responsivity [76, 77]. So the importance of this structure is to shorten the potential barrier as possible and increase the density of QDs which will also curtail the distance between neighbor QDs.

At 2008, S. S. Tseng and P. W. Li embedded Germanium quantum dots into TEOS gate insulator of Poly-silicon phototransitors [78]. This Poly-Si TFT showed a

significant responsivity and drive current under 400~450 nm light irradiation. J. M. Shieh and W. C. Yu fabricated phototransistor with silicon QDs to generate photocurrent under 1310nm and 1550nm wavelengths [79]. At these wavelengths, this phototransistor showed ~3 A/W responsivity with amplifying function in the channel.

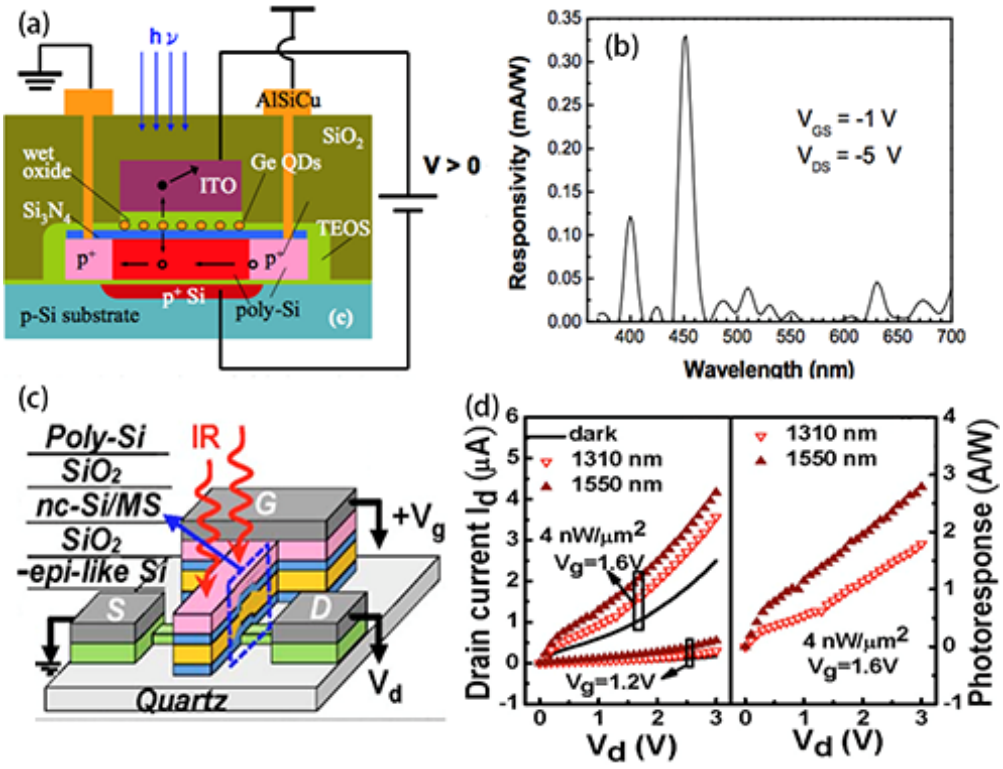

Figure 1.20 (a) Schematic diagram of germanium quantum dots embedded in the TEOS insulator for the Poly-silicon phototransitors. (b) Responsivity of this phototransistor [78]. (c) The silicon quantum dots embedded in the epi-like Si phototransistor's structure's image. (d) The output characteristics of the phototransistor and the responsivity under IR light [79].

M. H. Kuo and W. T. Lai demonstrated a CMOS approach for integrating Ge QDs in the composite insulator to inject the electrons into the channel [80]. Through this fabrication approach, the distance between QDs is curtailed to transfer the carriers feasibly. The photocurrent ratio and the responsivity were 4.1×10^6 and 1.7 A/W, respectively. A superior external quantum efficiency of 240% and a very fast temporal response time of 1.4 ns have been obtained. These research results manifest the great promise for these Si-based phototransistor in the optical interconnects and

telecommunications. However, the disadvantages of these QDs' synthesis methods are the complicated process, the rigid fabrication conditions, the non-uniformity and the thin as-prepared QDs layer.

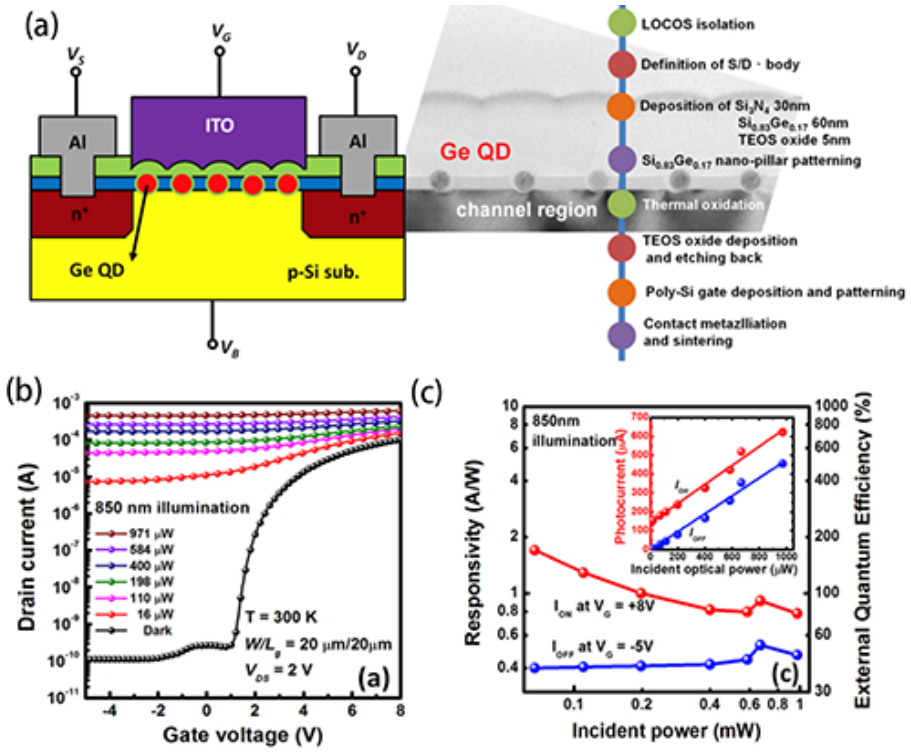

Figure 1.20 Ge QDs embedded in the silicon nitride insulator of silicon phototransistor. (b) Transfer characteristics of the phototransistor under 850 nm with different incident power. (c) Responsivity, EQE and photocurrent versus different powers of the phototransistor [80].

In our work, thanks to the new chemical producted colloid QDs, highly QDs concentrated insulator was developed as gate insulator of phototransistors at low-temperature. The detailed fabrication process and the performance of this device are introduced in the following chapters.

6. Conclusion

Phototransistor combined with the IR absorption of PbS QDs can be very useful in optoelectronics, telecommunication, IR imaging and remote control, etc. To pursue a

high-efficiency and wide detecting, technology progresses have been developed starting from traditional HdCdTe bulk material. Quantum well multilayers and strained superlattices materials to other solution processed QDs materials have been used.

Especially, phototransistors with QDs materials embedded into the TFT's channel and the gate insulator can be the final solution for highly photosensitive devices in determined wavelength range.

7. Reference

[1] M. B. Gray, D. A. Shaddock, C. C. Harb, and H. A. Bachor, "Photodetector Designs for Low-Noise, Broadband, and High-Power Applications", Review of Scientific Instruments, Vol. 69, No. 11, (1998), pp.3755-62.

[2] F. Yan, X. Xin, S. Aslam, Y. Zhao, D. Franz, J. H. Zhao and M. Weiner, "4H-SiC UV Photo Detectors with Large Area and Very High Specific Detectivity", IEEE Journal of Qauntum Electronics, Vol. 40, No. 9, (2004), pp. 1315-20.

[3] S. Ghanbarzadeh, S. Abbaszadeh, and K. S. Karim, 'Low Dark Current Amorphous Silicon Metal-Semiconductor-Metal Photodetector for Digital Imaging Applications', IEEE Electron Device Letters, Vol. 35, No. 2, (2014), pp. 235-37.

[4] D. Feng, S. Liao, P. Dong, N. Feng, H. Liang, D. Zheng, C. –C. Kung, J. Fong, R. Shafiiha, J. Cunningham, A. V. Krishnamoorthy, and M. Asghari, "High-Speed Ge Photodetector Monolithically Integrated with Large Cross-Section Silicon-on-Insulator Waveguide", Applied Physics Letters, Vol. 95, No. 26, (2009), p. 261105.

[5] Z. Zheng, L. Gan, H. Li, Y. Ma, Y. Bando, D. Golberg, and T. Zhai, "A Fully Transparent and Flexible Ultraviolet-Visible Photodetector Based on Controlled Electrospun ZnO-CdO Heterojunction Nanofiber Arrays", Advanced Functional Materials, Vol. 25, No. 37, (2015), pp. 5885-94.

[6] G. Maculan, A. D. Sheikh, A. L. Abdelhady, M. I. Saidaminov, M. A. Haque, B. Murali, E. Alarousu, O. F. Mohammed, T. Wu, and O. M. Bakr, "Ch3nh3pbcl3 Single Crystals: Inverse Temperature Crystallization and Visible-Blind Uv-Photodetector", J Phys Chem Lett, Vol. 6, No. 19, (2015), pp. 3781-6.

[7] S. Zhu, Y. Gao, B. Hu, J. Li, J. Su, Z. Fan, and J. Zhou, "Transferable Self-Welding Silver Nanowire Network as High Performance Transparent Flexible Electrode", Nanotechnology, Vol. 24, No. 33, (2013), p. 335202.

[8] Y. Hu, H. O. Churchill, D. J. Reilly, J. Xiang, C. M. Lieber, and C. M. Marcus, "A Ge/Si Heterostructure Nanowire-Based Double Quantum Dot with Integrated Charge Sensor", Nature Nanotechnology, Vol. 2, No. 10, (2007), pp. 622-5.

[9] D. Pacifici, H. J. Lezec, and H. A. Atwater, "All-Optical Modulation by Plasmonic Excitation of Cdse Quantum Dots", Nature Photonics, Vol. 1, No. 7, (2007), pp. 402-06.

[10] M. E. Ikpi, P. Atkinson, S. P. Bremner, and D. A. Ritchie, "Fabrication of a Self-Aligned Cross-Wire Quantum-Dot Chain Light Emitting Diode by Molecular Beam Epitaxial Regrowth", Nanotechnology, Vol. 23, No. 22, (2012), p. 225304.

[11] L. Sang, J. Hu, R. Zou, Y. Koide, and M. Liao, "Arbitrary Multicolor Photodetection by Hetero-Integrated Semiconductor Nanostructures", Scientific Report, Vol. 3, (2013), p. 2368.

[12] T. Spuesens D. V. Thourhout, S. K. Selvaraja, L. Liu, G. Roelkens, R. Kumar, G. Morthier, P. Rojo-Romeo, F. Mandorlo, P. Regreny, O. Raz, C. Kopp, and L. Grenouillet, "Nanophotonic Devices for Optical Interconnect", IEEE Journal of Selected Topics in Quantum Electronics, Vol. 16, No.5, pp. 1363-75.

[13] A. X. Wang, and X. Kong, "Review of Recent Progress of Plasmonic Materials and Nano-Structures for Surface-Enhanced Raman Scattering", Materials (Basel), Vol. 8, No. 6, (2015), pp. 3024-52.

[14] M. S. Islam and L. VJ, "Nanoscale Materials and Devices for Future Communication Networks", IEEE Communications Magazine, Vol. 48, No. 6, (2010), pp. 112-20.

[15] D. Pan, H. Wei, and H. –X. Xu, "Metallic Nanowires for Subwavelength Waveguiding and Nanophotonic Devices", Chinese Physics B, Vol. 22, No. 9, (2013), p. 097305.

[16] A. H. Aly, M. Ismaeel, and E. Abdel-Rahman, "Comparative Study of the One Dimensional Dielectric and Metallic Photonic Crystals", Optics and Photonics Journal, Vol. 02, No. 02, (2012), pp. 105-12.

[17] A. R. Tao, S. Habas, and P. Yang, "Shape Control of Colloidal Metal Nanocrystals", Small, Vol. 4, No. 3, (2008), pp. 310-25.

[18] G. H. Gweon, T. Sasagawa, S. Y. Zhou, J. Graf, H. Takagi, D. H. Lee, and A. Lanzara, "An Unusual Isotope Effect in a High-Transition-Temperature Superconductor", Nature, Vol. 430, No. 6996 (2004), pp. 187-90.

[19] A. K. Iyer and G. V. Eleftheriades, "Characterization of a Multilayered Negative-Refractive-Index Transmission-Line (NRI-Tl) Metamaterial", Microwave Symposium Digest, 2006. IEEE MTT-S International (2006), pp. 428-31.

[20] A. Armghan, X. Hu, S. Yuan, and J. Xia, "Negative Refractive Index Metamaterial Structure Using Srr by Incidenting the Light Horizontally", Journal of Electromagnetic Analysis and Applications, Vol. 7, No. 11, (2015), pp. 276-82.

[21] W. Lv, J. Zhong, Y. Peng, Y. Li, X. Luo, L. Sun, F. Zhao, J. Zhang, H. Xia, Y. Tang, S. Xu, and Y. Wang, "Organic near-Infrared Upconversion Devices: Design Principles and Operation Mechanisms", Organic Electronics, Vol. 31, (2016), pp. 258-65.

[22] H. S. Pattanaik, M. Reichert, D. J. Hagan, and E. W. V. Stryland, 'Three-Dimensional Ir Imaging with Uncooled Gan Photodiodes Using Nondegenerate Two-Photon Absorption', Opt Express, Vol. 24, No. 2, (2016), pp. 1196-205.

[23] S. -Y. Wang H. -S. Ling, W.-C. Hsu, and C. -P. Lee, "Voltage-Tunable Dual-Band Quantum Dot Infrared Photodetectors for Temperature Sensing", Opt Express, Vol. 20, No. 10, (2008), pp. 10484-89.

[24] F. H. Koppens, T. Mueller, P. Avouris, A. C. Ferrari, M. S. Vitiello, and M. Polini, "Photodetectors Based on Graphene, Other Two-Dimensional Materials and Hybrid Systems", Nature Nanotechnology, Vol. 9, No. 10, (2014), pp. 780-93.

[25] A. Pospischil, M. Humer, M. M. Furchi, D. Bachmann, R. Guider, T. Fromherz, and T. Mueller, "CMOS-Compatible Graphene Photodetector Covering All Optical Communication Bands", Nature Photonics, Vol. 7, No. 11, (2013), pp. 892-96.

[26] N. Das, F. F. Masouleh, and H. R. Mashayekhi, "A Comprehensive Analysis of Plasmonics-Based GaAs Msm-Photodetector for High Bandwidth-Product Responsivity", Advances in OptoElectronics, Vol. 2013 (2013), pp. 1-10.

[27] W. K. Bae, J. Kwak, J. Lim, D. Lee, M. K. Nam, K. Char, C. Lee, and S. Lee, "Multicolored Light-Emitting Diodes Based on All-Quantum-Dot Multilayer Films Using Layer-by-Layer Assembly Method", Nano Letters, Vol. 10, No. 7, (2010), pp. 2368-73.

[28] J. Kwak, W. K. Bae, D. Lee, I. Park, J. Lim, M. Park, H. Cho, H. Woo, D. Y. Yoon, K. Char, S. Lee, and C. Lee, "Bright and Efficient Full-Color Colloidal Quantum Dot Light-Emitting Diodes Using an Inverted Device Structure", Nano Letters, Vol. 12, No. 5, (2012), pp. 2362-6.

[29] K. Munechika, Y. Chen, A. F. Tillack, A. P. Kulkarni, I. Jen-La Plante, A. M. Munro, and D. S. Ginger, "Quantum Dot/Plasmonic Nanoparticle Metachromophores

with Quantum Yields That Vary with Excitation Wavelength", Nano Letter, Vol. 11, No. 7, (2011), pp. 2725-30.

[30] F. Maier-Flaig, C. Kubel, J. Rinck, T. Bocksrocker, T. Scherer, R. Prang, A. K. Powell, G. A. Ozin, and U. Lemmer, "Looking inside a Working Siled", Nano Letters, Vol. 13, No. 8, (2013), pp. 3539-45.

[31] L. Zhang D. Yang, H. Wang, Y. Wang, Z. Li, T. Song, C. Fu, S. Yang, and B. Zou, "Pentacene-Based Photodetector in Visible Region with Vertical Field-Effect Transistor Configuration", IEEE Photonics Technology Letters, Vol. 27, No. 3, (2015), pp. 233-36.

[32] D. Yang, L. Zhang, S. Y. Yang, and B. S. Zou, "Influence of the Dielectric PMMA Layer on the Detectivity of Pentacene-Based Photodetector with Field-Effect Transistor Configuration in Visible Region", IEEE Photonics Journal, Vol. 5, No. 6, (2013), pp. 6801709-09.

[33] A.Nourbakhsh, A. V. Klekachev, I. Asselberghs, A. L. Stesmans, M. M. Heyns, and S. D. Gendl, "Graphene Transistors and Photodetectors", Electrochemical Society Interface, Vol. 22, No. 1, (2013), pp. 63-68.

[34] T. George, O. Koybasi, M. S. Islam, I. Childres, I. Jovanovic, A. Dutta, and Y. P. Chen, "Graphene Field Effect Transistor as a Radiation and Photodetector", Proceeding of SPIE, Vol. 8373, (2012), p. 83730H.

[35] J. Frigerio, G. Isella, S. Bietti, "Multispectral imaging sensors integrated on silicon", july, SPIE Newsroom, 2013.

[36] P. NORTON, "HgCdTe Infrared Detectors", Opto-Electronic Review, Vol.10, No. 3 (2002), pp. 159-74.

[37] W. Lei, R. J. Gu, J. Antoszewski, J. Dell, G. Neusser, M. Sieger, B. Mizaikoff, and L. Faraone, “MBE Growth of Mid-Wave Infrared HgCdTe Layers on GaSb Alternative Substrates”, Journal of Electronic Materials, Vol. 44, No.9, (2015), pp. 3180-87.

[38] R. S. Saxena, N. K. Saini, R. K. Bhan, and R. K. Sharma, “A New Circuit Model of HgCdTe Photodiode for Spice Simulation of Integrated IRFPA”, Infrared Physics & Technology, Vol. 67, (2014), pp. 58-62.

[39] H. C. Liu, A. G. Steele, M. Buchanan, and Z. R. Wasilewski, “Dark Current in Quantum Well Infrared Photodetectors”, Journal of Applied Physics, Vol. 73, No. 4, (1993), p. 2029.

[40] M. Oehme, D. Widmann, K. Kostecki, P. Zaumseil, B. Schwartz, M. Gollhofer, R. Koerner, S. Bechler, M. Kittler, E. Kasper, and J. Schulze, “GeSn/Ge Multi-quantum Well Photodetectors on Si Substrates”, Optical Letters, Vol. 39, No. 16, (2014), pp. 4711-4.

[41] Y. Arslan, T. Colakoglu, and C. Besikci, “Diffraction-Grating-Coupled High Quantum Efficiency Inp/Ingaas Quantum Well Infrared Photodetector Focal Plane Array”, IEEE Journal of Quantum Electronics, Vol. 49, No.2, (2013), pp. 186-95.

[42] K. P. Streubel, A. Laubsch, H. Jeon, M. Sabathil, G. Bruederl, J. Wagner, M. Strassburg, E. Baur, H. Braun, U. T. Schwarz, A. Lell, S. Lutgen, N. Linder, R. Oberschmid, and B. Hahn, “Measurement of the Internal Quantum Efficiency of Ingan Quantum Wells”, Vol. 6486 (2007), p. 64860J.

[43] Y. Gu, Y. G. Zhang, Y. J. Ma, L. Zhou, X. Y. Chen, S. P. Xi, and B. Du, “Inp-Based Type-I Quantum Well Lasers up to 2.9 Mm at 230 K in Pulsed Mode on a Metamorphic Buffer”, Applied Physics Letters, Vol. 106, No.12, (2015), p. 121102.

[44] M. Strojnik, M. Nurul Abedin, T. F. Refaat, J. M. Zawodny, S. P. Sandford, U. N. Singh, S. V. Bandara, S. D. Gunapala, I. Bhat, and N. P. Barnes, “Multicolor Focal Plane Array Detector Technology: A Review”, Vol. 5152 (2003), pp. 279-288.

[45] H. Temkin, T. P. Pearsall, J. C. Bean, R. A. Logan, and S. Luryi, “Gexsi1−X Strained-Layer Superlattice Waveguide Photodetectors Operating near 1.3 Mm”, Applied Physics Letters, Vol. 48, No. 15, (1986), p. 963.

[46] J. B. Rodriguez, E. Plis, G. Bishop, Y. D. Sharma, H. Kim, L. R. Dawson, and S. Krishna, “Nbn Structure Based on Inas ⁄ Gasb Type-Ii Strained Layer Superlattices”, Applied Physics Letters, Vol. 91, No. 4, (2007), p. 043514.

[47] H. S. Kim, E. Plis, N. Gautam, S. Myers, Y. Sharma, L. R. Dawson, and S. Krishna, “Reduction of Surface Leakage Current in Inas/Gasb Strained Layer Long Wavelength Superlattice Detectors Using Su-8 Passivation”, Applied Physics Letters, Vol. 97, No. 14, (2010), p. 143512.

[48] G. J. Brown, G. J. Brown, F. Szmulowicz, and M. Razeghi, “InAs/InGaSb Superlattices for Very Long Wavelength Infrared Detection”, Proceedings of SPIE, Vol. 4288 (2001), pp. 200-208.

[49] M. A. Naser, M. J. Deen, and D. A. Thompson, “Theoretical Modeling of Dark Current in Quantum Dot Infrared Photodetectors Using Nonequilibrium Green’s Functions”, Journal of Applied Physics, Vol. 104, No. 1, (2008), p. 014511.

[50] A. Vardi, N. Akopian, G. Bahir, L. Doyennette, M. Tchernycheva, L. Nevou, F. H. Julien, F. Guillot, and E. Monroy, “Room Temperature Demonstration of GaN ⁄ AlN Quantum Dot Intraband Infrared Photodetector at Fiber-Optics Communication Wavelength”, Applied Physics Letters, Vol. 88, No. 14, (2006), p. 143101.

[51] W. Zhang, H. Lim, M. Taguchi, S. Tsao, B. Movaghar, and M. Razeghi, “High-Detectivity InAs Quantum-Dot Infrared Photodetectors Grown on InP by Metal–Organic Chemical–Vapor Deposition”, Applied Physics Letters, Vol. 86, No. 19, (2005), p. 191103.

[52] C. O. Kim, S. W. Hwang, S. Kim, D. H. Shin, S. S. Kang, J. M. Kim, C. W. Jang, J. H. Kim, K. W. Lee, S. H. Choi, and E. Hwang, “High-Performance Graphene-Quantum-Dot Photodetectors”, Scientific Report, Vol. 4 (2014), p. 5603.

[53] S. L. Diedenhofen, D. Kufer, T. Lasanta, and G. Konstantatos, 'Integrated Colloidal Quantum Dot Photodetectors with Color-Tunable Plasmonic Nanofocusing Lenses', Light: Science & Applications, Vol. 4, No. 1, (2015), p. e234.

[54] P. Bhattacharya, Semiconductor Optoelectronic Devies, Prentice Hall Englewood Cliffs, 1994.

[55] M. Fukuda, Optical Semiconductor Device, John Wiley and Sons Inc, 1999.

[56] A. Van der Ziel, Fluctuation phenomena in Semiconductors, Butterworths scientific publication, 1959.

[57] S. L. Chuang, Physics of Optoelectronic Devices, John Wiley and Sons Inc., 1995.

[58] T. E. Jenkins, Optical Sensing Techniques and Signal Processing, Prentice Hall International Englewood Cliffs, 1987.

[59] S. Kasap, J. B. Frey, G. Belev, O. Tousignant, H. Mani, J. Greenspan, L. Laperriere, O. Bubon, A. Reznik, G. DeCrescenzo, K. S. Karim, and J. A. Rowlands, “Amorphous and Polycrystalline Photoconductors for Direct Conversion Flat Panel X-Ray Image Sensors”, Sensors, Vol. 11, No. 5, (2011), pp. 5112-57.

[60] L. H. Zeng, M. Z. Wang, H. Hu, B. Nie, Y. Q. Yu, C. Y. Wu, L. Wang, J. G. Hu, C. Xie, F. X. Liang, and L. B. Luo, “Monolayer Graphene/Germanium Schottky Junction as High-Performance Self-Driven Infrared Light Photodetector”, ACS Applied Material & Interfaces, Vol. 5, No. 19, (2013), pp. 9362-6.

[61] M. Nikoufard, X.J.M. Leijtens, Y.C. Zhu, T.J.J. Kwaspen, E.A.J.M. Bente, F.H. Groen, and M.K. Smit, “Modelling and characterization of InP-based high-speed pin-photodiode”, in Proceedings Symposium IEEE/LEOS Benelux Chapter, 2003, Enschede.

[62] Y. Kang, M. Zadka S. Litski, G. Sarid, M. Morse, M. J. Paniccia, Y. -H. Kuo, J. Bowers, A. Beling, H. –D. Liu, D. C. McIntosh, J. Campbell and A. Pauchard, “Epitaxially-Grown Ge/Si Avalanche Photodiodes for 1.3μm Light Detection”, Optics Express, Vol. 16, No. 13, (2008), pp. 9365-71.

[63] Y. Lee, I. Omkaram, J. Park, H. -S. Kim, K. Kyung, W. Park, and S. Kim, “A α-Si:H Thin-Film Phototransistor for a Near-Infrared Touch Sensor”, IEEE Electron Device Letters, Vol. 36, No.1, (2015), pp. 41-43.

[64] J. Y. Oh, and M. S. Islam, “Nanobridge Gate-All-around Phototransistors for Electro-Optical or Gate Circuit and Frequency Doubler Applications”, Applied Physics Letters, Vol. 104, No. 2, (2014), p. 022110.

[65] C. Zhang, Z. H. Zhang, X. Yang, T. Zhou, C. B. Han, and Z. L. Wang, “Tribotronic Phototransistor for Enhanced Photodetection and Hybrid Energy Harvesting”, Advanced Functional Materials, 26 (2016), pp. 2554-60.

[66] S. E. Ahn, I. Song, S. Jeon, Y. W. Jeon, Y. Kim, C. Kim, B. Ryu, J. H. Lee, A. Nathan, S. Lee, G. T. Kim, and U. I. Chung, “Metal Oxide Thin Film Phototransistor for Remote Touch Interactive Displays”, Advanced Material, Vol. 24, No. 19, (2012), pp.2631-6.

[67] S. Jeon, S. E. Ahn, I. Song, C. J. Kim, U. I. Chung, E. Lee, I. Yoo, A. Nathan, S. Lee, J. Robertson, and K. Kim, 'Gated Three-Terminal Device Architecture to Eliminate Persistent Photoconductivity in Oxide Semiconductor Photosensor Arrays', Nat Mater, Vol. 11, No. 4, (2012), pp.301-5.

[68] G. Konstantatos, I. Howard, A. Fischer, S. Hoogland, J. Clifford, E. Klem, L. Levina, and E. H. Sargent, “Ultrasensitive Solution-Cast Quantum Dot Photodetectors”, Nature, Vol. 442, No. 7099, (2006), pp.180-3.

[69] S. W. Shin, K. H. Lee, J. S. Park, and S. J. Kang, “Highly Transparent, Visible-Light Photodetector Based on Oxide Semiconductors and Quantum Dots”, ACS Appl Mater Interfaces, Vol. 7, No.35, (2015), pp.19666-71.

[70] S. M. Lee, S. J. Park, K. H. Lee, J. –S. Park, S. Park, Y. Yi, and S. J. Kang, “Enhanced Photocurrent of Ge-Doped InGaO Thin Film Transistors with Quantum Dots”, Applied Physics Letters, Vol. 106, No.3, (2015), pp.031112.

[71] Z. Sun, Z. Liu, J. Li, G. A. Tai, S. P. Lau, and F. Yan, "Infrared Photodetectors Based on CVD-Grown Graphene and PbS Quantum Dots with Ultrahigh Responsivity", Advanced Materials, Vol. 24, No.43, (2012), pp.5878-83.

[72] C. Biswas, H. Jeong, M. S. Jeong, W. J. Yu, D. P. and Y. H. Lee, "Quantum Dot-Carbon Nanotube Hybrid Phototransistor with an Enhanced Optical Stark Effect", Advanced Functional Materials, Vol.23, No.29, (2013), pp.3653-60.

[73] R. Wang, Y. Zhang, H. Wang, X. Song, L. Jin, and J. Yao, "Wide Spectral Response Field Effect Phototransistor Based on Graphene-Quantum Dot Hybrid", IEEE Photonics Journal, Vol.7, No.2, (2015), pp.1-1.

[74] D. Zhang, L. Gan, Y. Cao, Q. Wang, L. Qi, and X. Guo, "Understanding Charge Transfer at PbS-Decorated Graphene Surfaces toward a Tunable Photosensor", Advanced Materials, Vol. 24, No.20, (2012), pp.2715-20.

[75] D. K. Hwang, Y. Tack. Lee, H. S. Lee, Y. J. Lee, S. H. Shokouh, J. Kyhm, J. Lee, H. H. Kim, T. –H. Yoo, S. H. Nam, D. I. Son, B. –K. Ju, M. –C. Park, J. D. Song, W. K. Choi, and S. Im, "Ultrasensitive PbS Quantum-Dot-Sensitized InGaZnO Hybrid Photoinverter for near-Infrared Detection and Imaging with High Photogain", NPG Asia material, Vol.8, (2016), p. e278.

[76] P. Zingway, C. S. Liang, L. S. Lai, Y. T. Tseng, Y. M. Hsu, P. S. Chen, S. C. Lu, M. J. Tsai, and C. W. Liu, "A High-Performance SiGe-Si Multiple-Quantum-Well Heterojunction Phototransistor", IEEE Electron Device Letters, Vol. 24, No. 10, (2003), pp.643-45.

[77] A. V. Dvurechenskiœ A. I. Yakimov, V. V. Kirienko, and A. I. Nikiforov, "Ge/Si Photodiodes and Phototransistors with Embedded Arrays of Germanium Quantum Dots for Fiber-Optic Communication Lines", Physics of the Solid State, Vol. 47, No. 1, (2005), pp.34–37.

[78] I. H. Chen S. S. Tseng, and P. W. Li, "Photoresponses in Poly-Si Phototransistors Incorporating Germanium Quantum Dots in the Gate Dielectrics", Nanotechnology, IEEE Conference on (2008), pp.48-50.

[79] J. –M. Shieh, W. –C. Yu, J. Y. Huang, C. –K. Wang, B. –T. Dai, H. –Y. Jhan, C. –W. Hsu, H. –C. Kuo, F. –L. Yang, and C. –L. Pan, "Near-Infrared Silicon Quantum Dots Metal-Oxide-Semiconductor Field-Effect Transistor Photodetector", Applied Physics Letters, Vol. 94, No. 24, (2009), p.241108.

[80] M. H. Kuo, W. T. Lai, T. M. Hsu, Y. C. Chen, C. W. Chang, W. H. Chang, and P. W. Li, "Designer Germanium Quantum Dot Phototransistor for near Infrared Optical Detection and Amplification", Nanotechnology, Vol. 26, No. 5, (2015), p. 055203.

Chapter 2 Fabrication technology and electrical characterization of Poly-silicon Thin Film Transistor

1. Introduction

In last 30 years, LCD and OLED (flat plane displays, FPD) devices have occupied the display market. The TFT technology as the addressing and driving core has been explored and promoted by all the researchers and manufactures [1-3]. From the α-Si TFT to Low-temperature-Poly-silicon (LTPS) and oxide TFT technology, many new technologies emerged during these decades [4-8].

In our IETR group, LTPS TFT has been studied for a long time. The technology led to great performance for the mobility, on/off ratio and stability [9-11]. Moreover, this poly-silicon TFT have also been utilized in many fields as display, biosensor, MEMS and in optoelectronics [12-14]. In this thesis, this technology is used in the developed phototransistor process. Since the goal of this thesis is to find out a possible method to integrate QDs into TFT device for achieving a highly-sensitive performance, combining LTPS process and organic SU8 gate insulator fabrication technology can be the key technique.

In this chapter, the fabrication process of Poly-silicon TFT is described. The steps of the process and the tools used during these steps are introduced and summarized. After that, modification of the process by using SU8 as gate insulator in place of usual SiO_2 insulator will be described.

2. Fabrication Process of Thin Film Transistor

Figure 2.1 illustrates the top-gated TFT structure and the forming sequence for the fabrication through the cross-sectional schematic image. The fabrication of the TFT starts with the glass substrate. Undoped polysilicon is deposited on it as the active layer. Then, doped polysilicon is deposited and etched to form the drain and source regions. The doping type determines the TFT's type (N or P channel). Afterwards, the gate insulator is deposited. Finally, the drain/gate/source electrodes are sputtered on the top surface.

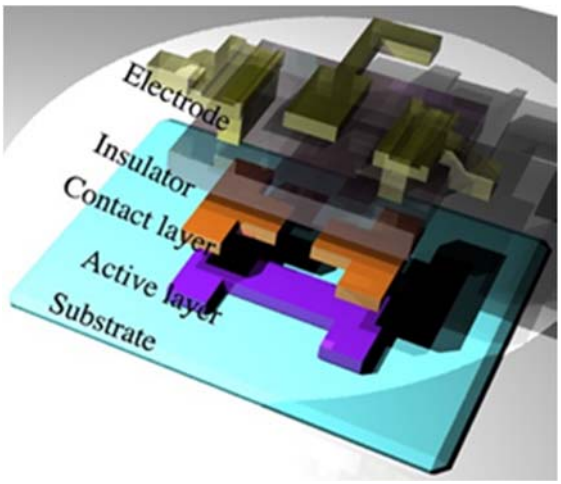

Figure 2.1 The cross-sectional schematic of the LTPS TFT we used to illustrate the structure and the depositing sequence for fabrication.

2.1 Undoped poly-silicon active layer deposition by LPCVD

In this work, Low Pressure Chemical Vapor Deposition (LPCVD) technique was used to get silicon films on the glass substrate. The glass substrate is cleaned by acetone and alcohol in turn for three times for sake of removing dirt and impurities on the substrate. Finally, the substrate is blew by Nitrogen to dry the substrate as depicted in figure 2.7 and baked at 100℃for around 3-5 minutes to guarantee the arid. After that, 150nm undoped film as active layer is deposited in the substrate by LPCVD deposition process.

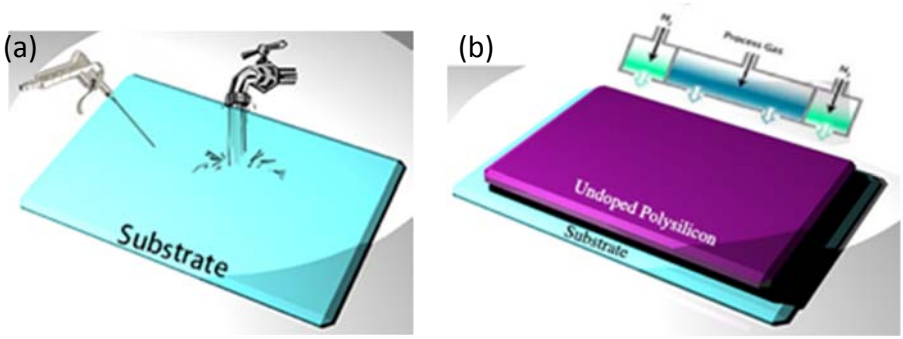

Figure 2.2 schematic for substrate preparation (a) and undoped Polysilicon deposition by LPCVD (b).

The deposition reactor is shown figure 2.3 [15]. Thermal decomposition of silane

by LPCVD leads to better uniformity, low oxygen content, non-fogging surface, high-volume products and is cost-effective. Thus LPCVD is the main stream method for depositing Poly-silicon. The reaction formula of Poly-silicon growth by LPCVD is:

$$SiH_4 \xrightarrow[550\sim660℃]{\approx 40\ \mathrm{Pa}} Si + 2H_2$$

The process parameters affecting deposition are temperature, silane flow and reaction pressure. In this thesis, the detailed deposition condition is presented in table 2.1.

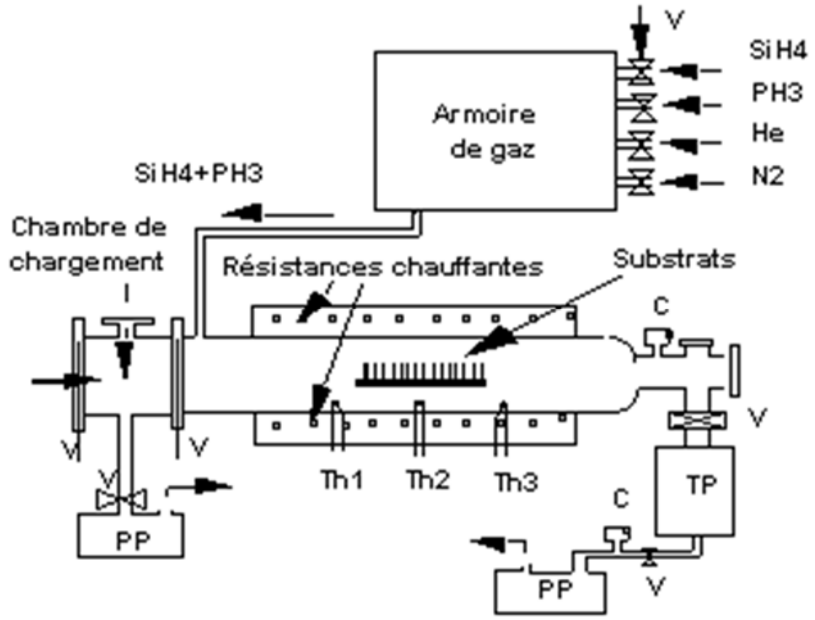

Figure 2.3 LPCVD reactor graphic schematic for the Poly-silicon deposition [15].

Table 2.1 The deposition conditions of silicon by LPCVD

Growth index	Substrate temp.	Reaction press.	Gas flow ratio	SiH_4 flow
parameters	600℃	0.9 mbar	SiH4:Ar=1:9	25 div

In these deposition conditions, silicon is amorphous.

To form polycrystalline silicon, the furnace temperature is increased to 600°C while the substrates are still inside. At this temperature, silicon films crystallize in a

time of 8 hours. Poly-silicon films are then obtained.

2.2 Doped poly-silicon deposition for drain/source region

After the undoped polysilicon active layer is deposited, the doped layer is essential for the formation of the source/drain region. Thus, 300nm doped polysilicon layer is deposited by similar LPCVD process as shown in figure 2.4; only doping gas is added during the deposition. For N-type TFT, we need N-type doped source and drain regions so that phosphine is added. For P-type TFT, diborane is added.

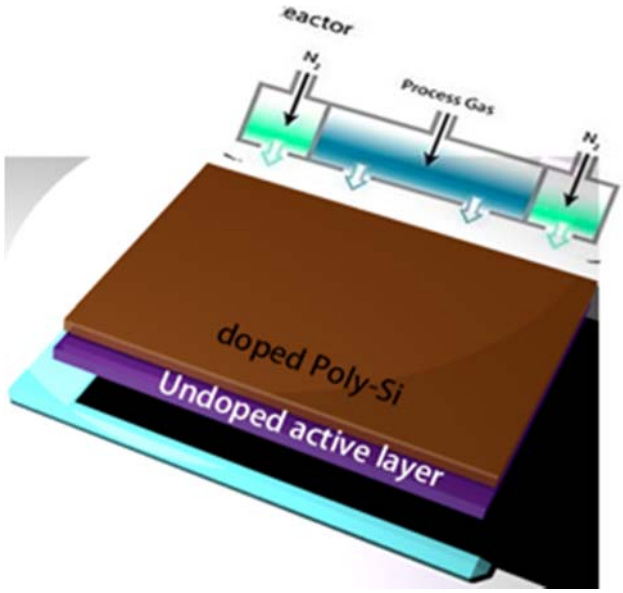

Figure 2.4 Schematic for doped poly-silicon layers by LPCVD

To better research the transfer mechanism in the phototransistors, both N-type and P-type TFTs are employed to explore the photocurrent generating phenomenon in these two types of TFTs. As can be seen in the LPCVD operating schematic in figure 2.3, the impurity gas of this reaction for N-type polysilicon is the PH_3, which can be used to combine with the SiH_4 hot decomposition. As for the p-type polysilicon deposition, the Borane gas can be utilized for the impurity.

2.3 Definition of TFT's channel and geometry

As for definition of TFT's channel, the doped poly-silicon thin film must be etched to expose completely the undoped poly-silicon for achieving an excellent on/off ratio and lower off-state current. In this thesis, the plasma RIE (Reactive ion etching) process

was carried out and SF_6 is employed to etch the N-doped poly-silicon. As shown in figure 2.5, the SF_6 gas is ionized under the 13.56MHz radio frequency source and accelerated to the etched silicon thin film. Under plasma state, the reaction between SF_6 gas and silicon film will be promoted.

Due to the highly anisotropic feature and vertical etching direction, the etching rate for the poly-silicon will be larger and controllable to stop when the full thickness of the doped layer is etched. Thus, the detailed process parameters are as following:

Table 2.2 The process parameters of the RIE process

Etched material	Reactive gas	Gas flow (sccm)	Pressure (mTorr)	Power (W)	Etching rate (nm/min)
Poly-Si	SF_6	10	10	40	≈160

Moreover, for screening the interference between different devices, the isolation of each TFT should be performed by the etching processes. The fabrication process of this mask 2 lithography and RIE process are similar to the above channel definition fabrication process.

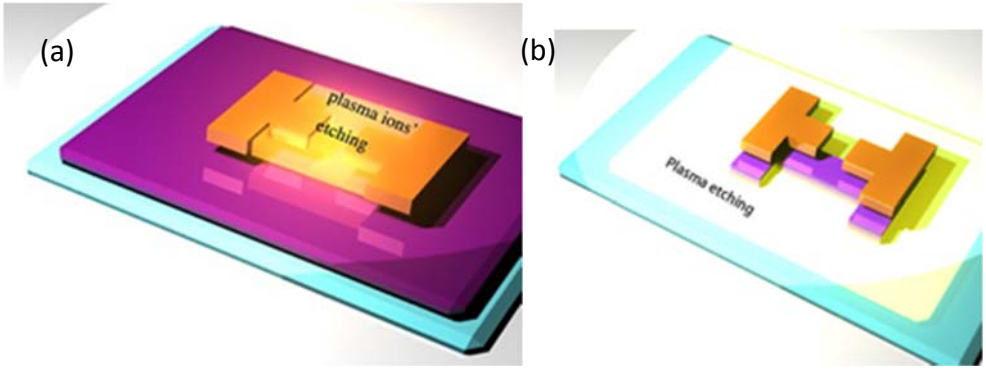

Figure 2.5 Schematic of the RIE plasma etching for the channel's definition (a) and device's isolation (b).

2.4 RCA cleaning of the as-prepared device

For removing the organic and metallic impurities on the surface of the previous

silicon, RCA cleaning is carried out by the three steps to improve the surface qualities in the TFT active layer area. The detailed contents of three steps, cleaning material and experimental times are as followed:

(1) The bath with (H_2O+NH_4OH+H_2O_2) is taken at 70℃ for 10 min: the raio of these three components is 200ml: 10ml: 40ml; after temperature of the NH4OH solution reach up to 70℃, the H_2O_2 should be added into this bath and kept reaction for 10 min.

(2) The bath with (H_2O+HCl +H_2O_2) is taken at 80℃ for another 10min: the ratio for these three components is 200ml: 40ml: 40ml; after temperature of HCl solution reach up to 80℃, the H_2O_2 should be added into this bath and also kept reaction for 10 min.

(3) The deoxydation process of HF 2％ diluted solution: the RCA cleaning process can be finished by adding samples into this HF 2% solution (400ml H_2O and 16ml HF) until realizing the hydrophobic characters of the silicon surface.

2.5 Gate insulator deposition

2.5.1 SiO_2 inorganic insulator deposition

For researching the properties of the polysilicon TFT, high quality SiO_2 inorganic insulator thin film was deposited on the as-prepared polysilicon substrate. Herein, the deposition technology we used here is the Atmospheric Pressure Chemical Vapor Deposition (APCVD) as shown in figure 2.6. And SiO_2 thin film was formed through thermal decomposition at 450℃ by mixed Silane and oxygen O_2 following the 2 reactions:

$SiH_4 \rightarrow Si+2\ H_2$

$Si + O_2 \rightarrow SiO_2$

The APCVD possesses many advantages, for example rapid film forming velocity, easy reaction and low temperature deposition condition [16]. For guaranteeing the quality of the film, the process parameters, such as temperature, pressure, gas components, and deposition rate, should be controlled rigidly. Here, the reactive mixed

gas (O_2, diluted Nitrogen N_2, and silane (SiH_4)) are vented into the chamber. The pressure during reaction is 10^5 Pa. The deposition rate is important, around 20 nm/min) and the dispersion on the thickness is lower than 5%. After formation, the deposition is followed by a thermal annealing at 600°C during 1 hour.

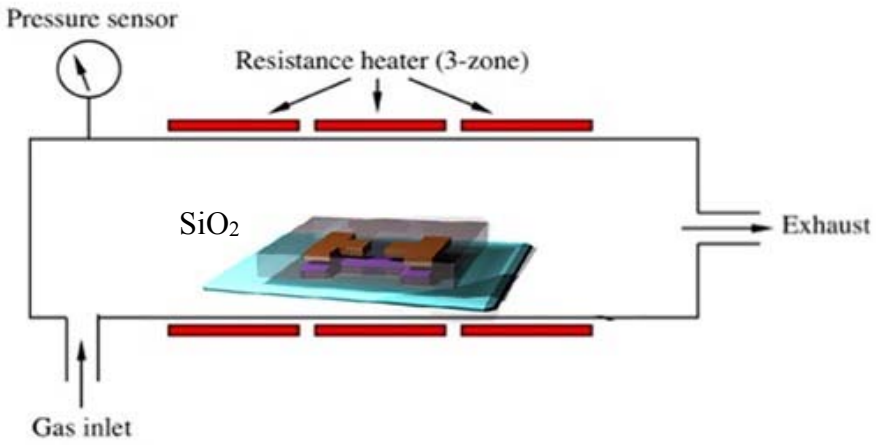

Figure 2.6 Schematic for depositing SiO_2 gate insulator by APCVD process

In our processes, the samples with patterned undoped and doped polysilicon layers were put into the APCVD chamber and be deposited by SiO2 thin film, as show in figure 2.6. Figure 2.7 show typical 1 MHz (HF) and in Quasi-Static (QS) capacitance-voltage characteristics of a MIS structure using APCVD SiO2 as insulator.

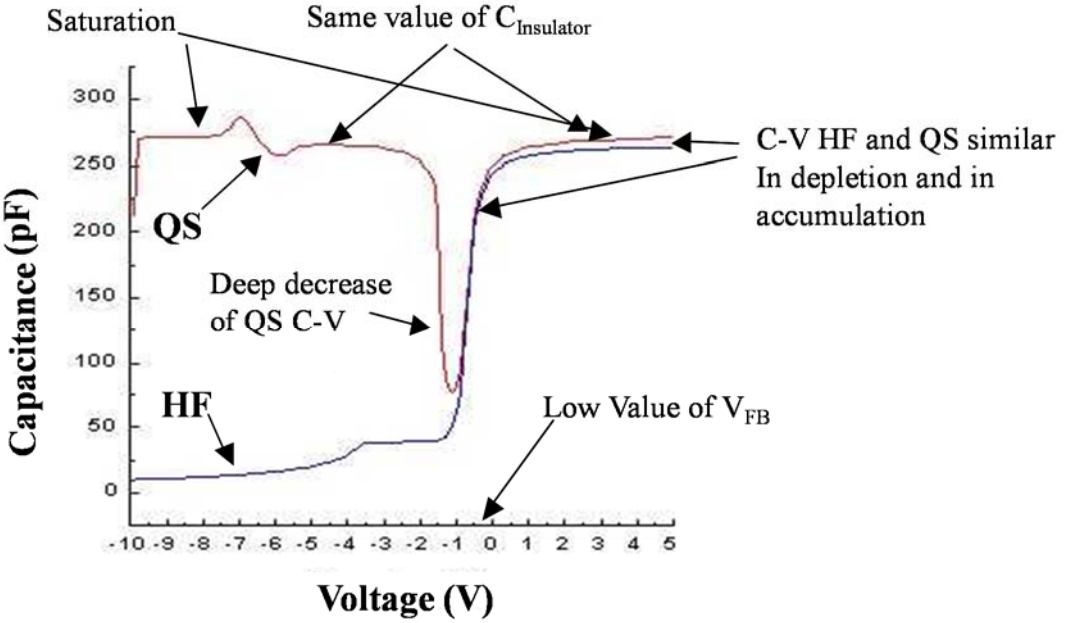

Figure 2.7: C(V) characteristic of a MIS structure using 59 nm thick SiO2 deposited by APCVD as insulator.

The curves present all the characteristics of a gate insulator quality:

(1) Saturated and same Value of the QS capacitance in inversion and accumulation regimes showing weak leakage current in the insulator

(2) Deep decrease of the QS capacitance in depletion regime showing weak content of defects at insulator-Semiconductor interface

(3) Low value of the Flat-Band Voltage VFB showing weak content of fixed charges inside the insulator

Quantitatively, the main parameters extracted from these curves are presented in Table 2.3.

Table 2.3 Characterisitcs of 59nm thick silicon dioxide extracted from the CV curves of figure 2.3.

Tickness of SiO_2	V_{FB} (V)	Density of charges at the interface Q_{SS}/q (cm^{-2})	Breakdown field (MV/cm)
59nm	-0.7	1.6×10^{11}	10.7

2.5.2 SU8 organic insulator deposition

For the phototransistors in this thesis with photo-sensing hybrid insulator, the liquid organic insulator can be utilized by blending with the QDs solid nanoparticle. The common-used organic insulator material, polyving akohol (PVA), polystyrene (PS), poly-p-vinylphenol (PVPh) and polymethylmethacrylate (PMMA), are alternative options for the TFT [17-20]. However, SU8 2000.5 organic photo-resist is used for the insulator due to a thin spin-coated film, cheap and feasible thin film deposition process. On account of providing the possibility to use the following QDs/SU8 insulator, the pristine SU8 insulator is used here for certificating the performance of SU8 insulator and the TFT with SU8 gate insulator.

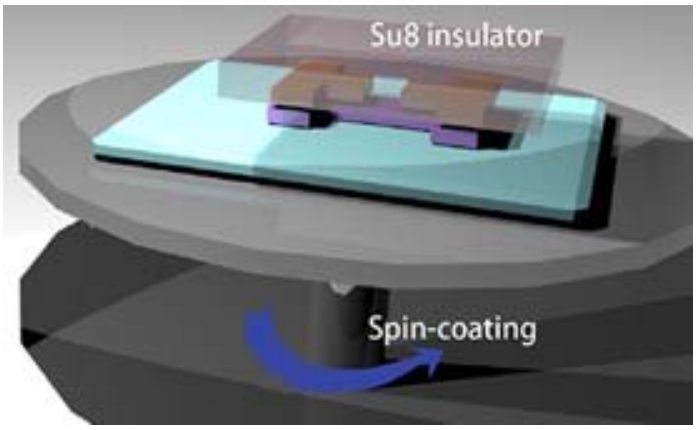

Figure 2.8 Schematic for SU8 insulator spin-coating

Herein, the process of deposition is the spin-coating process which has the following parameters:

Spin-coating speed: 2500 rpm

Accelerate rate: 3000 rpm/s

Spin-coating duration: 30 s

SU8 was using soft-bake process through 95℃ annealing to evaporate all the solvents in SU8 solution. SU8 is composed by small molecules. The as-fabricated sample was exposed under UV light and SU8 organic layer was cross-linked due to the oxidation in the organic layer. After the develop process of SU8 in the develop solution, the SU8 layer was after-baked in the heating stage for 60s. Finally, SU8 organic insulator was heated at the stage by increasing temperature from 95℃ to 115℃, and kept in the 115℃for 30 min to solidify the SU8 organic insulator. Through profile measurement, the formed SU8 insulator's thickness was observed as 350nm.

To detect the performance of the SU8 organic insulator, the electrical properties such as capacitance and leakage current are carried out to characterize the SU8 insulator. Figure 2.9 shows the C-V characteristic of Al/SU8/Si MIS structure device with 1 mm^2 at 1 MHz high frequency.

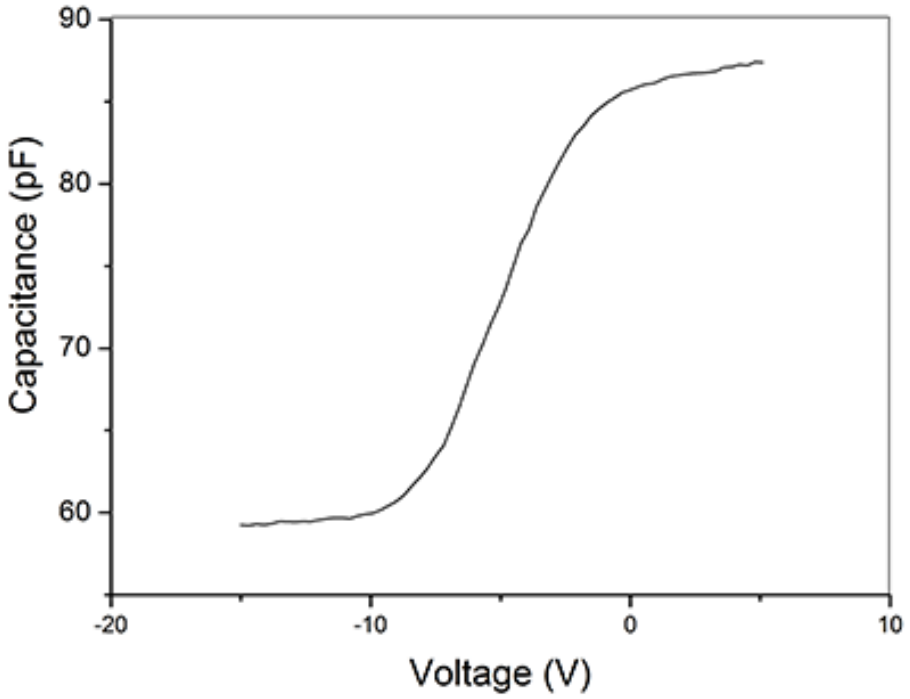

Figure 2.9 The C-V characteristic of the Al/SU8/Si MIS structure device at high frequency 1 MHz.

In this experiment, the interface aroused by SU8 organic insulator contact with Si substrate is the same with the practical interface between SU8 and the Poly-silicon active layer. Therefore, the capacitance behavior demonstrate that this SU8 has enough capacitance characters for the SU8 gated TFT.

For the leakage current, another MIM capacitor is fabricated on the ITO-coated glass substrate by depositing SU8 organic insulator and evaporating Aluminum on the top surface. The leakage current variation dependent on the voltage is measured and illustrated in figure 2.10.

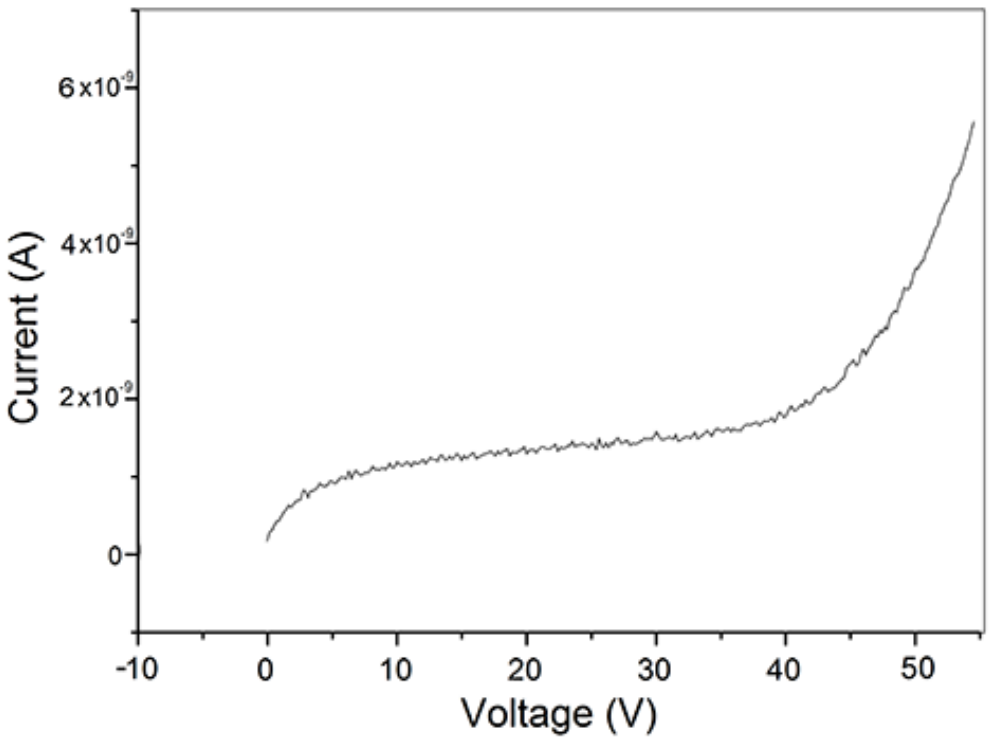

Figure 2.10 The leakage current of the Al/SU8/ITO MIM structure device.

The area of this capacitor is 1 mm^2, where the leakage current is 4 nA at 50 V applied voltage. It means that for the 40/20 μm channel, the leakage current is below than 1×10^{-10}A, which prove that the leakage current of this SU8 organic insulator is appropriate for the Poly-silicon TFT.

2.6 Gate insulator etching for drain/source contact

To connect the drain/source contact with the electrode, the gate insulator must be etched at the drain/source region as shown in figure 2.11. For the inorganic and organic insulator material, the different etching methods will be selected which are introduced in this section respectively.

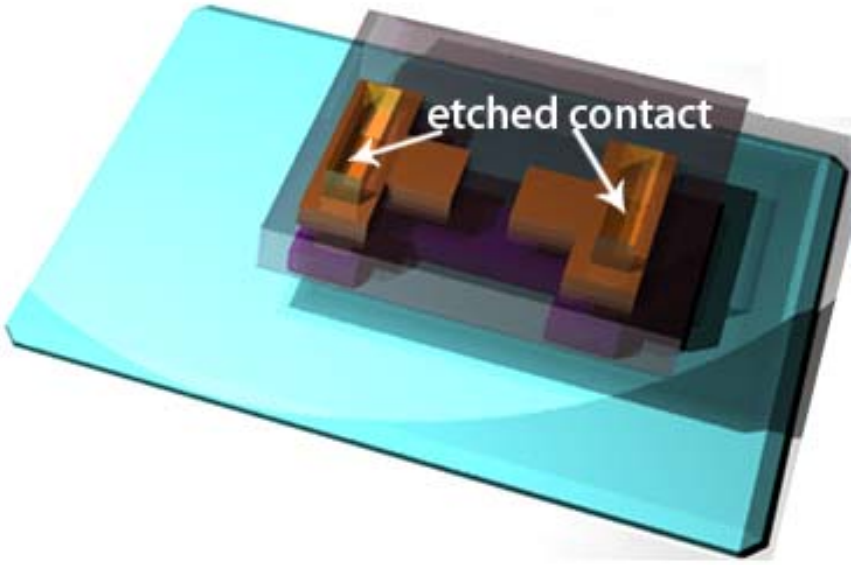

Figure 2.11 Schematic for the etched contact at the drain/source region

2.6.1 Wet-etching on inorganic SiO_2 insulator

In this process, two different processes can usually be utilized again to etch the SiO_2 insulator by SF_6 gas (dry etching) and HF solution (wet etching). Here, the simple HF wet etching process was selected through checking the hydrophobic phenomena of the silicon surface. Meanwhile the over-etching phenomena of the SiO_2 can be controlled under observation of the microscope.

2.6.2 Dry-etching on organic SU8 insulator

As regards of organic SU8 insulator, the only etching method is the RIE etching process. However, the etching plasma gas is O2 which will react with organic material rapidly under plasma state. Therefore, the experimental parameters are shown in the following tables.

Table 2.4 Plasma RIE etching parameters for SU8 organic insulator

Etched material	Reactive gas	Gas flow (sccm)	Pressure (mTorr)	Power (W)	Etching rate (nm/min)
SU8	O_2	30	10	100	≈100

2.7 Transparent AZO (ZnO:AL) electrode depostition by RF sputtering and the etching process for Source/Gate/Drain formation

For the phototransistor, the transparent electrode is the essential part for transmitting infrared light into the photo-sensing component. So the Radio frequency (RF) sputtering method as can be seen in figure 2.12 is employed to deposit AZO transparent electrode due to low-temperature process, stable thin film growth rate, high reproducibility and low cost.

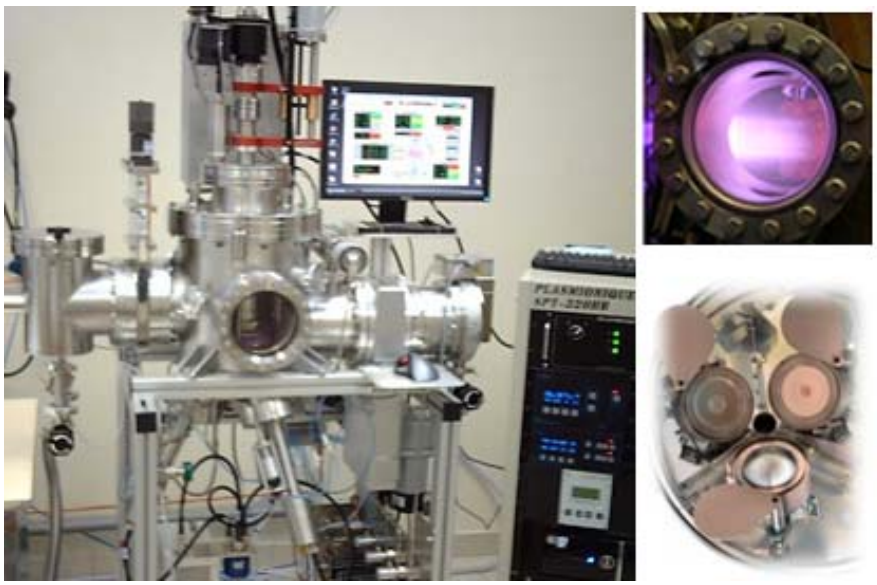

Figure 2.12 RF plasmionique sputtering instrument, the targets' base and plasma glow chamber in this instrument.

In this experiment, the target's size is 250mm × 100mm, the vacuum of this chamber is 10^{-5} Pa, the distance to target is 75 mm and Ar flow volume is 15 sccm. After charging Ar gas, the pressure of the chamber during sputtering is 0.1Pa with 300

W sputtering power. The as-fabricated AZO thin film can be observed by the profile measurement.

Table 2.5 RF sputtering parameters for AZO transparent electrode

Deposited material	Reactive gas	Gas ratio	Pressure	Power (W)	deposition rate (nm/min)
AZO	Ar/O_2	4:1	1 pa	150W	≈5

And the etching solution was used by the same etching buffer solution with same volume formula: 701 H_3PO_4 (85%)+28 HNO_3(70%)+139 CH_3COOH+132 H_2O DI. For the 100nm Al etching, the etching temperature is 50℃ with about 1 min40 s etching time.

But for the AZO transparent electrode etching, the etching temperature is 40℃ with quickly 4.5s etching where the over-etching can be confirmed by the microscope's observation. The final structure of the phototransistor with transparent electrode is depicted in figure 2.13.

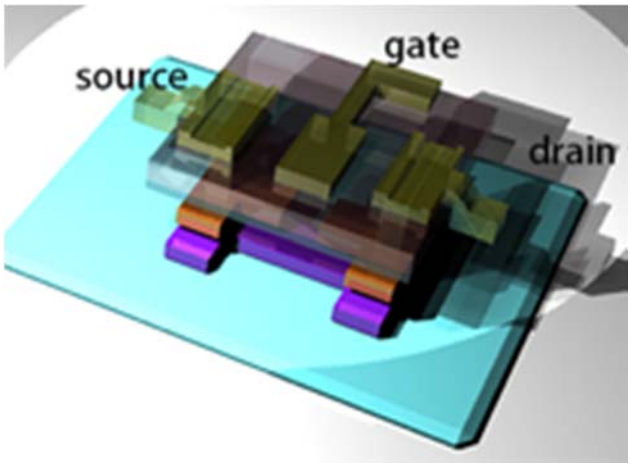

Figure 2.13 Device Schematic for the formed Source/Gate/Drain electrodes.

3. Operating principle and performance for the Poly-silicon TFT

The working principle of TFTs derives directly from the usual MOSFET transistor.

Indeed, TFT is only a Metal-Insulator-Semiconducteur field effect transistor. The only difference is that the active layer is not single crystalline and not doped and the transistor works in accumulation. The off-current is limited by the resistivity of the undoped layer and not by PN junction as for MOSFET. The not single crystalline active layer introduces electrically active defects in the channel lowering the carrier mobility and limiting the swing. Finally, the very low thickness of the active layer leads to closer functioning of TFT to SOIFET than to bulk MOSFET. In particular, the influence of the rear interface can be important. Great care to the cleaning of the substrate before the deposition of the active layer is mandatory.

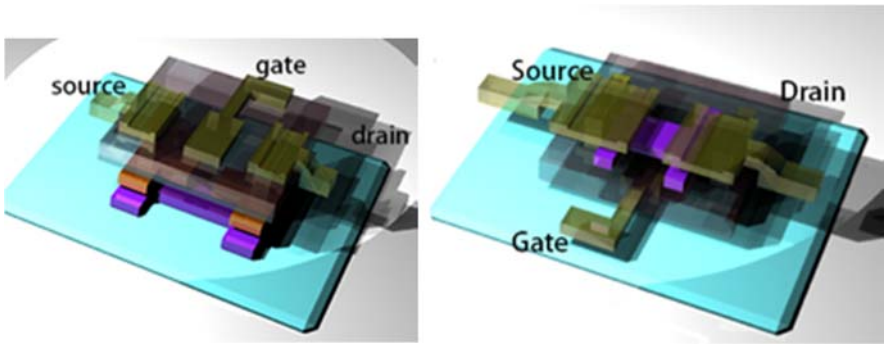

Figure 2.14 The two typical thin film transistors with (a) top-gated and (b) bottom gated structures.

As shown in figure 2.14, based on gate and insulator dielectric, the deposition orders of the TFTs' semiconductors can be distinguished by the top-gate and bottom gate structures. After forming the semiconductors and electric insulator, the deposition of drain/source/gate (D/S/G) electrode are performed simultaneously by metal evaporation processes to realize the definition of the three electrodes terminals, which is the top-gate structure device. Conversely, fabricating gate electrode and then forming the insulator dielectric and semiconductors on substrate by semiconductors deposition processes are termed as bottom-gate structure. In this work, only Top-Gate structure is used.

3.1 Device physics for TFTs

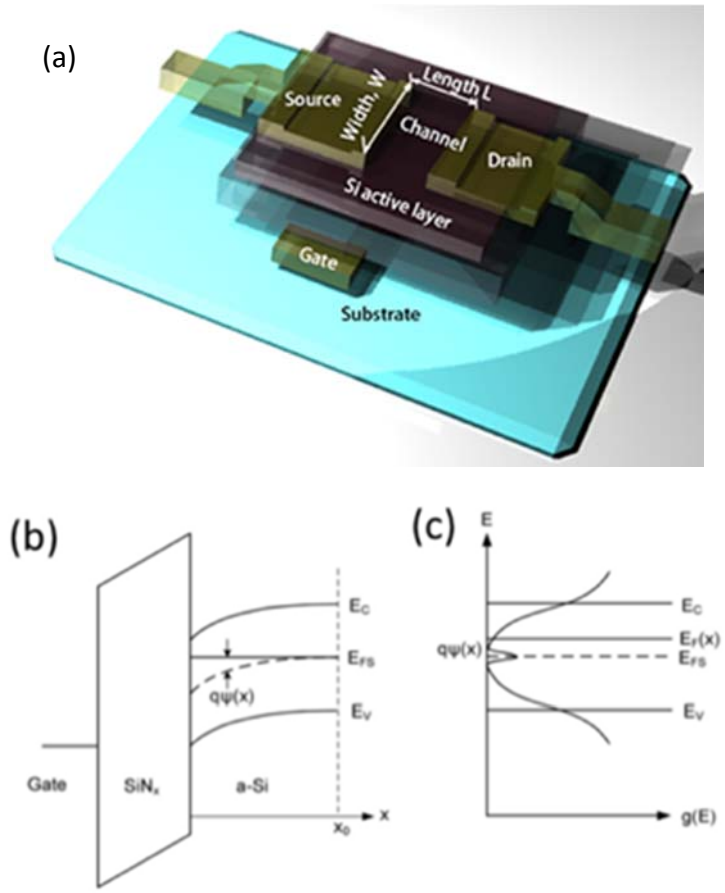

Figure 2.15 (a) The structure parameters for the basic Si thin film transistors. (b) The energy bandgap alignment for TFT. (c) Distribution of Density state.

Figure 2.15 (a) shows the TFT with classical silicon material as channel and the parameters for devices' working principles. W is the width of TFTs' channel, L is the length of channel. The drain-source voltage is applied on the drain electrode, gate voltage is added on the gate electrode and source electrode is connected to ground.

(1) Bandgap bending by gate voltage

Under positive gate voltage's condition, the Fermi energy level close to the interface between insulator dielectric and silicon will bend to the bottom of conduction band. This bending interface can be solved by the Poisson equation:

$$\frac{d^2\psi(x)}{dx^2} = -\frac{\rho(x)}{\epsilon_{si}} \qquad (2.1)$$

where x is the distance between semiconductor silicon thin film and dielectric/active layer interface. The energy band formula at the surface is as following:

$$(x = 0) = \psi_s = V_G - \frac{|Q_n|}{C_{ins}} \qquad (2.2)$$

Where C_{ins} is the capacitance of the gate insulator layer's infinitesimal unite, Q_n is the accumulated charge on the every unite area's gate insulator layer/semiconductor active layer interface caused by gate voltage. The charge Q_n is calculated by the following expression:

$$Q_n = \int_0^{x_0} \rho(x)\,\mathrm{dx} \qquad (2.3)$$

Combining the active layer charge density distribution of Si-semiconductor active layer and energy band's bend can receive the following equation:

$$\rho(x) = -\mathrm{q}\int_{E_{FS}}^{\infty} g(E)f(E - q\psi)\,\mathrm{dE} \qquad (2.4)$$

where $f(E)=\frac{1}{1+\exp(\frac{E-E_{FS}}{kT})}$ is the distribution equation of the Fermi-Dirac:

Thus, the field effect mobility μ_{FET}, can be computed by the bandgap mobility μ_0:

$$\mu_{FET} = \mu_0 \frac{Q_e}{Q_n} = \mu_0 \frac{\int_0^{x_0} \rho_e(x)\mathrm{dx}}{\int_0^{x_0} \rho(x)\mathrm{dx}} \qquad (2.5)$$

(2) Field effect mobility

Field effect mobility is the main parameter for TFT. In semiconductor physics, the definition of mobility is the mean speed of the carriers in unite electric field which expressed the moving rate of the carriers and named as mobility.

For the field effect mobility which can be obtained from the transconductance g_m, the transfer characteristic is similar with MOSFET, so in the Poly-silicon TFT,

$$I_D = \mu_{FE} C_{ins} \frac{W}{L}[(V_G - V_T)V_D - \frac{1}{2}V_D^2] \qquad (2.6)$$

where C_{ins} is the unit area capacitance of gate insulator, W、L are width and length of channel, V_T is the threshold voltage.

When $V_D << V_G - V_T$, $V_G > V_T$, the drain current at linear regime is approximate to :

$$I_D = \mu_{FET} C_{ox} \frac{W}{L}[(V_G - V_T)V_D] \qquad (2.7)$$

The transconductance is defined as:

$$g_m = \frac{\partial I_D}{\partial V_G}|_{V_D=const} = \frac{W}{L} C_{OX} \mu_{FET} V_D \qquad (2.8)$$

Finally, the field effect mobility can be calculated as:

$$\mu_{FET} = \frac{L}{WC_{OX}V_D} g_m \qquad (2.9)$$

(3) Threshold voltage

Both inorganic TFT and organic TFT have threshold voltage, which is the gate voltage from which the transistor can be considered as conducting. Usually, threshold voltage of inorganic TFT is usually approximate 0 V- 15 V and that of organic TFT is usually at 10 V-20 V range. Different insulator materials lead to different device's threshold voltag V_T, the larger dielectric constant of insulator material can cause a small V_T. The thickness of insulator has also a big influence on V_T. Generally speaking, the device with thin insulator thickness has a small V_T. The threshold voltage V_T is as following:

$$V_T = V_s + V_{ms} - \frac{Q_{ss}+Q_B}{C_{ins}} \qquad (2.10)$$

C_{ins} is the unite area capacitance of gate insulator, V_s is the surface potential characterizing the bandgap bending of active layer thin film, V_{ms} is the contact potential offset between gate and active layer, Q_{ss} is the induced charge density arouse by fixed charge, mobile ion carrier and interface state (can be equivalent to the surface state charge) in the insulator layer. Q_B is the surface charge density in the channel. The insulator has the biggest influence on V_T through the insulator thickness, the dielectric constant and the surface morphology.

(4) On/off ratio

In LCD display area, TFTs operate as switch device, which is only working at (on) and (off) states, the two extreme stations. On/off ratio is just one important parameter for device, which stands for the sensitivity of switch speed. Higher on/off ratio stands quicker switching speed. For N-type field effect transistor, when V_{GS} is negative, it is in off-state and I_{DS} is the I_{off} at this time. When V_{GS} is positive, it is in on-state, I_{DS} is called I_{on} at this time. When TFT works at linear region, on-state current is:

$$I_{on} = \frac{W}{L}\mu C_i \left(V_G - V_T - \frac{V_D}{2}\right) V_D \qquad (2.11)$$

When device works at saturation region, on-state current is:

$$I_{on} = \frac{W}{2L}\mu C_i(V_G - V_T)^2 \quad (2.12)$$

When device works at off-state, off-state current I_{off} is:

$$I_{off} = q(n\mu_e + p\mu_p)\frac{Wd}{L}V_{DS} \quad (2.13)$$

where q, n, p, μ_e, μ_p, W, L, d are standing for charge quantity, electron density, hole density, electron mobility, hole mobility, channel width, channel length and active layer channel's thickness. From the on-state and off-state current expressions, we can observe that increasing gate insulator's capacitance density and decreasing active layer's thickness are the effective methods to enhance on-current and constraint off-current.

(5) Subthreshold swing (SS)

Mobility, on/off ratio and threshold voltage are the three main indexes measuring performance of field effect transistors. However, actually the SS factor is another important indicator for TFT. Because this factor is determined by the interface situation between active layer and insulator layer, this interface is the most important interface affecting the performance of the device.

The definition of SS is: under certain drain-source voltage, the required gate voltage increment (∇V_G) for adding one magnitude drain-source current.

$$SS=\frac{dV_{GS}}{d(LogI_{DS})} \quad (2.14)$$

where V_{GS} is gate voltage, I_{DS} is drain-source current.

3.2 TFTs' electrical parameters characterization of typical SiO_2 gated TFTs

The transfer characteristics curve is the corresponding drain-source current versus the gate voltage V_{GS} with constant drain-source voltage V_{DS}. The working region of this transfer curve is divided into four zones. For example, in figure 2.22 the typical transfer curve is divided to cut-off region below -5V, linear region between -5V to 5V where the current increase quickly equivalent to linear curve and the saturated region from 5V to 20V.

Figure 2.16 also shows the transfer characteristics of Poly-silicon TFT gated by previous 100 nm SiO_2 insulator with W/L ratio of 40/20 μ m channel. With this thin 100 nm SiO_2 film gate insulator, the gate leakage current is around 1nA.

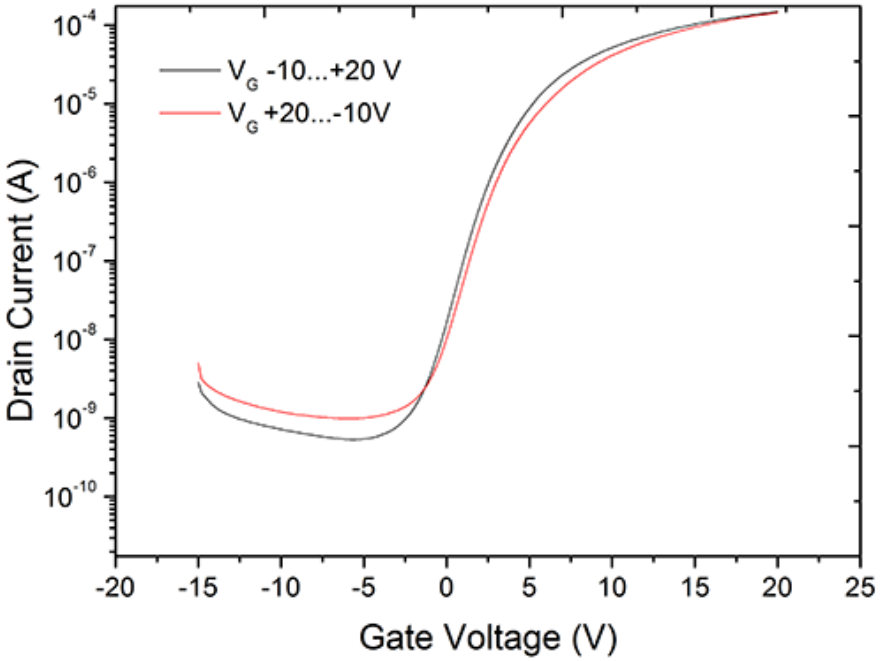

Figure 2.16 Transfer characteristics curve of the w/l=40/20 μ m Poly-silicon TFT and hysteretic curve of this TFT at V_d=1V

Except for this parameter, the other electrical properties of this TFT, such as mobility (μ), Subthreshold slope (S.S.) and threshold voltage (V_{TH}) can be summarized as the followed table:

Table 2.8 Electrical parameters of the SiO_2 insulator gated TFT.

insulator	Mobility (cm2/Vs)	S.S. (V)	V_{TH} (V)	On/off ratio
SiO_2	13	0.67	5.5	~10^6

Meanwhile hysteresis phenomenon is also observed in this transfer characteristic curves. The threshold voltage V_{TH}'s shift is below 0.3V between the 2 curves. From this parameter, it demonstrates the low trap charge density in the active layer, insulator layer and interface for the SiO_2 insulator to provide device's stability.

Figure 2.17 shows the output characteristic curves of Poly-silicon TFT. Through

this output characteristic curve, the saturation regime can be clearly revealed for different gate voltage to show a high saturated current.

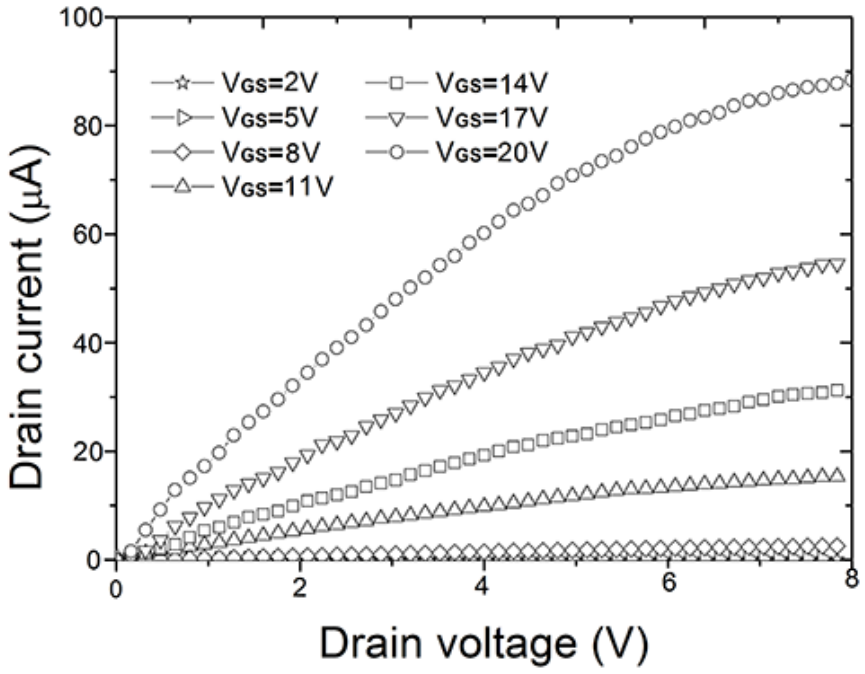

Figure 2.17 Output characteristic curves of SiO_2 insulator gated Poly-silicon TFT

These electrical characterizations of SiO_2 insulator gated TFT exhibit the excellent quality for this Poly-silicon TFT, which is suitable to utilize as the phototransistor due to its high mobility, S.S and threshold voltage. However, because it's impossible to mix the chemical synthesized QDs into SiO_2 insulator directly, it is essential to find some liquid insulator for the future application with mixing QDs.

3.3 TFTs' electrical parameters characterization of Organic SU8 gated TFTs

For the as-prepared SU8 organic insulator gated TFT with 40/20 μ m channel, figure 2.18 illustrates the transfer characteristic curves with a scanning gate voltage from -15 V to 40 V. From this transfer characteristic curves, the leakage current is below 1nA with 300 nm SU8 gate insulator. Moreover, the other electrical parameters of this TFT can also concluded in the following table:

Table 2.5 Electrical parameters of the SU8 insulator gated TFT.

Insulator	Mobility (cm2/Vs)	S.S. (V)	V_{TH} (V)	On/off ratio
SU8	3.1	3.2	22	~10^5

Compared with previous SiO_2 insulator gated TFT, with SU8 insulator, this device has lower leakage current (0.1 nA), but worse mobility, S.S. threshold voltage and one order smaller on/off ratio.

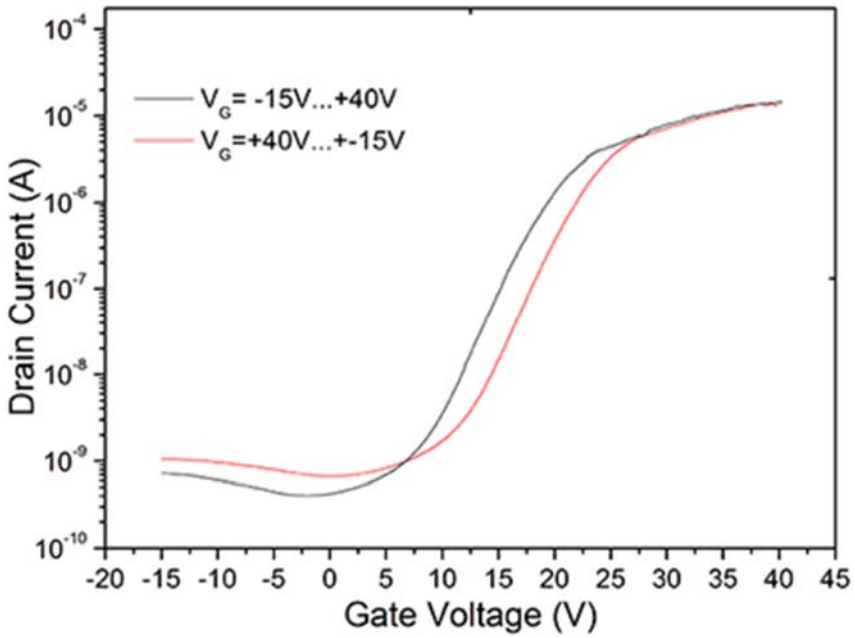

Figure 2.18 Transfer characteristic curve of SU8 insulator gated TFT and hysteretic curve of this TFT at V_d=6V

Meanwhile, through the hysteretic transfer characteristic curve in figure 2.18, the threshold voltage V_{TH} shift is around 2.4V, which is also much higher than the threshold voltage shifts in SiO_2 insulator. All these parameters' comparison provides the proofs that the SU8 as organic insulator has a bad contact between inorganic SiO_2 insulator's interface. Moreover, the SU8 has also more defects and trap-states because the SU8's low temperature spin-coating solution process.

Figure 2.19 depicts the output characteristic curve of this SU8 gated insulator, this

curves also show the saturation region of this TFT under different gate voltages.

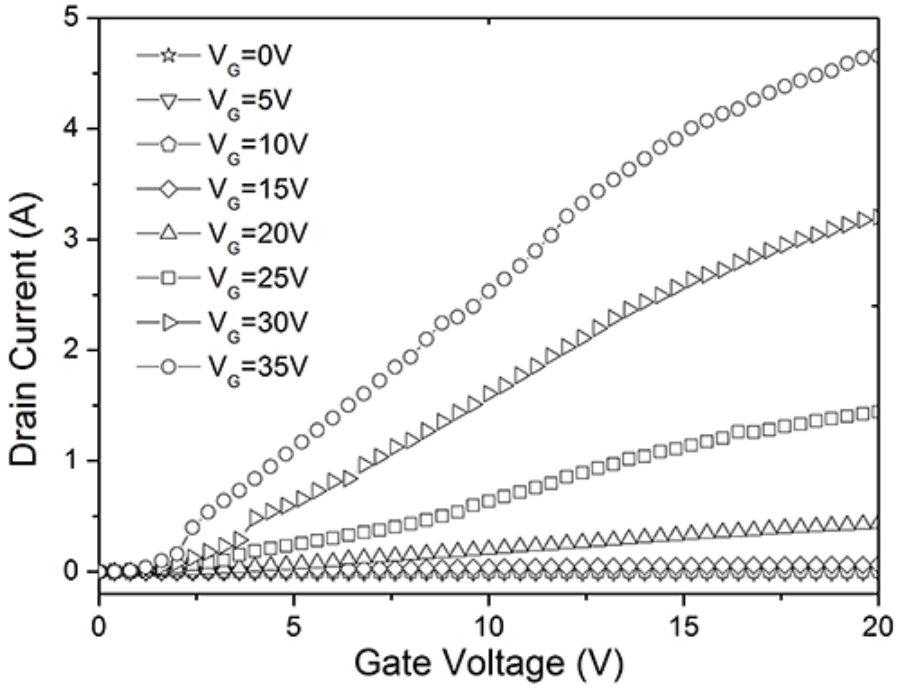

Figure 2.19 Output characteristic curves of SU8 insulator gated TFT

Nevertheless, the SU8 insulator already provides an excellent insulating property, enough mobility, stable TFT's characters, reasonable on/off ratio and subthreshold voltage. Through this verification experiments, the SU8 insulator will be an alternative selection as the TFT's effective insulator. The successive experimental steps are to blend the QDs into this SU8, which will be functionalized as the future photo-sensing hybrid insulator. The detailed analysis of this hybrid insulator including leakage current, photo-generated current and capacitance will be introduced in the chapter 4.

4. Conclusion

In this chapter, these experiments manifest important scientific results, which demonstrates the possibility to constitute the photo-sensing hybrid QDs/SU8 insulator in the Poly-silicon TFT. The as-fabricated Poly-silicon TFT shows excellent electrical characters for supporting the phototransistor such as mobility, on/off ratio, Subthreshold voltage and low threshold voltage. Furthermore, the SU8 organic solution

fabrication process can be compatible to MOSFET and other CMOS fabrication technology. This technology stepped an important progress for the future large-scale micro-electronic phototransistor's processes.

5. Reference

[1] B. H. You, B. J. Lee, K. Lee, S. Y. Han, J. H. Koh, J. H. Lee, S. Takahashi, B. H. Berkeley, N. D. Kim and S. S. Kim, "55.1: 12.1-Inch a-Si:H Tft LCD with Embedded Touch Screen Panel", SID Symposium Digest of Technical Papers, Vol. 39, No. 1, (2009), pp.830–33.

[2] P. Chen, Y. Fu, R. Aminirad, C. Wang, J. Zhang, K. Wang, K. Galatsis, and C. Zhou, "Fully Printed Separated Carbon Nanotube Thin Film Transistor Circuits and Its Application in Organic Light Emitting Diode Control", Nano Letters, Vol. 11, No. 12, (2011), pp. 5301-8.

[3] A. Shin, S. J. Hwang, S. W. Yu, and M. Y. Sung, "Design of Organic TFT Pixel Electrode Circuit for Active-Matrix OLED Displays", Journal of computers, Vol. 3, No. 3, (2008), pp. 1-5.

[4] Y. Yamamoto, "Technological Innovation of Thin-Film Transistors: Technology Development, History, and Future", Japanese Journal of Applied Physics, Vol. 51, No. 6R, (2012), pp. 55-61.

[5] A. Z. Kattamis, I. Cheng, K. Long, B. Hekmatshoar, K. H. Cherenack, S. Wagner, J. C. Sturm, S. M. Venugopal, D. E. Loy, S. M. O'Rourke, and Da. R. Allee, "Amorphous Silicon Thin-Film Transistor Backplanes Deposited at 200℃ on Clear Plastic for Lamination to Electrophoretic Displays", Vol. 3, No. 3, (2007), pp. 304-308.

[6] N. D. Young, G. Harkin, R. M. Bunn, D. J. McCulloch, R. W. Wilks, and A. G. Knapp, "Novel Fingerprint Scanning Arrays Using Polysilicon TFT's on Glass and Polymer Substrates", Vol. 18, No.1, (1997), pp. 19-20.

[7] B. F. Hung, K. C. Chiang, C. C. Huang, and Albert Chin, "High-Performance Poly-Silicon TFTs Incorporating $LaAlO_3$ as the Gate Dielectric", Vol. 26, No. 6, (2005), pp. 384-386.

[8] Y. Jeong, C. Bae, D. Kim, K. Song, K. Woo, H. Shin, G. Cao, and J. Moon, "Bias-Stress-Stable Solution-Processed Oxide Thin Film Transistors", ACS Applied Materials & Interfaces, Vol. 2, No. 3, (2010), pp. 611-5.

[9] O. Bonnaud, T. Mohammed-Brahim, "Poly-Si TFT based technologies and circuits for magnetic, chemical, and bio sensors", ECS Conference, Vol. 33, No.5, (2010), pp.409-418.

[10] T Nogushi, K Sugihara, K Shimoda, T Gushiken, T. Okada, E. Jacques, H. Dong, and T. Mohammed-Brahim, "Poly SI TFTs Formed by Low Temperature Process Using Blue Laser Diode Annealing", the 14th International Meeting on Information Display (IMID 2014), Aug 2014.

[11] A. Girard, N. Coulon, C. Cardinaud, T. Mohammed-Brahim, and F. Geneste, "Effect of doping on the modification of polycrystalline silicon by spontaneous reduction of diazonium salts", Applied Surface Science, Vol. 314, (2014), pp.358-366.

[12] G. Godem-Wenga, E. Jacques, A. –C. Salaün, R. Rogel, L. Pichon, and F. Geneste, "Step-gate polysilicon nanowires field effect transistor compatible with CMOS technology for label-free DNA biosensor", Biosensors and Bioelectronics, Vol. 40, No. 1, (2013), pp.141-146.

[13] C. L. Paven-Thivet, Y. Lu, H.V. Nguyen, R. Benzerg, L. L. Gendre, S. Rioual, D. Benzegoutta, F. Tessier, F. Cheviré, A. Sharaiha, C. Delaveaud, and X. Castel, "Lanthanum titanium perovskite compound: Thin film deposition and high frequency dielectric characterization", Thin Solid Films, Vol. 553, (2014), pp.76-80.

[14] G. Wenga, E. Jacques, A.-C. Salaün, R. Rogel, L. Pichon, and F. Geneste, "Bottom-gate and Step-gate Polysilicon Nanowires Field Effect Transistors for Ultrasensitive Label-free Biosensing Application", Procedia Engineering, Vol. 47, (2012), pp.414-417.

[15] P. Zhang, “Développement et fabrication de transistors couches minces verticaux en technologie silicium polycristallin basse temperature”, Thesis University of Rennes 1, (2012).

[16] A. Barron, “Chemical Vapor Deposition of Silica Thin Films”, OpenStax-CNX Web site. http://passthru.cnx.org/plone/content/m24897/1.4/, Jan 22, 2010.

[17] V. Etten, E. A. Ximenes, E. S. Tarasconi, L. T. Garcia, I. T. S. Forte, M. M. C. Boudinov, H. Boudinov, “Insulating Characteristics of Polyvinyl Alcohol for Integrated Electronics”, Thin Solid Films, Vol. 568, (2014), pp. 111-16.

[18], Y. Jang, D. H. Kim, Y. D. Park, J. H. Cho, M. Hwang, and K. Cho, “Influence of the Dielectric Constant of a Polyvinyl Phenol Insulator on the Field-Effect Mobility of a Pentacene-Based Thin-Film Transistor”, Applied Physics Letters, Vol. 87, No. 15, (2005), p. 152105.

[19] B. J. de Gans, P. C. Duineveld, and U. S. Schubert, “Inkjet Printing of Polymers: State of the Art and Future Developments”, Advanced Materials, Vol. 16, No. 3, (2004), pp. 203-13.

[20] J. Wen-hai, D. Guo-Tong, Y. Shu-kun, W. Wei, C. Yu-Chun, W. Xu, “Organic Thin Film Field Effect Transistors with PMMA-GMA Gate Dielectric”, Vol. 23, No. 7, (2006), pp. 1939-1942.

[21] Q. Cao, M. G. Xia, M. Shim, and J. A Rogers, “Bilayer Organic–Inorganic Gate Dielectrics for High-Performance, Low-Voltage, Single-Walled Carbon Nanotube Thin-Film Transistors, Complementary Logic Gates, and P–N Diodes on Plastic Substrates”, Advanced Functional Materials, Vol. 16, No. 18, (2006), pp.2355-62.

[22] J. B. Kim, C. Fuentes-Hernandez, D. K. Hwang, W. J. Potscavage, and B. Kippelen, “Top-Gate Hybrid Complementary Inverters Using Pentacene and Amorphous Ingazno Thin-Film Transistors with High Operational Stability”, AIP Advances, Vol. 2, No. 1 (2012), p. 012134.

[23] E. Jacques, M. Romain, A. Yassin, S. Bebiche, M. Harnois, T. Mohammed-Brahim, J. Rault-Berthelot, and C. Poriel, “An Electron Deficient Dicyanovinylene-Ladder-

Type Pentaphenylene Derivative for N-Type Organic Field Effect Transistors", J. Mater. Chem. C, Vol. 2, No. 17, (2014), pp. 3292-302.

Chapter 3 Synthesis and Characterization of Quantum dots

1. Introduction

The quantum confinement effect is one of the quantum dots' (QDs) unique opto-electrical characters, and the vital property in nanosicence and its other applications [1-4]. Especially, the size-tunable and the bandgap-modulated ability can regulate the absorbance and PL emission for the materials and devices, which can also change the conventional semiconductor's fabrication processes from "impurity engineering" to "energy-band engineering", through optimizing the fabrication process, precisely controlling reactor conditions and applying electric/magnetic field [5-7]. As a consequence, semiconductor QDs show a great application potential in opto-electric devices such as photo-detectors, photo-field-effect-transistors, solar cells and light-emitting-diodes [8-11].

As for the QDs' synthesis, plenty of researching emphasizes have been put on the group Ⅱ-Ⅵ colloidal quantum dots such as CdS, CdSe and CdTe, previously. However, due to large permittivity constant, Bohr radius (18nm), and size-tunable ability in IR waveband range (800nm-3500nm) [12-14], the group Ⅳ-Ⅵ compound PbS, PbSe and PbTe QDs were emerged as hottest investigated materials in optical-electrical fields [15]. In the case of the QDs' application in opto-electric device, it should have the following characters:

(1) Be characteristic of excellent matchup bandgap or electronic affinity between QDs with other semiconductors in the active layer to guarantee the photo-generated electrons' effective injection to the contact band (CB) of semiconductor active layer.

(2) Be characteristic of extinction coefficient, which can provide wide absorption wavelengths' range and strong absorption intensity.

(3) The oxidation state and excited state of QDs should have well stability and activity to provide effective transfer of photo-carriers.

(4) QDs should have excellent lattice matching with other semiconductors in the

heterostructure's interface.

(5) The redox potential of QDs should be lower which can minimize the free energy's loss during the primary and secondary electron's transfer processes.

In this thesis, PbS QDs with strong absorption in IR waveband were produced by metal oxidation and organic thermal decomposition method to provide multi-sizes and high quantum efficiency PbS QDs for the IR photodetectors' applications. Through changing the organic surface group and optimizing the defects at the surface's ligand, we offer sufficient information for the QDs' integrated phototransistors with IR detecting capability.

2. QDs' properties and synthesis mechanism

QDs as 0-dimension material have a quantum confinement in three dimensions (3-D) and electron's energy also has quantized characters in 3-D which cause all the polarized light can induce the transition for the QDs. Thus, excellent QDs' optical-electrical properties attract many attentions from scientific researchers.

2.1 QDs' properties

When the size of the materials is reduced to small dimension, it will be characteristic of new properties, such as quantum size effect, specific surface effect, dielectric confinement effect, quantum tunneling effect and so on [16-18]. All kinds of these materials can be termed as nanocrystal. These quantum opto-electric properties have been studied by more and more scientists and researchers. In theoretic, the excitons' Bohr radius can be deduced according to the hydrogen-like atom's radius:

$$a_b{}^* = \varepsilon_r(\frac{m}{\mu_m})a_b \qquad (3\text{-}1)$$

a_b is Bohr radius, ε_r is permittivity constant, m is the electron mass, μ_m is reduced mass.

Obviously, QDs belong to nanocrystal and is the material which has a smaller size

within the Bohr radius of its bulk material, where electrons in QDs have a strong interaction with wave function of holes [19]. Thus QDs have unique optical-electric properties of this bulk material. QDs' confinement effect is one of the most notable characters in QDs' properties. When the QDs' size is less than bohr exciton radius, the bandgap of QDs can be increased in width. And the broadened bandgap can be expressed by the following equation:

$$\mathrm{E}_G(QD) = E_g(bulk) + \frac{h^2\pi^2}{2\mu_m r^2} \qquad (3\text{-}2)$$

Where E_g(QD) is the bandgap width of QD, $E_g(bulk)$ is the bandgap of bulk material, μ_m is the reduced mass, r is the radius of QDs.

2.2 QDs' synthesis mechanism

Synthesis of Semiconductor QDs can be done using alternative methods that can be approximately cataloged into physical and chemistry methods. Physical synthesis mainly consists of Molecular beam epitaxy (MBE), ion beam injection, micro-fabrication, mechanic grind and so on [20]. Nevertheless, these fabrication methods need very expensive instruments and high cost experiments. Meanwhile, these QDs' distribution is massive and low density which also limit the future application of QDs. Generally speaking, chemistry method is quite cost-effective and easy to operate which can also achieve high uniform QDs for the future large-scale micro-electronic application. Consequently, colloidal chemistry method is the vital candidate for synthesizing semiconductor QDs. Through precisely controlling of chemistry reaction condition, it can be realized to adjust of the QDs' size, morphology and properties.

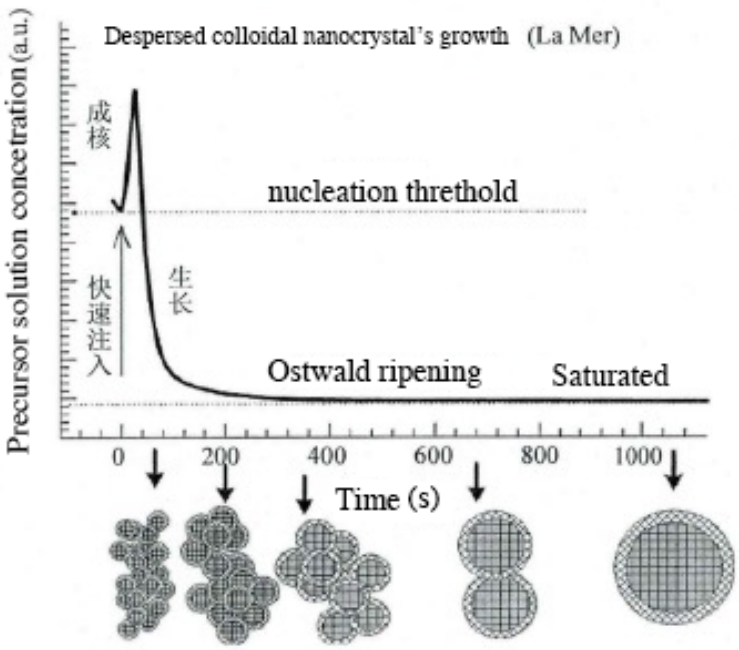

Figure 3.1 dispersed colloidal nanocrystal's nucleation and growth model [21]

Synthesis of Inorganic nanostructure colloidal QDs can broaden new field of the chemistry composition. It can produce Mono-disperse Spherical nanoparticles with modulating the size, morphology, and different compound nanostructure. Researchers can produce sub-10nm metal, semiconductor and magnetic nanoparticles and create shell-core structure, hetero-structure or other complex morphology structure's nanoparticles. In addition, the classical sol-gel colloidal nucleation and growth theory can explain this synthesis [22] in figure 3.1.

Usually, colloidal nanomaterial's synthesis comes from the molecular precursor's reaction where the formation of colloidal nanoparticle can be grown through the processes: nucleation, growth, Ostwald ripening and saturated four sections as shown in figure 3.1. These molecular precursors mainly are inorganic salt and organic metal compound. Synthesis methods are hydrothermal/solvent heating method, hot-injection method, sol-gel method, and co-precipitation method. To guarantee the high quality nanoparticles which are of narrow diameters' distribution, nucleation and growth processes can be separated temporarily. Hot-injection method can be used to obtain high quality nanoparticles through this way. It is used to inject metal-oxide precursor into reaction solvent under high temperature. With the decrease of the temperature,

nucleation and growth methods can be separated temporary to synthesis uniform and narrow distributed colloidal QDs' nanoparticles.

The reactant should be reacted on the anhydrous and anaerobic circumstance when fabricated QDs by hot-injection. Typical reaction process is to insure reaction of precursor under removing water and oxygen. After, pouring the precursor solution into beaker rapidly, continuously reaction of these solvents will produce needed QDs products.

The QDs' synthesis mechanism is: when reactants are added into solutions without water and oxygen, precursor solution will create plenty of crystal core through saturated energy, growth of QDs will continually consume solution's precursor. The growth energy of core ΔG is the sum of surface free energy ΔG_s and volume free energy ΔG_v .

$$\Delta G_v = 4\pi r^2 + \frac{4}{3}\pi r^3 \Delta G^* \qquad (3\text{-}3)$$

where r is the radius of crystal core, γ is surface force or unite area surface energy, ΔG^* is unite crystal core's free energy. Positive ΔG_s is proportional to r^2; negative ΔG_s is proportional to r^3. While these free energy are in competition, when the size of core reach up to critical size r_0, formation energy ΔG will reach to peak:

$$\frac{d\Delta G}{dr} = 8\pi r\gamma + 4\pi r^3 \Delta G^* = 0 \qquad (3\text{-}4)$$

therefore, the radius r_0 can be calculated as expression:

$$r_c = -2\gamma/\Delta G^* \qquad (3\text{-}5)$$

Figure 3.2 is the nucleation and growth process's schematic, when critical size is r_0, ΔG is the threshold energy of core's growth. When the core in the solution is bigger than critical size r_0, bigger ΔG^* is vital influence factor. When ΔG is negative, the particle will grow bigger continuously. Otherwise, the core will disappear when size is less than r_0. The processes can be shown in figure 3.2.

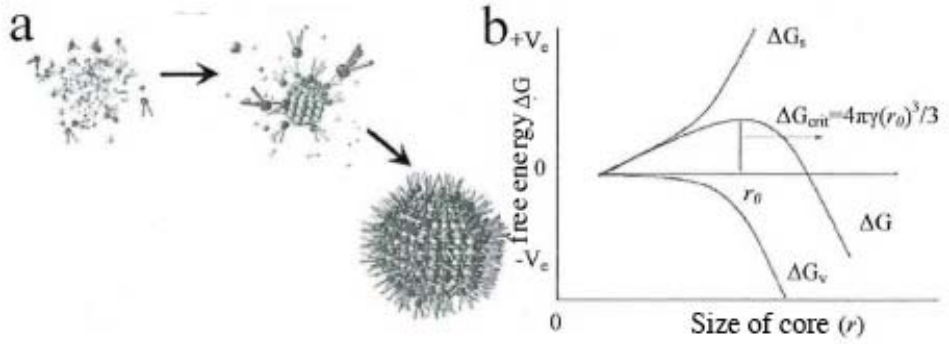

Figure 3.2 (a) Nucleation and growth schematic; (b) relationship of free energy and size's image [23].

When many crystal nucleuses are formed instantaneously, the precursor in previous solution grows gradually. And the growth rate of small crystal nucleus is higher than big crystal core. Due to relatively higher specific surface ratio of small crystal nucleus, it can catch up with growth rate of big crystal core leading to "focus size growth". For this reason, hot-injection method has this advantage. After the optimization of crystal nucleus' growth, the QDs' powder should be collected from solution to obtain optimizing mono-dispersed QDs' nanoparticle. Otherwise the nanoparticle in the solution will enter Ostwald ripening stage. This is the reverse reaction of "focus size growth", which will result in the large distribution of the particles' sizes.

2.3 QDs' carrier's transport mechanism

The carrier transport in QDs can be divided to resonance energy transport, hopping transport and tunnel transport. The ideal mobility of QDs can reach $10^{-2}cm^2/Vs$ [24]. This section will introduce hopping transport and tunnel transport.

Hopping transport is divided into Mott hopping transport and Efros-Shklovshii hopping transport. In some conditions, these two transport mechanisms can be converted with each other. Mott hopping transport depicts the low temperature localized conductivity mechanism in disordered system. The localized charge with E_i energy can be transferred to neighbor energy-state E_j by hopping transport. There are some energy offsets between these energy-states. As a common sense, the space distance r_{ij} and

energy offset ΔE_{ij} can determine the transportation possibility jointly.

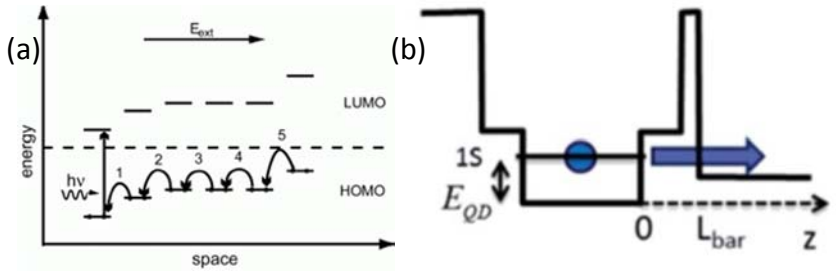

Figure 3.3 Carrier transport schematic, a. hopping transport; b. tunneling transport

When the main reason for the hopping transport is between neighbor QDs (as shown in figure 3.3a), the relationship of conductivity and temperature is the following expression:

$$\sigma = \sigma_0 \exp[-(T_0/T)^1] \qquad (3\text{-}6)$$

When the main reason for the hopping transport is between non-neighbor QDs (as shown in figure 3.3a), the expression for the conductivity and temperature:

$$\sigma = \sigma_0 \exp[-(T_0/T)^{\frac{1}{4}}] \qquad (3\text{-}7)$$

where, $T_0 = e^2/\varepsilon\alpha$, α is the length of localized-state, ε is the permittivity of the material.

Efros-shklovshii hopping transport theory is based on the assuming that quantum localized length is << transport length, ignoring the wave function overlapping area, the expression of conductivity and temperature is as following:

$$\sigma \propto \sigma_0 \exp[-(T_0/T)^{\frac{1}{2}}] \qquad (3\text{-}8)$$

When the energy band offset ΔE_{ij} of hopping transport is equal to Coulomb bandgap Δ, Efros-shklovshii hopping transport will convert to Mott hopping transfer. In the weaker charge-coupling QDs matrix, the coulomb energy band is $\Delta \approx 2E_c$, the energy E_c is needed energy of transporting one charge.

For the Spherical QDs, charge energy E_c can be computed by:

$$E_c = \frac{e^2}{4\pi\varepsilon r} \quad (3\text{-}9)$$

Based on previous analysis, for the conductive ligand, hopping transport theory can be used to research the transport mechanism of pyridine and PANI encapsulated PbS QDs.

However when charge energy E_c (36meV) is beyond hot-activation energy, coulomb bandgap plays dominant role, and the contact between QDs is insulator property. Different with hopping transport, tunneling transport has no relationship with temperature, the charge coupling energy between neighbor QDs can be expressed by:

$$\beta \approx h\Gamma \quad (3\text{-}10)$$

where, h is the plank constant, Γ is the tunneling possibility, tunneling possibility can be expressed by the following equation:

$$\Gamma \approx \exp(-2\pi\Delta x\sqrt{\frac{8m^*\Delta H}{h^2}}) \quad (3\text{-}11)$$

m^* is the effective mass of the carrier, ΔH and Δx are the height and distance of tunneling potential. From above equation, coupling energy is unrelated with temperature. Tunneling possibility and coupling energy will decline exponentially depended on Δx. ΔH and m^* have weaker influence on tunneling possibility and coupling energy. As depicted in figure 3.3b, because the potential height between QDs and the distance are very high, the influence of charge coupling energy between nanoparticles is relatively small. It is a little similar with the hopping transport, when the coupling energy $\beta > 2E_c$, the barrier for the charge transport from coulomb bandgap will decrease, the transport rate of charge will accelerate.

Nowadays, the common passivation of the QDs' surface organic group (ligand) is to use the short-chain molecular to replace the long-chain molecular. The exchange of ligands can minimize the distance between nanoparticles, meanwhile passivated surface can diminish the dangling bond and trap-state. Through this way, the conductivity of the QDs will increase obviously.

2.4 Characterization method and instrument of QDs

QDs' material and embedded device performance has so many characterization tools and instruments. This thesis uses X-ray diffraction (XRD), visible-IR spectrum (Vis-IR) absorbance, photoluminence (PL) emission, Scanning Electron Microscope (SEM) and Tunneling Electron Microscope (TEM) and Time-resolved PL emission decay.

(1) X-ray diffraction (XRD)

XRD can be used to research QDs material phase, crystal structure and crystallization. Meanwhile the Scherrer equation can calculate the QDs' size:

$$D = \frac{0.89\lambda}{B\cos\theta} \qquad (3\text{-}12)$$

Where, D is the particle's size, λ is the wavelength of X-ray, B is the FMWH, and θ is the diffraction angle.

When produce QDs' measuring sample, QDs solution is dropped on the substrate, and it can be used to test after evaporation. Usually, for obtaining high-quality diffraction image, we can repeat the above sampling steps until a thick, uniform QDs layer.

(2) Vis-IR absorbance spectrum

Different materials always have different ligh-absorption characters; Vis-IR spectrum is always utilized to characterize the QDs' absorption properties. When incident photon energy is less than QDs' bandgap, light can be absorbed by QDs. Incident light energy near QDs' bandgap will lead to strong resonance absorbance. And when the incident light's phonon energy is higher than the QDs' bandgap, the absorbance of QDs will increase exponentially. Therefore, the Vis-IR absorption spectrum can also be a method to estimate QDs' size and bandgap.

(3) Photoluminescence (PL) emission spectrum

Optical properties are the most important parameter for the QDs material in

optoelectronics, where PL emission is essential instrument for the optical analysis of this material. Usually, incident light with a lower absorption wavelength is the choice for the excited light of QDs. If the photoluminescence property is excellent, it will achieve a light emission peak with symmetric Gauss distribution. Moreover, PL emission spectrum can characterize the optical property of defects inside QDs. The exist of defect peak can also be characterized. The cause of for defect is the rotten encapsulation by the surface group during synthesis, which will lead to more surface states. In optoelectronics, there are both advantages and disadvantages for the defects. Therefore, PL spectrum is important to analyze the influence of the defects in optoelectronics' performance.

(4) Scanning Electron Microscope (SEM)

When forming thin optoelectronics films containing QDs, layer-by-layer deposition method is always used to create new QDs thin film, diminishing cracks and wholes. SEM is the essential instrument for characterizing the morphology and thickness of thin film. The surface property of sample will be obtained with high energy electron-beam scanning image.

(5) Tunneling Electron Microscope (TEM)

The size, distribution and morphology of QDs material are extremely significant. QDs have the diameters' distribution problem, which is the the relative standard deviation of the diameters' distribution. TEM is the measured mean to analyze QDs' microscope characters. Meanwhile, electron beam diffraction is the diffraction image of QDs. So diffraction image can analyze QDs' crystalline and lattice structure.

The encapsulated organic has serious influence for the TEM testing result. This organic material will be evaporated under electron beam. So before characterizing the properties of QDs, it is necessary to remove QDs' surface group sufficiently and prevent the QDs from agglomeration.

During QDs' sample fabrication process, firstly QDs solution should be dropped

on the copper net covered with carbon film. Then, organic surface group can be washed cleanly by solvent and evaporated for testing.

2.5 QDs' application in optoelectronics

On account of the QDs' confinement effect, semiconductor QDs' energy-band is no longer continuous and is depending on QDs' size intensely. Semiconductor QDs not only have organic material's advantages such as synthesis controllable, solution-process, and large-scale fabrication, but also have new intrinsic properties. For example, absorption and fluorescence spectrum tunable, high fluorescence quantum yield and multi-exciton effect. These characters can expand the application range of the QDs. The present application fields of semiconductor QDs are FET transistor, solar cell, LED and photodetector.

The following contents conclude the application of optoelectronics with the common-used semiconductors QDs.

(1) Semiconductor QDs' application in Field Effect Transistors.

Semiconductor QDs have many unique optical-electrical properties and compatible process with organic material and flexible substrate. Consequently, QDs have a great role in fabricating FET. It has stimulated many interests in developing QDs' FET [25-27].

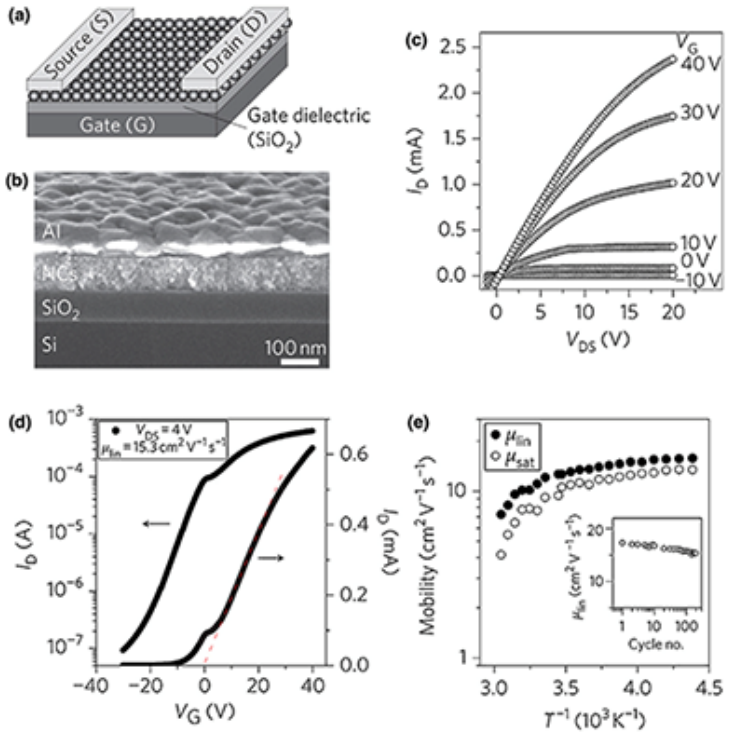

Figure 3.4 The FET schematic, TEM image of cross-section, and characterization for the QDs' channel FET [28].

Especially, with the development of chemical colloid QDs, the solution-process of this QDs layer broadens the device application. Jong-Soo Lee and Maksym V. Kovalenko fabricated the FET device with the colloid QDs and reported it in nature nanotechnology [28]. As shown in figure 3.4, the as-prepared QDs' FET shows high ~10^4 on/off ratio and 15.3 $cm^2 V^{-1}S^{-1}$. Theses experiments shows the bright future for the QDs application in microelectronics.

(2) Semiconductor QDs' application in solar cells.

Semiconductor QDs are of wide absorption range to solar spectrum, excellent carrier transport and other advantages. At the same time, the cost-effective, easily modified and mass productive characters attract many attentions in solar cell's research [8, 9]. It is the promising candidate to substitute traditional solar cell's materials.

At 2011, Prashant V. Kamat fabricated solar cells by hybrid QDs photosensing materials with a high efficiency 5~6% which can approach those of dye sensitized solar cells and organic photovoltaics. With these QDs hybrid, this solar cells also have a wide

absorption wavelengths' range. The biggest problem for the QDs' solar cells is that the charge transfer efficiency between discrete distributed QDs.

(3) Semiconductor QDs' application in light emitting diode.

This application is the most important field for the semiconductor QDs due to the super high quantum and fluorescence yields. Therefore, the application in LED, display and lamination have been researched for a long time [9-11, 29].

T. Kim and K. Cho fabricated QDs LED (QLED) devices and reported in nature photonics at 2013 [29]. Figure 3.5 illustrates the fabrication processes and display screens photography. It demonstrates that QLED is the most promising candidate for the future display to substitute the traditional LCD and OLED displays, if the last engineering weakness of QLED can be solved, such as large power consumption and high driving voltage.

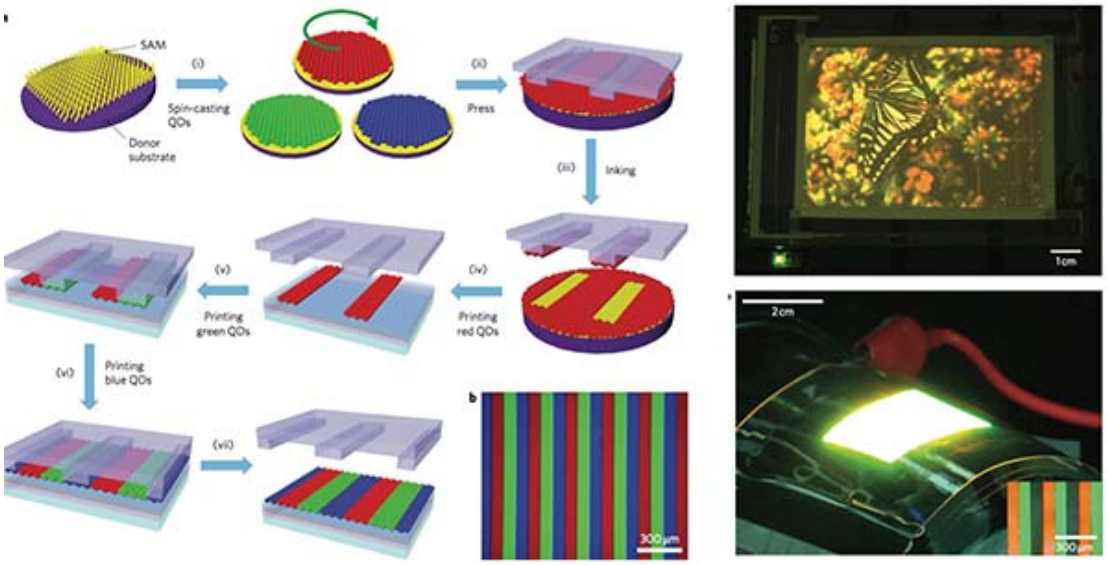

Figure 3.5 The fabrication processes for the QLED and the demonstrate photography of QLED screens and flexible illumination [29].

(4) QDs' application in photodetector (QDIP) has been introduced in chapter 1 in detail.

3. Synthesis details of PbS QDs

3.1 Materials and instruments for experiment

The detailed experiment medicines, materials and instruments are lead oxide (PbO, 99.9%), oleic acid (OA), 1-octadecane (ODE), and hexamethyl-Disilathiane (TMS, Bis (trimethylsilyl) sulfide), which are all purchased from Sigma-Aldrich company. All the solvents, Butyl acetate, methanol, isopropanol, acetone, n-Hexane, and ethanol were purchased from Sinopharm company. The experimental instruments are involved of three-necked flask，condenser reflux tube, centrifugal tube, sample bottle, syringe, dropper and magnetic stirrer machine.

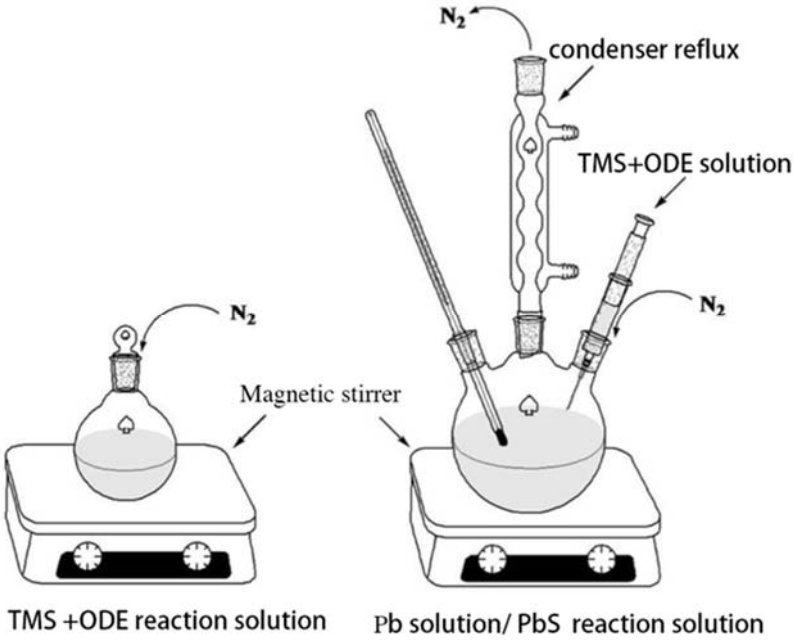

Figure 3.6 The experimental instruments of the PbS QDs' synthesis

During this experiment, PbO and TMS are the resources of lead and sulfur elements, OA organic is the surfactant for the reaction. The PbS colloidal QDs can be synthesized by the hot-injection method. The experiment schematic can be illustrated in figure 3.6, where the experiment is operated under Nitride (N_2) gas' protection.

3.2 Synthesis process for PbS QDs

For the growth of PbS QDs, 2mmol PbO, 5mmol OA and 12.7 ml ODE can be added into 50ml three-necks round-bottom flask. The mixture solution can be stirred under N_2 gas and heated to 180℃. Firstly, pump the reaction instruments under vacuum

for 3 times (20 min every time) and charge N_2 gas for 5min. After guaranteeing that there is no oxygen inside, the reaction temperature will reach up to 180℃ until PbO is dissolved totally into solution. With decrease of temperature to 140℃, 0.25ml TMS, 1.77 ODE mixture solution will be infused in the reaction solution and stirred for mixing completely. Then, 5ml n-Hexane solution should be poured inside and the whole reaction solution are transferred into room temperature water bath. After the solution's temperature is lowered down to RT, 1:2 volume ratio isopropanol/acetone hybrid solution was used to clean QDs. Through centrifugation at 7000 rpm rate during 5 min for three to four times, another methanol/acetone blended solution can be used to centrifuged again. Finally, cleaned QDs can be collected and be put into vacuum 60℃ drying box for 10 hours.

4. Characterization of Infrared-PbS QDs

After collected PbS QDs is emptied into n-Hexane solvent, it can be dispersed by sonic and dropped on the copper net. This sample is observed through tunneling electron microscope (TEM) and high-resolution tunneling electron microscope (HRTEM), after dry the PbS QDs coated copper net. As shown in figure 3.7a, the size of PbS QDs are approximately the spherical nanoparticles with uniform 5nm diameter and well dispersed in the solution.

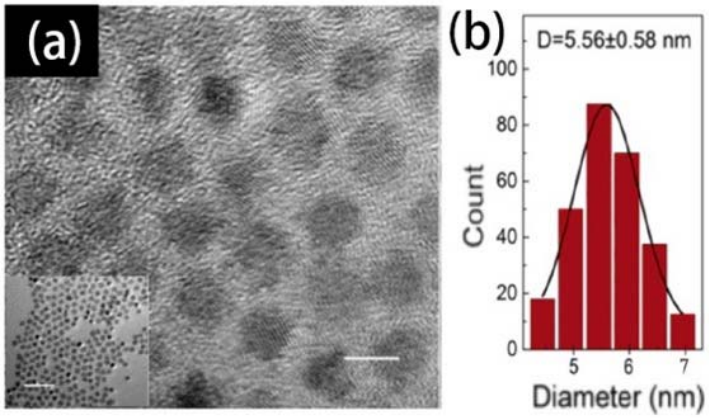

Figure 3.7 (a) HRTEM imgae of the PbS QDs scale bar: 5nm and overall image

(inset), scale bar: 20nm. (b) The statistic size of the 240 PbS QDs.

The PbS QDs are well dispersed in the toluene solution and can be spin-coated into the substrate through solution-process. Figure 3.8 (a) illustrates the cross-sectional morphology of the QDs layer through spin-coating process. The spin-coating parameters are: 1000 rpm speed, 1000 rpm accelerated rate and 30s duration. The thickness of the QDs layer is around 30nm as shown in the SEM characterization. And the compound of the QDs can be measured through the EDS spectrum testing inside. Except for the Si/O elements from substrate components and the residual element C inside EDS detector, the obvious Pb and S elements can be obtained as an approximate 1:1ratio.

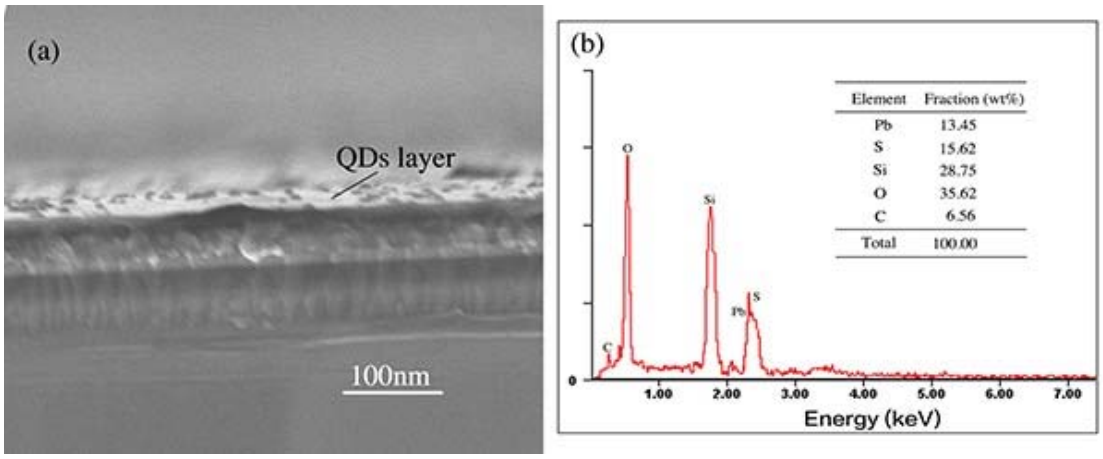

Figure 3.8 (a) The cross-sectional SEM image of spin-coated QDs layer in the oxidized silicon wafer. (b) Compound measurements of the PbS QDs through attached EDS spectrum in the SEM.

X-ray diffraction (XRD) could be utilized to characterize the crystal orientation signal of PbS QDs and the result can be depicted in figure 3.9. And the diffraction peaks of XRD spectrum are 111, 200, 220, 311, 222, 400, 331, 420, 422, 511 which is in correspondence with the typical 2θ degrees standard cards of PbS (JCPDS Card No 65-9496). The XRD results shows this material is typical PbS QDs. The previously introduced Scherrer equation can also be used to get the diameter of the QDs, which is calculated about 5.6nm, through the degree's distribution in the XRD image.

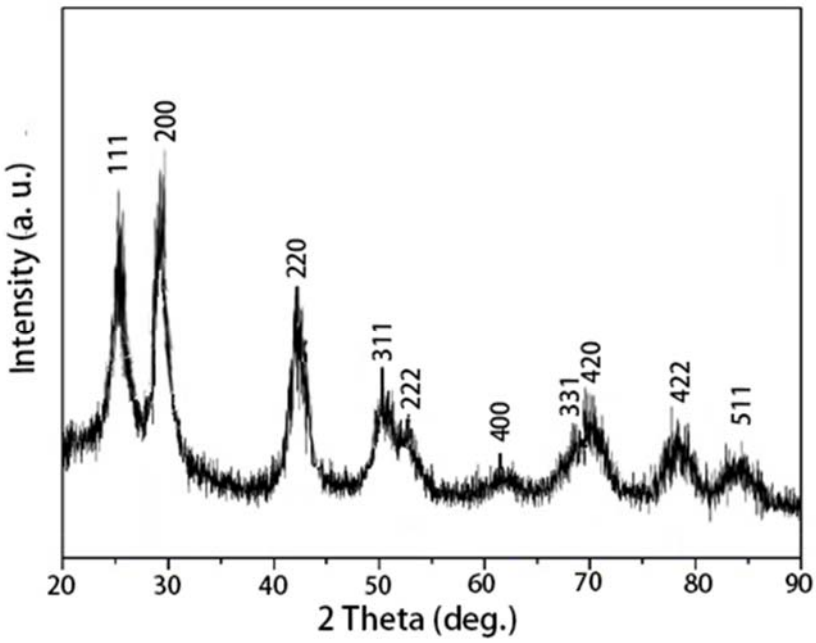

Figure 3.9 XRD spectra measurements' image of PbS QDs

Figure 3.10 shows the infrared absorbance and PL emission spectrum for the as-prepared PbS QDs. From the absorbance spectrum, the peak wavelength of the absorbance is in 1380nm, while the emission peak is 1400nm due to a red shift for the PL spectrum. This characterization shows a narrow bandgap (0.8eV) which has a wide potential in the application of the IR detection.

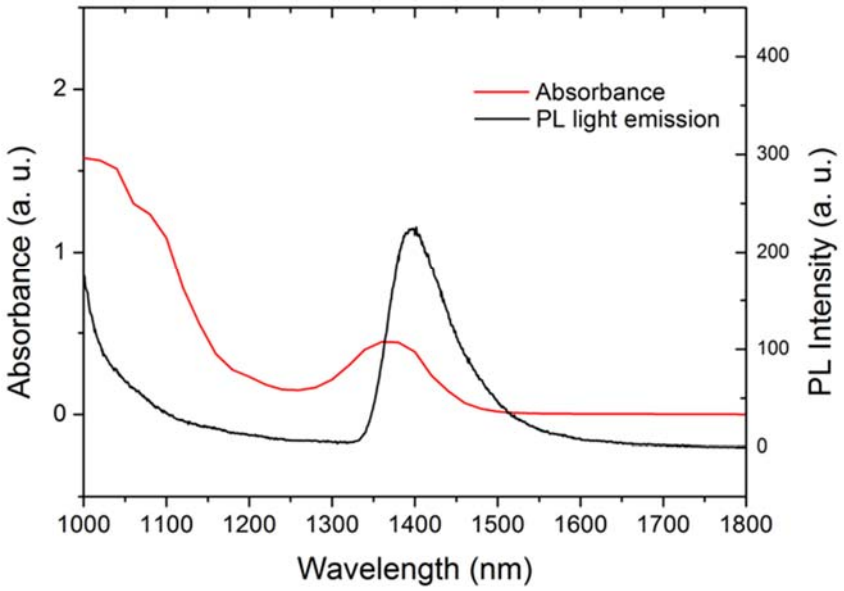

Figure 3.10 IR absorbance and PL emission intensity of the PbS QDs

5. Ligand exchange experiments of QDs

As description above, the ligand of QDs is the charge tunneling channel and bonding connection between QDs and other components (which can be insulator, semiconductor or metal). Many research proved that high temperature dealing can remove the organic surface group. While, obvious aggregation phenomenon of QDs will emerge due to the lack of ligand. That's also one reason that chemical colloid QDs are usually adapted to the room temperature solution process for fabricating optical-electrical devices.

5.1 ligands of QDs

Usually, there are some common used organic surface groups for the inorganic ODs. Firstly, the most common used organic ligand is the long-chain hydro-carbon (H-, C-) molecular. This ligand's encapsulating method is usually carried out at the same time during QDs' synthesis process. With this ligand, the QDs can form the uniform stable solution with hydrophobic and insulation (σ--10^{-12}-10^{-9} Scm^{-1}) property and this ligand can be illustrated in figure 3.11.

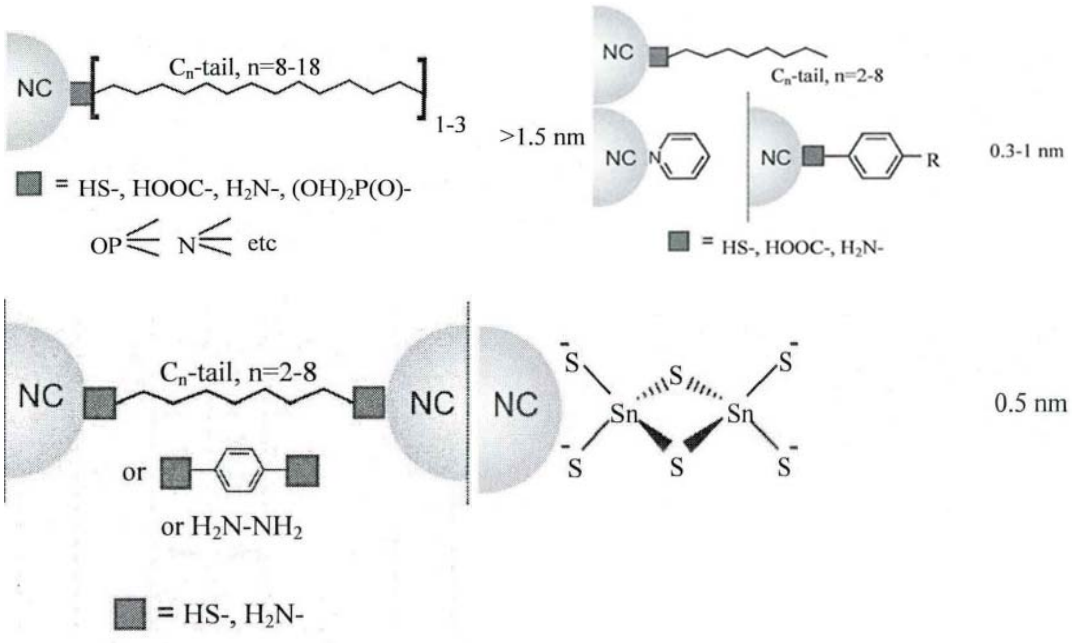

Figure 3.11 The typical four kinds of ligands for QDs with the chemical formulas and the lengths.

Other ones are the short-chain hydro-sulfur (H-, S-) and benzene ring's ligand which can be used for the passivation of the solid-state thin film and ligand exchange for liquid-state surface group. Through this ligand passivation process, the stability of nanoparticles' disperse in the solution and bonding with other semiconductors can be promoted. Meanwhile, the mobility of the material will be promoted and the conductivity of the metal nanocrystal will reach up to 10^{-1} Scm^{-1}.

5.2 ligands's exchange experiment of QDs

In our thesis, to pursue effective charge transfer from QDs, the ligand exchange experiment was carried out to replace OA ligand (>2.5nm), due to the long-chain molecular OA ligand and the low conductivity. The previous mentioned short-chain molecular, well conductive pyridine ligand (0.4nm) was used here for the PbS QDs. Firstly, PbS QDs with OA ligand was synthesized during the chemical growth of the QDs as precursor for the other different PbS QDs (as described in the prevous QDs' synthesis' section). And then the ligand exchange processes were used as follow to check the conductivity of QDs with different connected ligands

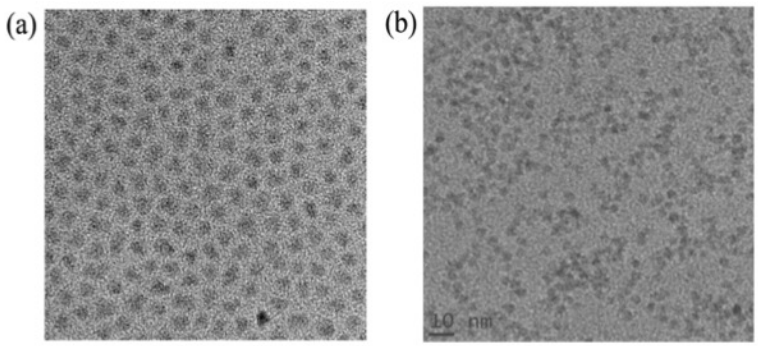

Figure 3.12 SEM image of the OA-encapsulated and pyridine-capped QDs after ligand exchange process

The detailed ligand exchange procedure of QDs is:

(1) The OA capped PbS QDs were dispersed in toluene (150mg PbS; 2mL), which was poured into the 10mL of pyridine in the flask. This blended solution system was vigorously bubbled with N_2 gas for around 15min. After 1 hour slowly stirring in the 70℃ oil bath solution was heated (70°C, 1 h), the mixture was centrifuged down with 6000 rpm during 30s.

(2) After centrifuging the mixture again, the collected precipitate was pyridine capped PbS QDs, which was re-dispersed in toluene by means of sonication for 2 hours at room temperature as shown in figure 3.12.

(3) Two steps of synthesizing PbS (QDs@PANI): the first step is to prepare tailored QDs: the TOPO ligands capping on the PbS QDs are added in the chloroform solution for stirring during 2h at room temperature. The QDs were exchanged with potassium 4-formyldithiobenzoic acid ligands, which form a dithionate bridge between the QDs and the ligand.

(4) Then, to form the poly-aniline (PANI) encapsulation on the PbS QDs, the aniline tetramer solution was added to the tailored QDs. The aniline tetramer in the oxidation state of emeraldine was prepared and added into the aldehyde-functionalized PbS QDs with a certain concentration (50mg, 0.15mmol). The solution was refluxed overnight under an inert atmosphere. The collected black solid precipitate is the PANI capped PbS QDs after the filtered and washed repeatedly with methanol, chloroform to extract non-reacted tetramer and non-

grafted aldehyde ligand.

5.1 Simulation and Characterization of QDs encapsulated with different ligand

The ligand of QDs is not only the bonding connection between QDs or QDs/other semiconductors, but also playing vital role for transferring carriers. Before testing the QDs with different ligands' performance by practical experiments, we performed the simulation by computer and the software MULTIPHYSICS 5.0. The electric field can be computed by the finite element method (FEM). The process of the simulation is: modeling the device->border conditional set up->meshing division->Numerical compute. The calculating model and the setting parameter can be referenced by the process level in the experiment. The detailed parameter can be set up illustrated in the figure 3.13, the distance of the QDs and semiconductor is 1.2nm. The property of the ligand can be set by two types, where one is the insulating-ligand, another one is the conductive-ligand. Meanwhile, the light-on upon the QDs layer can also create the built-in electric field inside this model, which can also be simulated here.

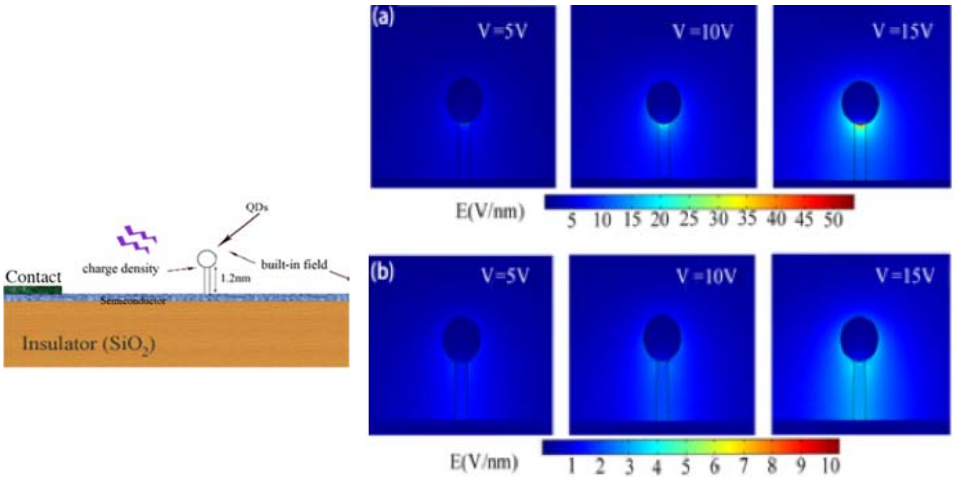

Figure 3.13 Simulated enhanced built-in electric field in QDs/conductive-ligands/semiconductor and QDs/insulating-ligands/semiconductor in light and in darkness(20V).

During the simulation, the voltage can be applied as different values where the distribution of electric field can be calculated and shown in figure 3.13. Based on this

FEM analysis, the conductive ligand has much more uniform electric distribution which will benefit the charge transfer along the ligand. It shows with better conductivity and narrow bandgap ligand, it can bring about more efficient carrier's transport. However, for the QDs' application in the semiconductors, the above static electric field simulation is not sufficient for instructing the further experiment. Figure 3.14 shows the model of the QDs layers' conductivity testing. The semiconductor module in COMSOL 5.0 is carried out to simulate the current along the QDs' layer, where the parameters of the semiconductor layer are N-type doped model and setting up by the properties of the QDs layers with different ligands.

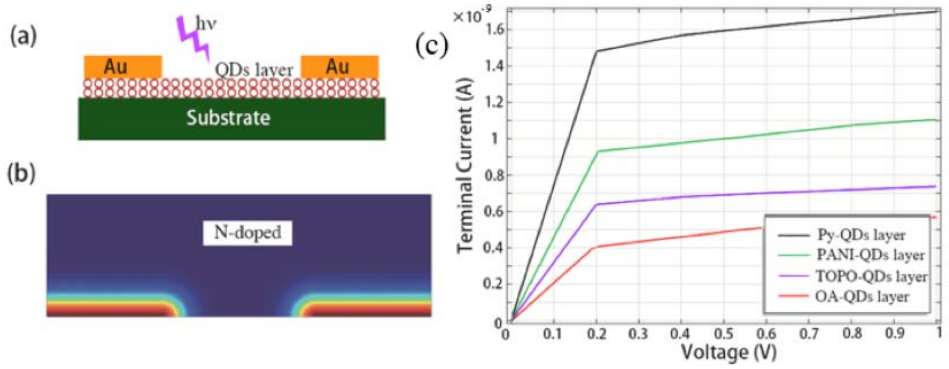

Figure 3.14 (a) The QDs' conductivity testing model schematic. (b) The set up of the N-doped semiconductor layer between the two contact. (c) The simulated current verse applied voltage of the semiconductor layer.

As shown in figure 3.14, the ODs' film on the substrate can be treated as continuous layer for the experiment. The semiconductor planar diode model is built as shown in figure 3.14 (a), where two electrodes is set on the N-doped CdSe substrate. And this border is set up by the continuous contact and the typical material parameters can be arranged as concluded here for the simulation.

Table 1. The typical material parameters summarized in this table [30-34]

	PbS	Pyridine	PANI	TOPO	OA
Conductivity (ε, S/cm)	0.25	$\sim 10^{-8}$	$\sim 10^{-9}$	$\sim 10^{-10}$	$\sim 2\times 10^{-10}$
permittivity	190	12.5	~30	2.6	2.5

Bandgap (eV)	0.4	6.5	1.8	8.5	9.6
Length (nm)	n/a	0.4	>4	1.5	2.5

As illustrated in the figure 3.14(c), the calculated distribution of the terminal current shows the higher conductive, permittivity and low bandgap material play vital roles in generating a better mobility and current for the planar diode. Nevertheless, this semiconductor module can not take into consideration of the practical electron tunneling in the insulating ligands such as TOPO and OA organic surface group.

Consequently, spin-coating process was used to form the QDs layer on the substrate. The gold metal was sputtered on the substrate to form the 50 μm×50 μm area diode and the current density (J-V curve) of the QDs with different ligands are drawn as the following figure 3.15.

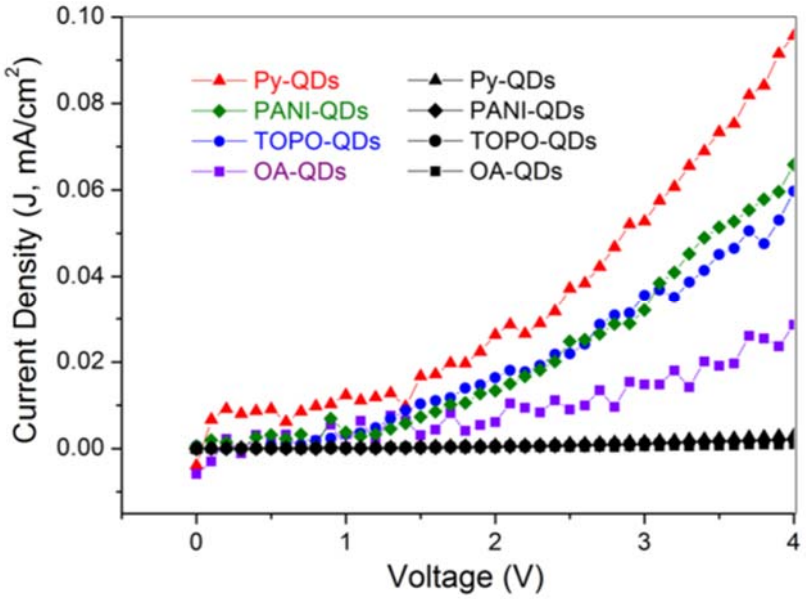

Figure 3.15 J–V characteristics of the PbS diode dependent on applied voltage with different ligand under dark and white light illumination.

As indicated in the J-V curves of PbS diode, pyridine QDs have a best conductivity short-chain molecular and mobility for the QDs layer and achieve a better current density for the diode. The short-chain TOPO insulating ligand shows a similar current density with PANI capped device maybe due to the electron's tunneling from the enhanced electric field. However, because in our synthesis process, TOPO has many defects and trap-states, they will trap the carriers and deteriorate charge transfer

efficiency. Thus, pyridine ligand was selected for encapsulating PbS QDs to pursue a more effective charge transfer.

6. Characterization of PbS QDs and QDs/SU8 hybrid material

For our thesis, epoxy based ink SU8 was employed for the gate insulator of TFT and the QDs were input inside SU8 for the formation of the photo-sensing hybrid insulator. Uncrosslinked SU8 2000 series photoresist (Bisphenol A Novolak epoxy) was used in this work. It is an oligomer formed of eight benzene rings and eight epoxy groups with low molecular weight (around 7KDa) diluted in cyclopentanone. By using photoacid generators, Su-8 can be polymerized and crosslinked into an infinite network. Cationic ring opening reaction is achieved under UV light exposure.

In this chapter, the IR absorbance of QDs alone, SU8 alone and the mixture of QDs and SU8 was measured. The final purpose was to detect the absorption of the hybrid material and confirm the charge transfer experiment phenomenon.

The detailed experiment is:

For the QDs film, the QDs solution was spin-coated at 1000rpm during 30s with 1000rpm accelerate. Then the film was baked at 180℃for 10min. The final thickness of the QDs film can be illustrated in figure 3.8 is about 25nm.

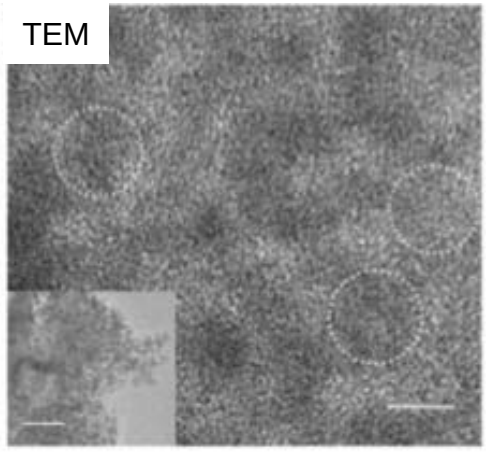

Figure 3.16 HRTEM and TEM images of mixed QDs/SU8 hybrid insulator to show the well QDs distribution inside.

SU8 organic insulator alone and QDs-SU8 mixed solution were spin-coated at

2500rpm (accelerate 3000rpm) during 30s, then soft-baked at 95°C during 90s, exposed during 70s to UV light and finally baked at 95°C during 90s. The final thickness of the formed film is 400nm. And the well distribution of QDs inside this hybrid insulator solution can be confirmed in figure 3.16.

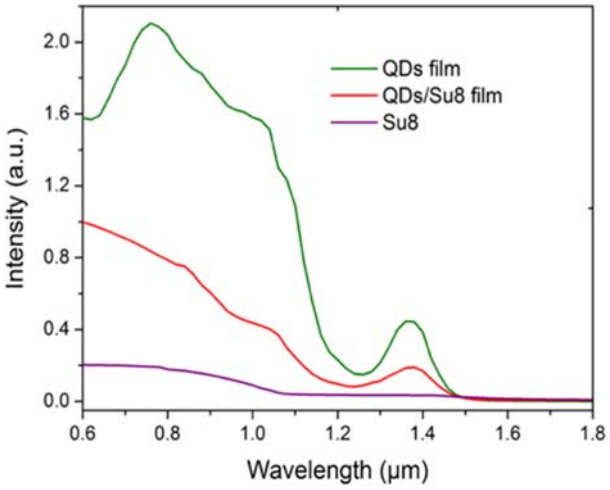

Figure 3.17 IR absorbance for the QDs film, QDs/SU8 hybrid and SU8 materials

As illustrated in figure 3.17, IR absorbance of QDs, QDs/SU8 hybrid and SU8 materials was measured for the stead-state absorption. For SU8 insulator, it doesn't have any absorption in the IR waveband, which is nearly transparent in this detection range. High absorbance is detected in the same wavelength range for QDs alone film. As expected this film presents an absorbance peak at less than 1.4 μm. For the QDs/SU8 film, the absorbance spectrum is similar to the QDs alone film one. However, the absorbance of this hybrid organic insulator-QDs material is weaker. The presence of absorbance with weaker amplitude indicates that there are charges' transfer process between QDs and SU8 interface. As mentioned before, the carrier can move out of QDs' core through tunneling mechanism and captured in the SU8 insulator. Thus one hypothesis is that maybe the PL quenching effect is happened here which cause a weaker absorbance here.

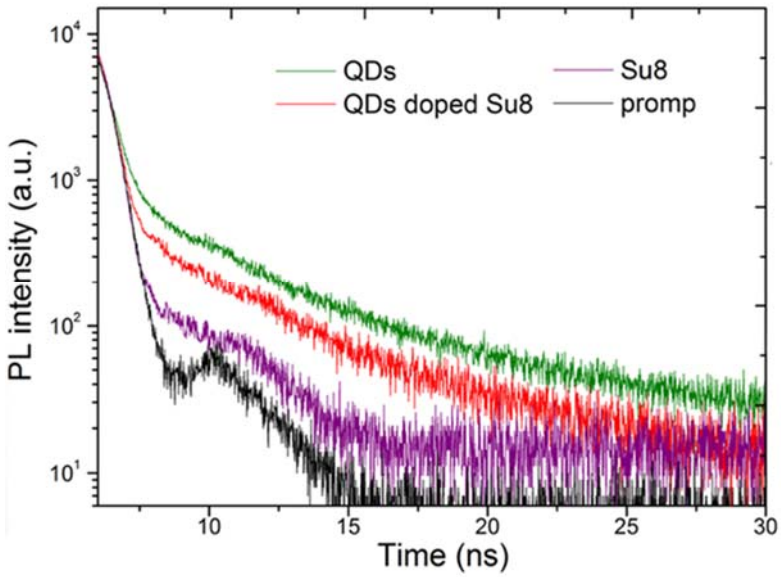

Figure 3.18 Time-resolved PL emission decay of QDs, SU8, and QDs/SU8 three different materials

Figure 3.18 presents the time-resolved PL spectrum of the 3 films, QDs alone, SU8 alone and the mixture of QDs and SU8. The declined PL emission decay can be expressed by the 1 exponential function: $\mathrm{I}(t) = \mathrm{A}\exp\left(-\frac{\mathrm{T}}{\tau}\right) + \mathrm{B}$

The fitting parameters (τ) are 1.65ns, 1.35ns and 0.21ns for QDs, QDs-doped Su8 and Su8 layer. Combined the absorption curves with the time-resolved PL spectrum, it can be observed that the quenching effect was happened between Su8 and PbS QDs, which cause faster decay and weaker absorption (as shown in figure 3.17 for the incident light).

7. Conclusion

This chapter introduces the fabrication process and characterization of the PbS QDs, providing the detailed characterization for the PbS QDs. Meanwhile, the significance evidences and physics mechanism of the ligands' exchange, experiment method and optical-electrical performance were described. Through optimization of the PbS QDs combined with the researching progresses of optoelectronics, appropriate PbS QDs

with effective surface organic group were fabricated and designed for the photodetector' material system and device structure.

8. Reference

[1] E. O. Chukwuocha, M. C. Onyeaju, and T. S. T. Harry, "Theoretical Studies on the Effect of Confinement on Quantum Dots Using the Brus Equation", World Journal of Condensed Matter Physics, Vol. 2, No. 2, (2012), pp. 96-100.

[2] J. Drbohlavova, V. Adam, R. Kizek, and J. Hubalek, "Quantum Dots-Characterization, Preparation and Usage in Biological Systems.", International Journal Molecular Sciences, Vol. 10, No. 2, (2009), pp. 656-73.

[3] K.E. Andersen, C.Y. Fong, and W.E. Pickett, "Quantum confinement in CdSe nanocrystallites.", Journal of Non-Crystalline Solids, Vol. 299, No. 302, (2002), pp. 1105-10.

[4] E. O. Chukwuocha, and M.C. Onyeaju, "Effect of Quantum Confinement on The Wavelength of CdSe, ZnS and GaAs Quantum Dots (QDs)", International Journal of Scientific & Technology Research, Vol. 1, No. 7, (2012), pp. 21-24.

[5] Edward B. Stokes, Adrienne D. Stiff-Roberts, and Charles T. Dameron, "Quantum Dots in Semiconductor Optoelectronic Devices", The Electrochemical Society Interface, Vol. 15, No. 4, (2006), pp. 23-27.

[6] L. Bakueva, I. Gorelikov, S. Musikhin, X. S Zhao, E. H Sargent, and E. Kumacheva, "Pbs Quantum Dots with Stable Efficient Luminescence in the near-Ir Spectral Range", Advanced Materials, Vol. 16, No. 11, (2004), pp. 926-29.

[7] V. A. Fonoberov, and A. A. Balandin, "ZnO Quantum Dots: Physical Properties and Optoelectronic Applications", Journal of Nanoelectronics and Optoelectronics, Vol. 1, No. 1, (2006), pp.19-38.

[8] T. Ribeiro, T. J. V. Prazeres, M. Moffitt, and J. P. S. Farinha, "Enhanced Photoluminescence from Micellar Assemblies of Cadmium Sulfide Quantum Dots and Gold Nanoparticles", The Journal of Physical Chemistry C, Vol. 117, No. 6 (2013), pp. 3122-33.

[9] P. V. Kamat, "Boosting the Efficiency of Quantum Dot Sensitized Solar Cells through Modulation of Interfacial Charge Transfer", Accounts of Chemical Research, Vol. 45, No. 11, (2012), pp. 1906-15.

[10] H. –M. Kim, J. –H. Youn, G. –J. Seo, and J. Jang, "Inverted Quantum-Dot Light-Emitting Diodes with Solution-Processed Aluminum–Zinc Oxide as a Cathode Buffer", J. Mater. Chem. C, Vol. 1, No. 8 (2013), pp. 1567-73.

[11] M. Molaei, M. Marandi, E. Saievar-Iranizad, N. Taghavinia, B. Liu, H. D. Sun, and X. W. Sun, "Near-White Emitting QD-LED Based on Hydrophilic CdS Nanocrystals", Journal of Luminescence, Vol. 132, No. 2, (2012), pp. 467-73.

[12] S. A. Gomes, C. S. Vieira, D. B. Almeida, J. R. Santos-Mallet, R. F. Menna-Barreto, C. L. Cesar, and D. Feder, "CdTe and CdSe Quantum Dots Cytotoxicity: A Comparative Study on Microorganisms", Sensors (Basel), Vol. 11, No. 12, (2011), pp. 11664-78.

[13] B. O. Dabbousi, J. Rodriguez-Viejo, F. V. Mikulec, J. R. Heine, H. Mattoussi, R. Ober, K. F. Jensen, and M. G. Bawendi, "(CdSe)ZnS Core-Shell Quantum Dots: Synthesis and Characterization of a Size Series of Highly Luminescent Nanocrystallites", Journal of Physical Chemistry B, Vol. 101, (1997), pp. 9463-75.

[14] K. Koc, F. Z. Tepehan, G. G. Tepehan, "Characterization of MPS capped CdS quantum dots and formation of self-assembled quantum dots thin films on a glassy substrate", Chalcogenide Letters, Vol. 8, No. 4, (2011), pp. 239-247.

[15] R. S. Silva, A.F.G. Monte, P. C. Morais, A. M. Alcalde, Fanyao Qu, and N. O. Dantas, "Synthesis and Characterization of PbS Quantum Dots Embedded in Oxide Glass", Vol. 36, No. 2A, (2006), pp. 394-396.

[16] S. V. Kilina, D. S. Kilin, V. V. Prezhdo, and O. V. Prezhdo, “Theoretical Study of Electron–Phonon Relaxation in Pbse and Cdse Quantum Dots: Evidence for Phonon Memory”, The Journal of Physical Chemistry C, Vol. 115, No. 44 (2011), pp. 21641-51.

[17] N. Soltani , E. Gharibshahi, E. Saion, “Band Gap of Cubic and Hexagonal CdS Quantum Dots – Experimental and Theoretical Studies.”, Chalcogenide Letters, Vol. 9, No. 7, (2012), pp. 321-328.

[18] A. J. Nozik, M. C. Beard, J. M. Luther, M. Law, R. J. Ellingson,| and J. C. Johnson, “Semiconductor Quantum Dots and Quantum Dot Arrays and Applications of Multiple Exciton Generation to Third-Generation Photovoltaic Solar Cells”, Chemical Reviews, Vol. 110, (2010), pp. 6873-90.

[19] G. Nootz, L. A. Padilha, L. Levina, V. Sukhovatkin, S. Webster, L. Brzozowski, E. H. Sargent, D. J. Hagan, and E. W. Van Stryland, “Size Dependence of Carrier Dynamics and Carrier Multiplication in Pbs Quantum Dots”, Physical Review B, Vol. 83, No. 15, (2011).

[20] K. Gietka, J. Kobak, J.-G. Rousset, E. Janik, T. Saupinski, P. Kossacki, A. Golnik and W. Pacuski, “MBE Growth of CdTe/ZnTe Quantum Dots with Single Mn Ions.”, Acta Physica Polonica A, Vol. 122, No. 6, (2012), pp.1056.

[21] C. B. Murray, C. Kagan, M. Bawendi, “Synthesis and characterization of monodisperse nanocrystals and close-packed nanocrystal assemblies”. Annual Review of Materials, Science, Vol. 30, No. 1, (2000), pp.545-610.

[22] E. Lifshitz, I. Dag, I. Litvin, G. Hodes, S. Gorer, R. Reisfeld, M. Zelner, and H. Minti, “Optical properties of CdSe nanoparticle films prepared by chemical deposition and sol-gel methods.” Chemical Physics Letters, Vol. 288, No. 2, 1998, pp.188-196.

[23] J. Tang, “Materials Engineering for Stable and Efficient PbS Colloidal Quantum Dot Photovoltaics.” Thesis University of Toronto, (2010).

[24] C. –Y. Huang, D. –Y. Wang, C.-H. Wang, Y. –T. Wang, Y. –T. Jiang, Y. –J. Yang, C. -C. Chen, and Y. –F. Chen, "Efficient Light Harvesting and Carrier Transport in Pbs Quantum Dots/Silicon Nanotips Heterojunctions", Journal of Physics D: Applied Physics, Vol. 44, No. 8, (2011), p.085103.

[25] F. C. Jain, E. Suarez, M. Gogna, F. Alamoody, D. Butkiewicus, R. Hohner, T. Liaskas, S. Karmakar, P. Y. Chan, B. Miller, J. Chandy, and E. Heller, "Novel Quantum Dot Gate FETs and Nonvolatile Memories Using Lattice-Matched Ii–Vi Gate Insulators", Journal of Electronic Materials, Vol. 38, No. 8, (2009), pp. 1574-78.

[26] F. Hetsch, N. Zhao, S. V. Kershaw, and A. L. Rogach, "Quantum Dot Field Effect Transistors", Materials Today, Vol. 16, No. 9, (2013), pp. 312-25.

[27] E. J. Gansen, M. A. Rowe, M. B. Greene, D. Rosenberg, T. E. Harvey, M. Y. Su, R. H. Hadfield, S. W. Nam, and R. P. Mirin, "Photon-Number-Discriminating Detection Using a Quantum-Dot, Optically Gated, Field-Effect Transistor", Nature Photonics, Vol. 1, No. 10, (2007), pp. 585-88.

[28] J. S. Lee, M. V. Kovalenko, J. Huang, D. S. Chung, and D. V. Talapin, "Band-Like Transport, High Electron Mobility and High Photoconductivity in All-Inorganic Nanocrystal Arrays", Nature Nanotechnology, Vol. 6, No. 6, (2011), pp.348-52.

[29] T. –H. Kim, K. –S. Cho, E. K. Lee, S. J. Lee, J. Chae, J. W. Kim, D. H. Kim, J. –Y. Kwon, G. Amaratunga, S. Y. Lee, B. L. Choi, Y. Kuk, J. M. Kim, and K. Kim, "Full-Colour Quantum Dot Displays Fabricated by Transfer Printing", Nature Photonics, Vol. 5, No. 3, (2011), pp. 176-82.

[30] Y. Zhou, M. Eck, C. Veit, B. Zimmermann, F. Rauscher, P. Niyamakom, S. Yilmaz, I. Dumsch, S. Allard, and U. Scherf, "Efficiency Enhancement for Bulk-Heterojunction Hybrid Solar Cells Based on Acid Treated Cdse Quantum Dots and Low Bandgap Polymer Pcpdtbt", Solar Energy Materials and Solar Cells, Vol. 95, No. 4, (2011), pp.1232-37.

[31] S. N. Sharma, T. Vats, N. Dhenadhayalan, P. Ramamurthy, and A. K. Narula, "Ligand-Dependent Transient Absorption Studies of Hybrid Polymer:Cdse Quantum Dot Composites", Solar Energy Materials and Solar Cells, Vol. 100, (2012), pp. 6-15.

[32] Matthew J. Greaney, Saptaparna Das, David H. Webber, Stephen E. Bradforth, and Richard and L. Brutchey, “Improving Open Circuit Potential in Hybrid P3HT:CdSe Bulk Heterojunction Solar Cells via Colloidal tert-Butylthiol Ligand Exchange”, ACS Nano, Vol. 6, No. 5, (2012), pp. 4222-30.

[33] N.J. Pinto, P. D. Shah, P. K. Kahol and B. J. McCormick, “Dielectric constant and ac conductivity in polyaniline derivative”, Solid State Communications, Vol. 97, No. 12, (1996), pp. 1029-31.

[34] C. Querner, P. Reiss, J. Bleuse, and A. Pron, “Chelating Ligands for Nanocrystals’ Surface Functionalization”, Journal of American Chemical Society, Vol. 126, No. 37, pp. 11574-11582.

Chapter 4 QDs-embedded SU8 hybrid for highly sensitive IR phototransistors

1. Introduction

Present chapter is focus on integrating QDs into phototransistors with high performance. With optimization of the QDs/SU8 hybrid insulator, this photo-sensing hybrid insulator can combine high sensitivity with excellent insulation properties. The QDs selected can broaden the detecting wavelength into long rang IR waveband. Moreover, the phototransistor structure can provide quick answer to incident pulsed IR light.

The mechanism of the optical-electric conversion is researched and summarized in this chapter. This novel TFT's integrated process can be transferred to all kinds of CMOS and MOSFET technology and be compatible with the large-scale microelectronic processes.

2. MIS structure device for Optimization of the QDs/Su8 hybrid insulator

In this thesis, QDs/SU8 hybrid composite has to act simultaneously as photo-sensing and insulating layer in this phototransistor. It is the key technology to make sure the enough photo-sensitivity and guarantee the insulating properties. To verify the performance of the QDs/SU8 hybrid, the MIS (metal-oxide-semiconductor) device as shown in figure 4.1 with ZnO: Al/ QDs-SU8/highly N-doped silicon wafer structure was fabricated. With this MIS structure, the performance of QDs/SU8 hybrid insulator can be optimized which provides enough information for the phototransistors' fabrication.

2.1 Review of previous QDs-embedded insulator for MIS structure

In 2011, S. Cosentino, Pei Liu and Son T. Le reported on a QDs-integrated MIS structure device [1]. With a 900℃ high temperature process, the QDs embedded SiO_2

layer can tunnel photo-generated QDs to the semiconductor Si. The disadvantage is of course the too higher 900℃ fabrication temperature which is so difficult to integrate with other optoelectronic devices.

In 2014, C. Y. Chien, W. T. Lai and P. W. Li develop a unique approach for integrate size tunable Ge quantum dots and Silicon Nitride Si_3N_4 insulator for the metal-oxide-semiconductor (MOS) diodes [2].

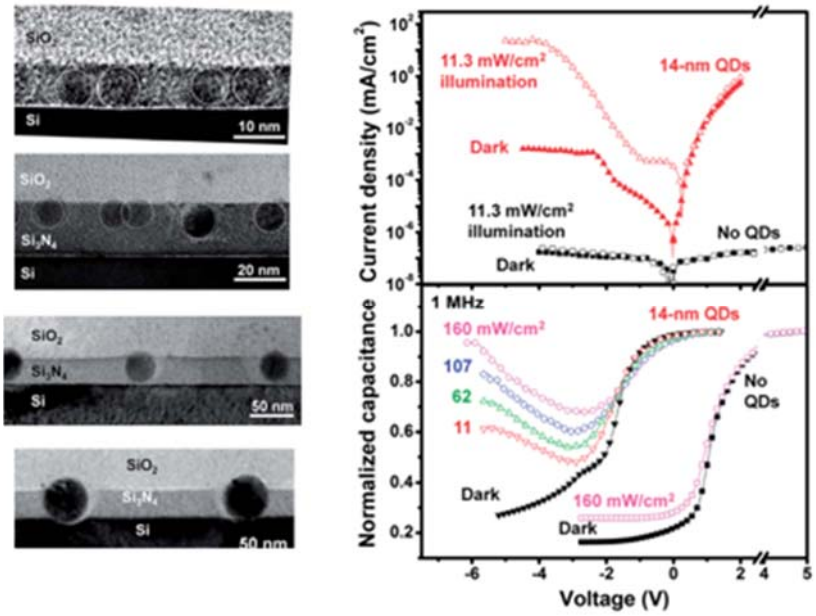

Figure 4.1 TEM image of the QDs-embedded SiN and SiO blended insulator for the MOS device and the J–V and C–V characteristics of the 14 nm Ge-QD MOS diode and the diode containing no Ge QDs in the dark and under 950nm

The experimental demonstration in this work shows a photo-generated current and a capacitance increase under IR light. But this layer-by-layer QDs embedded deposition process is a very complex, expensive and very-high temperature MBE technology. And they didn't create TFT under this MOS device to continue the further research on the QDs-embedded TFT.

Interestingly, no similar letters or papers reported the solution-process photo-sensitive insulator for MIS device or phototransistors, which shows the significant meaning of our research on this technology compatible with all-kinds of other

microelectronics, such as organic, silicon, oxide and novel low-dimension FET structure phototransistors.

2.2 Fabrication and Characterization of the MIS device

2.2.1 fabrication processes for the MIS device

Our QDs-embedded MIS structure followed a very simple fabrication process, it belongs to an organic solution-process. The device is fabricated on the highly N-doped silicon wafers with QDs/SU8 hybrid photo-sensing insulator and transparent AZO (ZnO: Al) electrode on the top for guiding the incident infrared light, as shown in figure 4.2.

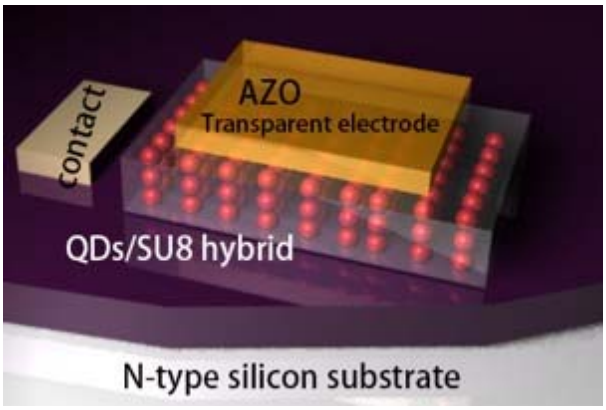

Figure 4.2 the schematic for the MIS structure device

The detailed processes:

1) The wafer is cleaned by acetone and ethanol for around 10 min respectively before any manipulation is carried out on the wafer for the sake of diminishing the impurities on the surface. The wafer is blown out by N_2.

2) The dried wafers go through the RCA cleaning of the N-type silicon. The detailed RCA cleaning process is following the above introduced standard steps to remove metallic and organic impurities by strong base, acid and

oxidant.

3) The dried QDs powder will be rationed by analytical balance and dissolved into as-prepared SU8 insulator solution to produce QDs/SU8 blended solution with different QDs' concentration.

4) The QDs/SU8 blended solution was spin-coated on the prepared wafers. The detailed deposition parameters are 2500rpm for speed; 3000rpm for accelerate; prebake temperature is 95℃ with 90s; UV-exposure time 70s; after-bake temperature is 95℃ with 90s; develop in the base solution for 55s; cross-linked baking stepped temperature is from 95 to 110℃ for 25min.

5) Finally, transparent AZO (ZnO: Al) electrode is deposited on the top by RF sputtering. The target is AZO (99.99%) with 4:1 ratio Ar/O2 hybrid reactive gas and 1 Pa pressure in the chamber. Moreover, the power of the RF source is 150 W and the sputtering time is about 30 min for forming 150nm transparent AZO electrode.

2.2.2 Characterization for the MIS device

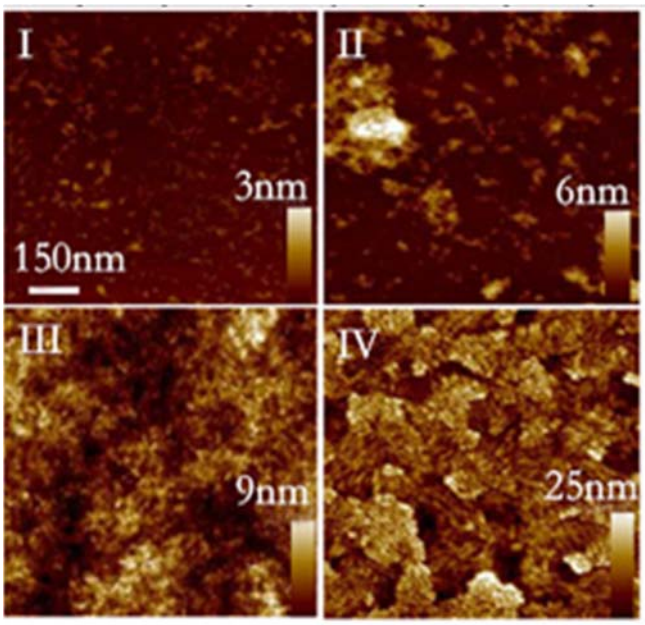

Figure 4.3 Topographic AFM data of pure SU-8 insulator film (i), 0.3mg/mL

(ii), 3mg/mL (iii) and pure PbS QDs (iv).

The top-view morphology of the QDs-based films (pristine SU8 insulator, 0.3mg/ml and 3mg/ml QDs/SU8, pure PbS QDs) can be illustrated in figure 4.3. As can be seen in this figure, higher concentration of QDs in SU8 induces higher surface roughness, but with a better QDs' uniform distribution.

One conclusion is that with increasing of the QD's concentration, the density and uniformity of the QDs will be promoted accompanied with the side effect of surface roughness. It will be boosted tremendously to deteriorate the insulation of the hybrid film. To explore and explain the conductivity and the mechanism of the QDs inside the insulator, the further experiment was carried out to investigate this photo-sensing composite insulator.

2.3 Optical-electrical properties and analysis for the MIS structure device

2.3.1 Optical-electrical properties of the MIS device

The MIS devices with different concentrations of QDs inside the SU8 insulator were characterized by plotting the flowing current I as a function of the applied voltage V. The measurements were done in darkness and under a 0.2 mw/cm^2 near infrared light at a wavelength of 0.85 μm. Figure 4.4 gives the net photocurrent (current under light – current in darkness) as a function of the applied voltage. At low QDs concentration, the photo-generated current is negligible, while it increases at higher QDs concentration. With the closer distance between QDs due to higher concentration, the photo-generated carriers in QDs can tunnel through SU8 so that a flowing current in the MIS device will be measurable.

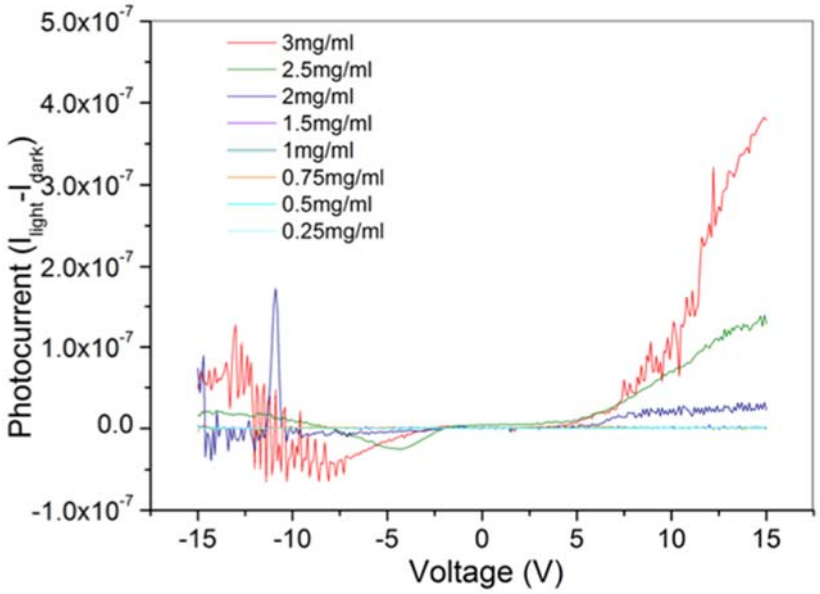

Figure 4.4 Photocurrent verse applied bias dependent on different concentration

2.3.2 Analysis and mechanism of the MIS device

To understand the mechanism of the photo-MIS device, the current in darkness and the photosensitivity of the device under previous near infrared light are plotted in Figure 4.5 as a function of the QDs' concentration inside the hybrid insulator. The photosensitivity is defined as usual by the ratio of the flowing current's increase under light (current under light – current in darkness) to current in darkness.

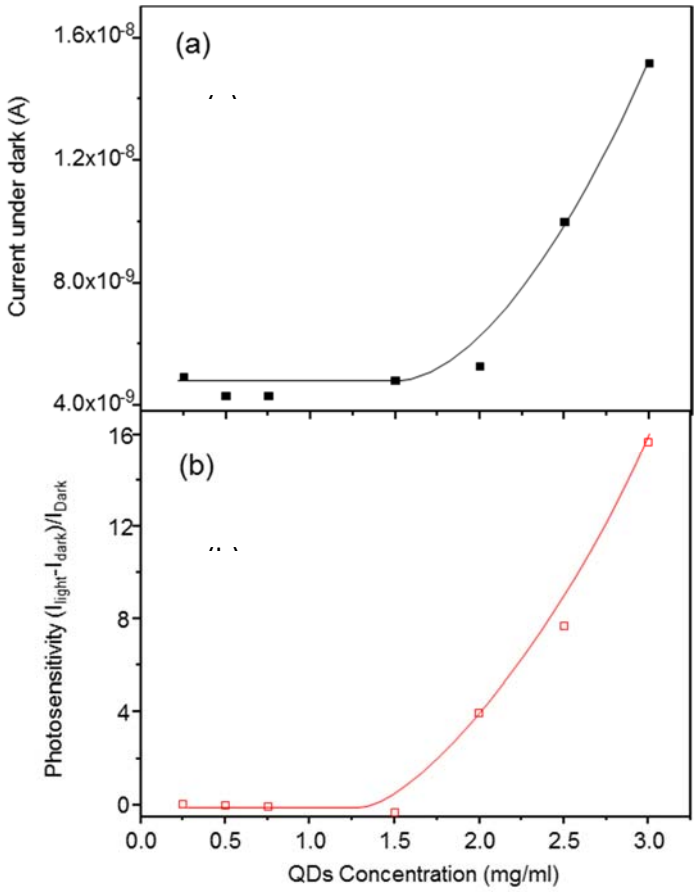

Figure 4.5 The dark current as a function different QDs' concentrations of the MIS structure devices (a), and the photosensitivity curve verse the QDs' concentrations (b).

When increasing the QD's dilution, the dark current stays nearly constant and low still a concentration of 1.5 mg/ml. At higher concentration, it increases highly but stays not so high, reaching 16 nA about at 3 mg/ml as shown in figure 4.5. Under light, the current increases only if the concentration is higher than 1.5 mg/ml. Before this concentration, it stays more or less at the under dark value. The photosensitivity, defined as the ratio of the increase (I_{Light}-I_{Dark}) under I_{Dark}, is nearly 0 before the concentration of 1.5 mg/ml. It increases with the concentration after this limit figure 4.6. To explain the increase of the dark current at higher than 1.5 mg/ml QDs concentration, we can argue on the possibility of tunneling of charge carriers between QDs that are separated by the SU8 insulator. At higher than 1.5 mg/ml QDs concentration, the distance between neighbor QDs becomes enough low leading to an

increase of the tunneling probability [3]. Due to the lower QDs' distance, lower potential barrier and the similar electric distribution, the tunneling possibility will be higher also for high concentration solution.

For the following results, the concentration of QDs was fixed to 2.5 mg/ml to take advantage of the photosensitivity without increasing too much the leakage current inside the insulator. At this concentration, the dark current is 10 nA with 0.1 mm^2 area of the MIS structure. Considering the channel area of the fabricated TFTs which is in the order of 10-50$\times 10^{-4}$ mm^2, the leakage current of the TFTs can be in the order of 100-500 pA.

In conclusion, SU8 insulator with enough concentration of QDs can act as efficient gate insulator of field effect transistors. Present experiment on MIS structure showed that a leakage current can flow in the insulator if the concentration of QDs is not low. However high concentration leads to high leakage current that is not compatible with the use of the mixed film as gate insulator. An optimum of 2.5 mg/ml QDs inside SU8 leading to a leakage current of 10-50 $\mu A/cm^2$ was determined as the best way to reach gate insulator quality.

The other conclusion is the possibility for photocarriers, generated by the light inside QDs, which can flow from QD to its neighbor and reach the electrode of the MIS structure. This possibility was shown to occur if the concentration of QDs is enough high to decrease the distance between QDs occurring in tunneling. The flow of the photocarriers can induce a carrier injection inside the channel of a field effect transistor and then a sensitivity to the light of the transistor.

3. Phototransistor using QDs/SU8 hybrid insulator

Previous conclusion leads us to fabricate field effect transistor using the mixed QDs-SU8 film as gate insulator in view to check their photosensitivity. Starting from

the large experience of IETR in silicon and organic Thin Film Transistors on any substrate, we use the well-known and well-established polysilicon TFT technology on glass to demonstrate the feasibility of making phototransistors. However, any other TFT technology will lead to similar results.

3.1 Fabrication processes for the QDs-embedded phototransistor

QDs-SU8 mixed solution was spin-coated at 2500rpm during 30s, then soft-baked at 95°C during 90s, exposed during 70s to UV light and finally baked at 95°C during 90s. This QDs-SU8 film is used as gate insulator of conventional LTPS top-gate TFT's structure. The fabrication follows the well-known and well-established TFT's process in the Lab, in the purpose to check precisely the change occurring when replacing the usual silicon dioxide gate insulator by present QDs-SU8 film.

The 4-masks process starts with the deposition of a stack of undoped and heavily phosphorous or boron doped amorphous silicon layers by LPCVD at 550°C. Then both layers are annealed at 600°C under vacuum during 8 hours in the same deposition reactor. Well-crystallized polycrystalline silicon material is obtained after this step [4].

The first photolithography step consists in SF6 plasma etching the top doped-layer to define the drain and source regions. The type of TFT is defined by the doping of these regions, N-type TFT with phosphorus doped layer and P-type TFT for boron doped layer.

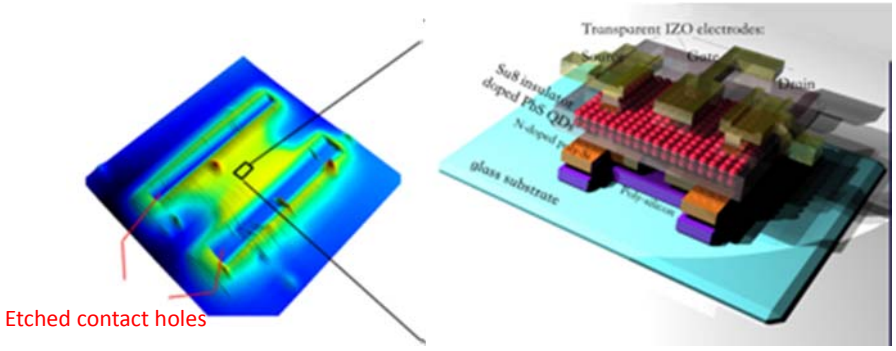

Figure 4.6 The 3D-profile picture of the Su8/QDs' blended insulator and the device schematic,.

In the second lithography step, TFTs are insulated from their neighbor by SF6 plasma etching the undoped layer.

Then, a radio corporation of America (RCA) cleaning is performed to remove ionic, organic impurities and reduce the roughness of the silicon surface. This important step is followed immediately by the deposition of photo-sensing insulator by the above-mentioned spin-coating process. This film will act simultaneously as photo-sensor and gate insulator. It is etched by RIE (the height morphology of the QDs functioned SU8 can be seen in figure 4.6) and the insulator was etched by RIE and third lithography process to contact the source/drain electrode. Moreover, 150nm Al doped Zinc oxide (ZnO:Al) transparent electrode was deposited by RF sputtering (using 4:1 ratio Ar/O2 gas, 1 Pa pressure, 100 W RF power and 30 min sputtering time). Finally, fourth photolithography was used to form the drain, source and gate electrodes which can be shown in figure 4.7.

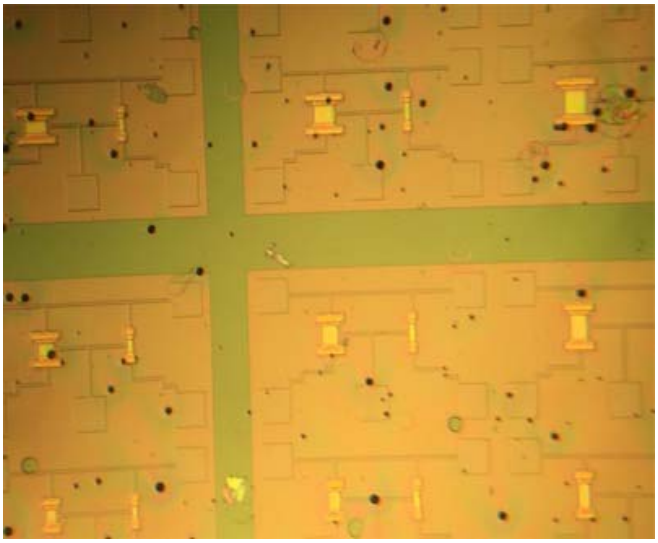

Figure 4.7 The microscope photograph of the device

3.2 Transfer characteristic of TFTs using QDs/SU8 insulators

TFTs using 2.5 mg/ml QDs diluted in SU8 as gate insulator were fabricated and characterized in dark and under different wavelengths light. Transfer characteristics,

channel current (between drain and source) as a function of the gate voltage, are shown in figure 4.8 of both N-type and P-type TFTs with same channel size, (40μm large and 20μm long) in dark and under different wavelengths lights. Obviously these TFTs are affected by the light. As expected form the absorbance behavior of the QDs-SU8 film, the variation of the current decreases when shifting to far IR.

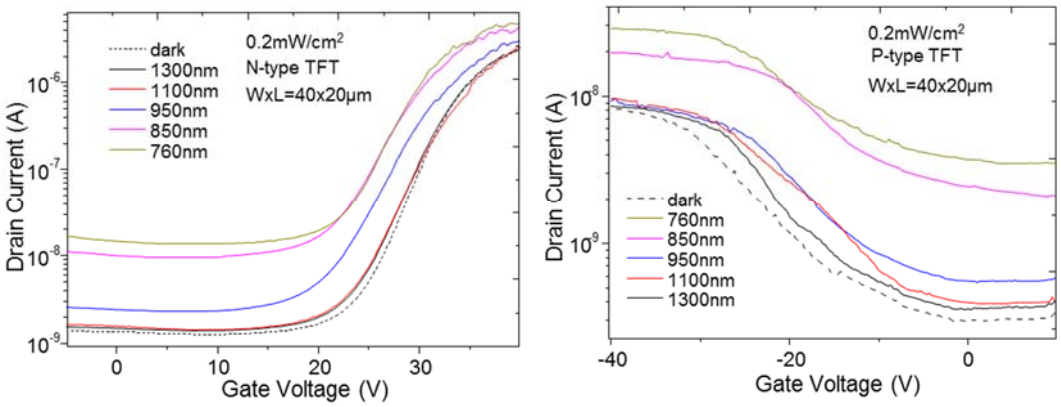

Figure 4.8 Transfer characteristics of N-type (a) and P-type (b) TFTs with the same channel length L=20μm and same channel width W=40μm under dark and under same power 0.2 mW/cm^2 and different IR wavelength light.

As shown in the figure 4.8, we present the electrical parameters for these two device here. Transfer characteristic of N-type TFT has a well on/off ratio (10^4), the mobility of this N-type TFT is 1.3 cm^2/Vs, sub-threshold slop is 1.4V/Dec with a low 1 nA reverse current and 0.1 nA leakage current. Compared with the N-type TFT, P-type TFT's electrical properties deteriorate for the mobility (0.37 cm^2/Vs) and the on/off ratio (10^2). Perhaps the better electrical characters of N-type TFT can lead to a better performance for the response toward the incident IR light.

As a consequence of these TFT's characteristics, further experiments were carried out to exhibit the optical-electrical performance, the conversion mechanism for the photo-generated current output and intrinsic amplifying mode for the FET structure photodetector.

4. optical-electrical performance and mechanism for the

phototransistor

The optical-electrical performance of the phototransistors should be measured and calculated to characterize the phototransistor. Especially, the stead-state optical-electrical responsivity, photo-sensitivity and power-dependent function were tested in this section for the photo-detector application.

4.1 optical-electrical performance of the phototransistor

4.1.1 Responsivity measurements and analysis for phototransistor

The responsivity of both types of TFTs is shown in figure 4.9 as a function of the gate voltage. For the N-type TFT, the responsivity increases sharply with the increase of the gate voltage and reaches saturated station after 35V. But in the responsivity curve of P-type TFT, the responsivity increases markedly with the decrease of the gate voltage and reach saturation below -25V. Thus, we can conclude that both N-type and P-type TFTs have a decade higher current in on-state regime of the TFT.

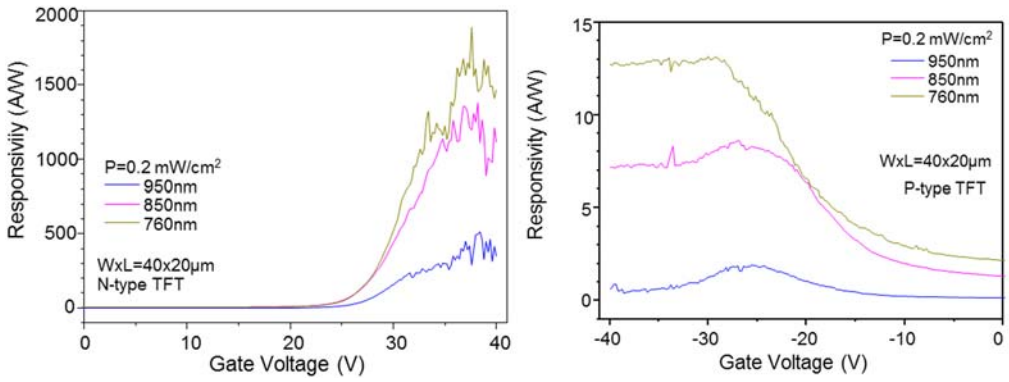

Figure 4.9 Responsitivity at near-IR 760nm, 850nm, and 950nm wavelengths of N-type TFT (c), and of P-type TFT (d)

Meanwhile, the responsivity is higher for N-type TFT than for P-type one because of a better mobility and on-state current proved above.

Remarkably, higher current was also obtained for N-type TFT reaching 1800 A/W at 760 nm. More important is the not negligible responsivity at 1.3 μm that reaches

13 A/W as depicted in figure 4.10 which implies the possibility for the application in telecommunication. Moreover, the responsivity also shows the decrease of N-type TFT responsivity when increasing the wavelength in correspondence with the QD's absorption.

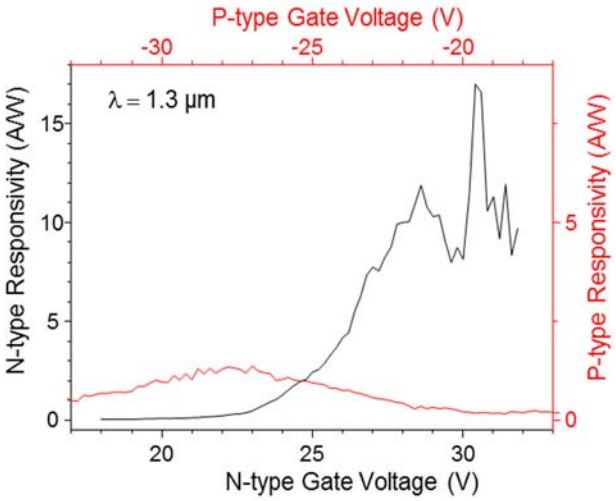

Figure 4.10 Their responsivity at long-wavelength IR waveband.

4.1.2 Photosensitivity measurements and analysis of phototransistor

The information on the responsivity is indicative on the usefulness of the device as sensor. However, it depends highly on the dark direct current and then on the field effect mobility of the transistor. Here, the process can be highly improved to increase this mobility. While the most important is the photosensitivity of the device that gives a direct information on the usefulness of the detection principle of the present device. The photosensitivity is the photocurrent gain which is the current increasing value under light in proportion of the dark current. It is given by $(I_{Light}-I_{Dark})/I_{Dark}$. The photosensitivity of previous N-type and P-type TFTs as a function of the gate voltage is shown in the following figures.

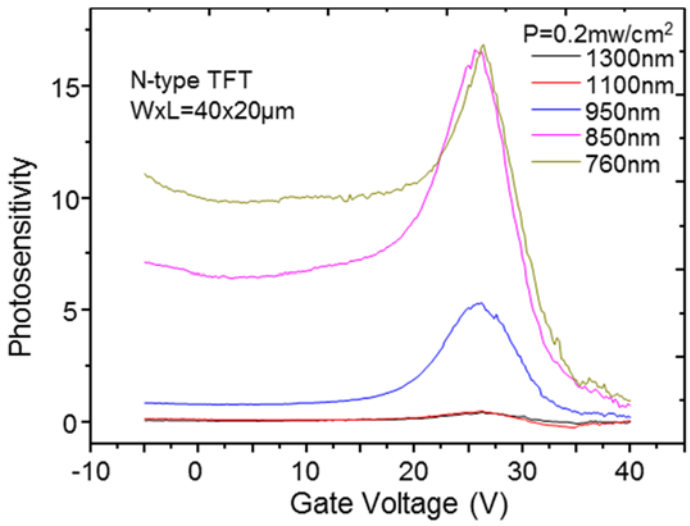

Figure 4.11 Photosensitivity (I_{Light}-I_{Dark})/I_{Dark}) of N-type to 0.2 mW/cm^2 power light at different IR wavelength.

Figure 4.11 shows the photosensitivity of N-type under the different IR wavelength with the same 0.2 mW/cm^2 incident light power verse the gate voltage.

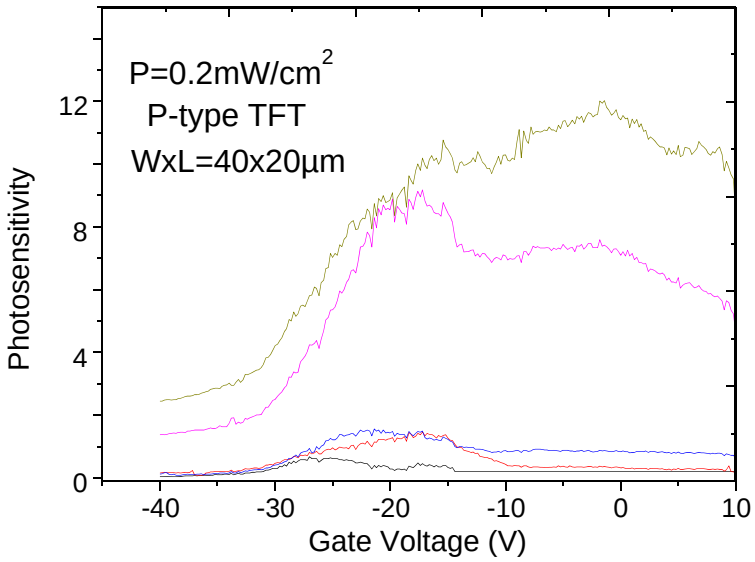

Figure 4.12 Photosensitivity (I_{Light}-I_{Dark})/I_{Dark}) of P-type to 0.2 mW/cm^2 power light at different wavelengths

Figure 4.12 shows the photosensitivity of P-type TFT under different IR wavelengths with the same 0.2 mW/cm^2 incident light power versus the gate voltage.

Remarkably the photosensitivity ranges in the same order for both types of TFTs even if it is slightly higher for N-type TFT. It is important here to remember the more

than 100 ratio between the responsivity of N-type and P-type TFTs. The similar photosensitivity demonstrates clearly that the same phenomenon is responsible for the sensitivity of the present device to the light. It accounts for the same QDs/SU8 photosensing gate insulator of both TFTs, but not the poly-silicon active layer with different electrical performances.

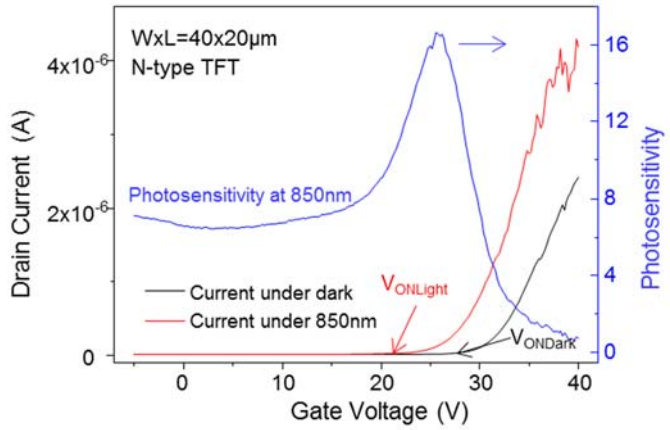

Figure 4.13 (a) Photosensitivity of N-type TFT at 850 nm showing the decrease of the threshold voltage under light and the peak of photosensitivity.

The photosensitivity of N-type TFT was tested at 850nm and the corresponding transfer characteristic curve under dark and 850nm illumination were plotted also in figure 4.13. The threshold voltage shifts towards lower values under light. This negative shift can be explained by the accumulation of the negative carriers inside active layer thanks to the positive carriers' trapping within hybrid insulator/channel's interface driven by positive gate voltage.

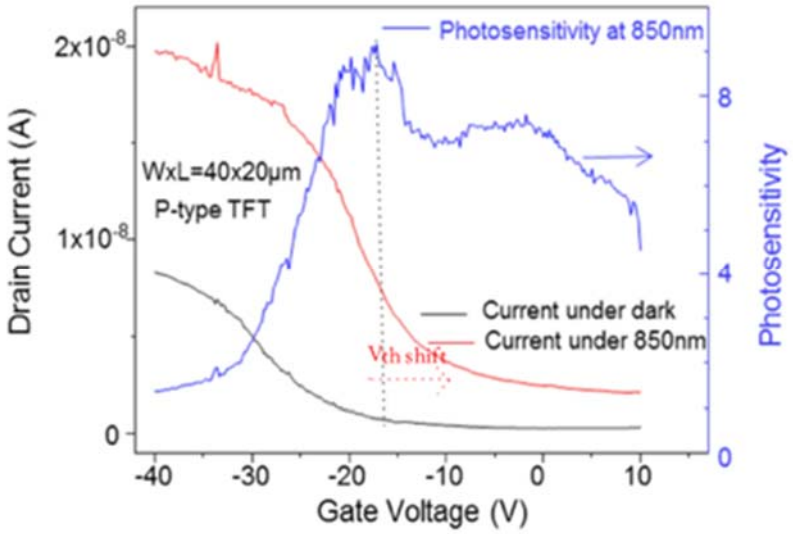

Figure 4.14 (a) Photosensitivity of P-type TFT at 850 nm showing the decrease of the threshold voltage under light and the peak of photosensitivity.

The photosensitivity of P-type TFT was tested at 850nm and the corresponding p-TFT's transfer characteristic curve under dark and 850nm illumination were plotted also in figure 4.14. The threshold voltage shifts towards less negative values under light. This positive shift can be explained by the accumulation of positive carriers thanks to the negative carrier's trapping within insulator/channel's interface driven by the negative gate voltage.

Synthesizing the results of both N-type and P-type TFTs' threshold voltage shift experiment, the photosensitivity peaks at medium gate voltage. To understand the origin of the peak, it is possible to involve the shift of the threshold voltage V_{TH} under light. Indeed, V_{TH} shifts towards lower values for both N-type and P-type TFTs under light. It peaks between $V_{ONunder\ light}$ and V_{ONDark} ($V_{ONunder\ light}$ and V_{ONDark} are the gate voltage from which the current starts to increase under light and under dark respectively). In this range of gate voltage, the photocurrent starts to increase when the dark current stays very low. After higher gate voltage than V_{ONDark}, both photo- and dark- currents increase and the photosensitivity decreases.

4.1.3 Power-dependent responsivity and analysis for phototransistor

After trying to exhibit the responsivity and photosensitivity, it is the time to check the behavior of the responsivity as a function of the light power, or the sensitivity of the sensor. Figure 4.15 plots the the transfer characteristic curves under 0.95 μm IR light dependent under different incident light powers under drain-source voltage V_{DS}=5V.

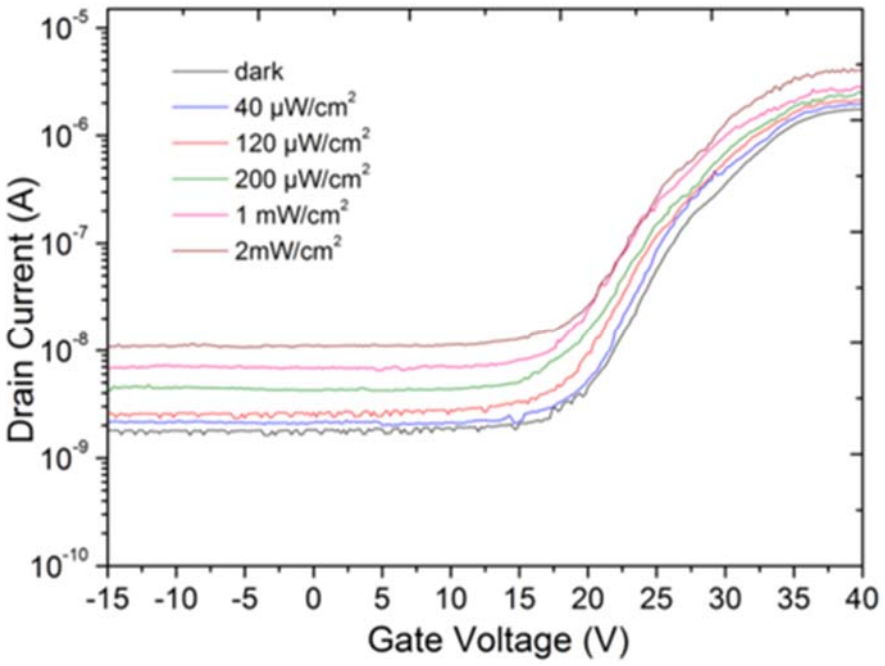

Figure 4.15 Transfer characteristic curves under 0.95 μm IR light at different incident light powers.

As shown in this figure 4.15, the drain current increases gradually with the increase of the incident IR light's power. To better analyze and explain the power-dependent behavior, the typical drain current was extracted to calculate the responsivity and plotted log-log curves versus the power intensity.

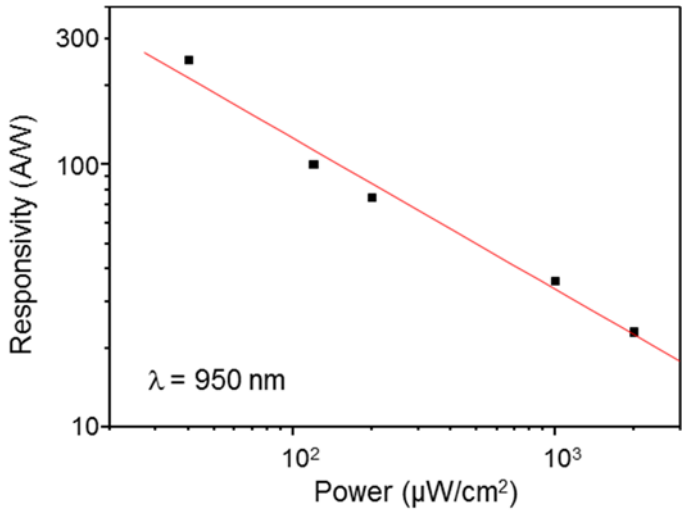

Figure 4.16 Log-Log plot of the behavior of the responsivity as a function of the light power at the wavelength of 950 nm.

Figure 4.16 presents the variation of the responsivity as a function of the light power for 950 nm IR wavelength in a logarithm/logarithm plot. As usual, the curve can be fitted by a power law:

$$\text{Responsivity} = 1.8\text{x}10^{3}\ P^{-0.58} \qquad (2)$$

where the responsivity is given in A/W and the light power P in μA/cm^2. As the responsivity is the ratio between the increase of the current under light and the light power, the relation between the variation of the current that is the photocurrent I_{PH} and the light power P is given by :

$$I_{PH} = \alpha\ P^{1-0.58} = \alpha\ P^{0.4} \qquad (3)$$

Such power law was previously found [5, 6], particularly for graphene-PbS QDs systems. However, the power values they found were so different for the same system and from the present value. The exact significance of this power is really unknown still now. So that we can only assume the present power value, 0.42, is representative of the total probability to convert a photon into electron-hole pair, to separate it under the effect of the gate voltage and finally to inject it into the channel through tunneling effect.

4.2 optical-electrical mechanism inside the phototransistor

For further researching, we proposed two hypotheses for explaining the photo-generated current in the QDs-embedded phototransistors. One is the electron-injection from the QDs/SU8 hybrid insulator, another is the electron carrier's trap within the insulator/active layer's interface leading to a change in capacitance. Consequently, some experiments were performed to explore the intrinsic photocurrent's generation mechanisms inside this phototransistor.

4.2.1 Device energy band and carrier's injection theory for the phototransistor

The energy band diagram of the device shows such possibility of tunneling between QDs and silicon channel (Figure 4.17). In corresponding with this tunneling transfer theory, previous experiment on the MIS structure has also demonstrated the similar device mechanism where the low distance between QDs at high concentration QDs/SU8 hybrid insulator will facilitate the charge tunneling from one QD to the neighbor.

For 5nm diameter PbS QDs, the minimum of their conduction band (CB) was found to be at -4.30 eV and the maximum of the valence band (VB) to be at -5.20 eV [9, 10]. As usual, the minimum of the CB is taken at -4.05eV and the maximum of the VB at -5.17 eV for crystalline silicon. Similarly, the maximum of the CB was taken at -4.35 eV and the maximum of VB at -7.72 eV for ZnO [11]. The values for ZnO are subjected to caution as they depend on the oxygen content and the preparation method. They can change by some 0.1 eV.

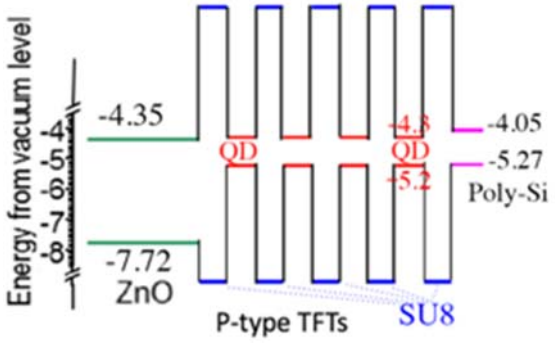

Figure 4.17 Energy band alignment for the phototransistor

Considering the minute minimum CB value's difference between QDs and poly silicon, electrons (resp. holes) can easily tunnel from conduction band (resp. valence band) of QD to conduction band (resp. valence band) of silicon under the application of gate voltage.

If Injection of charge carriers from QDs to the channel is the physical phenomenon leading to the long wavelength sensitivity of the TFTs with QDs-SU8 mixed layer, the leakage gate current has to be similar to the photocurrent or the increase of drain current.

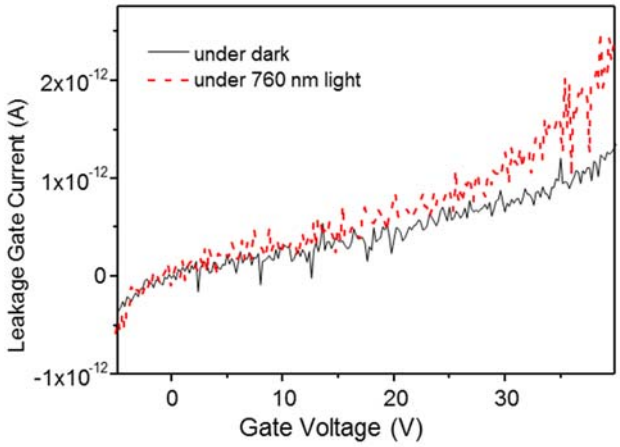

Figure 4.18 Gate leakage current of N-type with L=20µm channel length and W=40µm channel width under dark and under 760 nm wavelength and 0.2 mW/cm^2 power light.

However, figure 4.18 presents the leakage gate current of the N-type TFTs under dark and under 760 nm light in the purpose to highlight its very weak value even if it increases slightly under light. The gate leakage current is 4 orders lower compared with the photocurrent. From this experiment, the contribution of the leakage current or direct current injection can be excluded from the main reason to arise drain current's increase. It seems that there is a disobedient between energy level's theory analysis and practical experiment. So essentially, the carrier's trapping theory was proposed to better describe the photocurrent generation mechanism.

4.2.2 The device physics for the carrier's trapping mechanism within the insulator/active layer's interface

The possibility for electrons and holes to move inside the insulator under the gate field means the possibility of carrier transport inside the insulator. This transport can be insured by tunneling of carriers from one QD to its neighbor as deduced from last section and also prior to the MIS structure's experiment. Since the direct carriers' injection has considered as minutiae for drain-source current's increase under light's exposure, the following carrier's trapping case was used to explain this photosensitivity phenomenon.

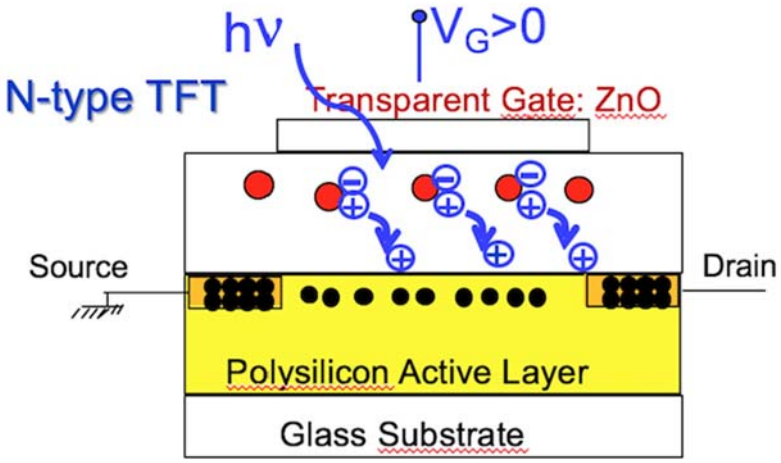

Figure 4.19 Schematic explaining the photosensitivity of present N-type phototransistor.

The appearance of fixed charge inside the insulator under light is evidenced from the decrease of the threshold voltage for both N-type and P-type TFTs under light. For N-type TFTs, photogenerated holes move towards the channel under the positive gate voltage as shown in figure 4.19, where TFT works. This fixed positive charge allows electron accumulation in the channel under lower gate voltage and then leads to a decrease of the threshold voltage of N-type TFTs.

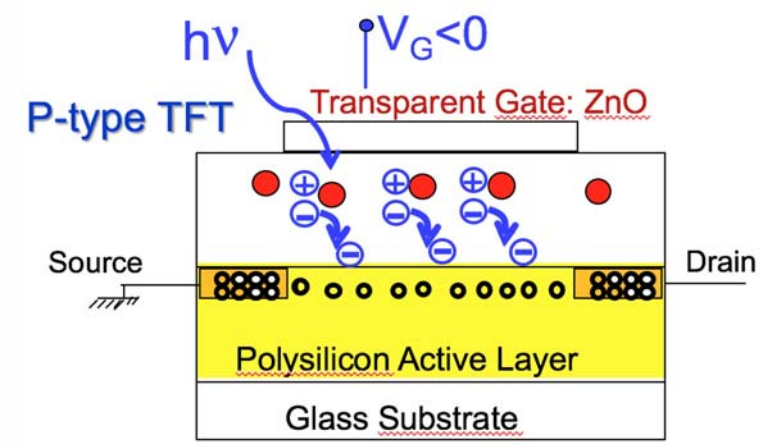

Figure 4.20 Schematic explaining the photosensitivity of present P-type phototransistor.

For P-type TFTs, photogenerated electrons move towards the channel under the negative gate voltage as shown in figure 4.20. This fixed negative charge allows hole accumulation in the channel of P-type under lower gate voltage and then brings about a decrease of the threshold voltage of P-type TFTs.

In consequence, the carrier's distance to the channel will seriously influence this trapping mechanism. To check the effect of the distance fixed charge inside the insulator and the variation of the current, N-type TFTs with very thin SU8 film between the channel and the mixed QDs-SU8 insulator were fabricated for separating photosensing insulator and active layer.

4.2.3 Optical-electrical properties of phototransistor with electron-injection block layer

4.2.3.1 Optical-electrical properties of phototransistor with 150nm SU8

To further research this problem, we deposit a sandwich of two insulator layers as gate insulator (figure 4.21). The first one, directly deposited on the channel surface, is an SU8 layer without QDs. The detailed process of this deposition is 5000rpm spin-speed, 5000rpm accelerate and 30s duration for the formation of this 150nm SU8

pristine insulator The second, deposited on this first layer, is the normal QDs/SU8 insulator for photo-sensing function.

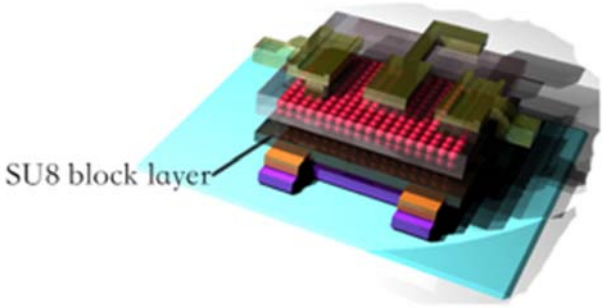

Figure 4.21 The device schematic of the QDs-embedded transistor with SU8 electron-injection block layer

Figure 4.22 shows the transfer characteristics of the described phototransistor with 150nm SU8 insulator between QDs/SU8 hybrid and active Si layer which is illuminated under 580nm incident light's illumination. Through this experiment, this phototransistor with a photo-sensitive behavior was investigated under the visible 580nm yellow light. The photosensitivity is about 0.6.

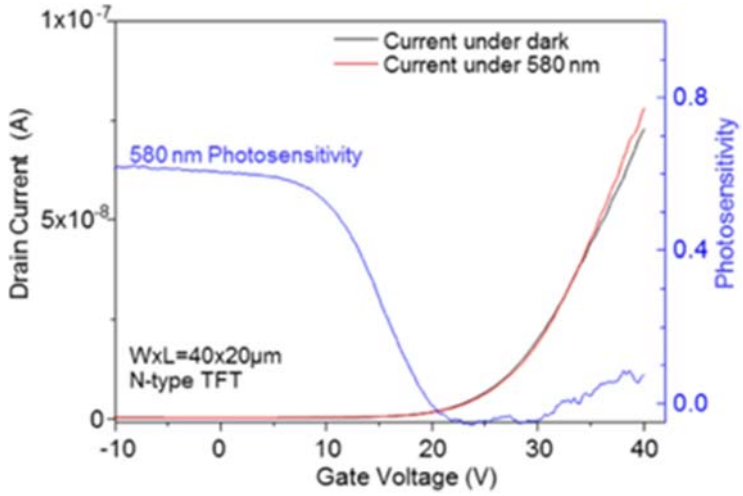

Figure 4.22 Transfer characteristics under dark and under lighting at 580 nm of TFTs with double (SU8 only (a) + mixed QDs-SU8 (b)) gate insulator layer, and their photosensitivity.

Contrary to previous normal QDs-embedded phototranistor, no noticeable change in the threshold voltage between these characteristics can be detected. Low

photosensitivity under visible light (580nm) is measured. The low sensitivity under visible light is due to the intrinsic absorption by silicon active layer of the TFT. Absorption coefficient of crystalline silicon is known to be $7x10^3$ cm^{-1} at 580nm. With this value, less than 20% of the light is absorbed in 300 nm thick silicon active layer [7, 8]. In off-regime of N-type TFTs (negative gate voltage), the off-current is limited by the conduction of the total active layer. Under light, the off-current is highlighted by the absorption of the active layer. However due to the weak absorption, the photosensitivity stays very low. To explore the phototransistor's behavior in IR wavelength range, the device is also measured under the 850nm and 950nm.

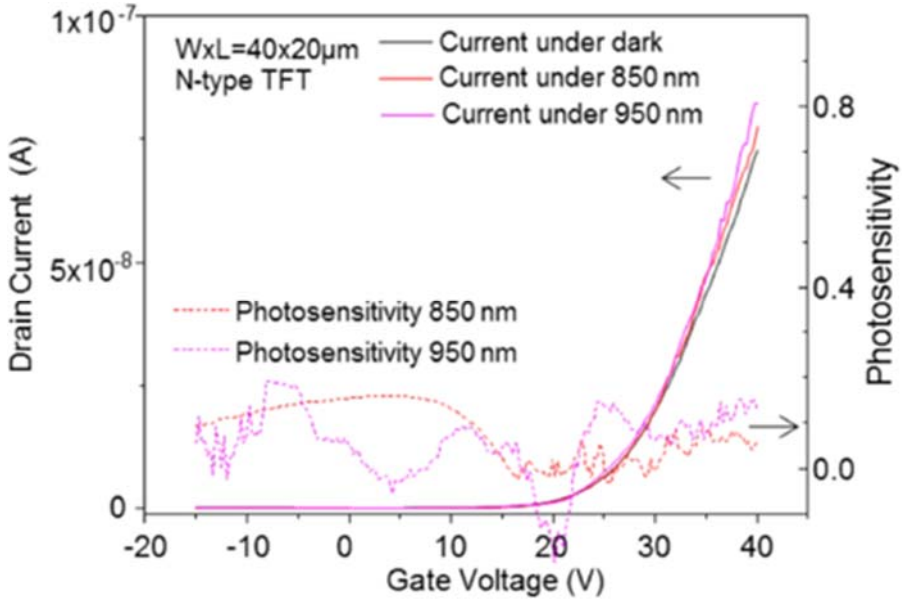

Figure 4.23 Transfer characteristics under dark and under lighting at 850 nm and 950 nm of TFTs with double (SU8 only + mixed QDs-SU8) gate insulator layer, and their photosensitivity.

At longer wavelength (850nm and 950 nm), the absorption by silicon is much lower without inducing photosensitivity, as illustrated in figure 4.23. The more important discovery is the loss of the photosensitivity at these long-wavelengths IR regimes of the present TFTs in comparison of previous ones. Then even if the QDs-SU8 mixed layer still absorb light, TFTs are not sensitive to the light. This result clearly demonstrates that any fixed charge that can be created inside the gate insulator but far

from the channel is not responsible for the sensitivity of TFTs sensitive to long wavelength light.

4.2.3.2 Optical-electrical properties of phototransistor with 15nm SiO_2

In another similar process, we use 15 nm thick SiO_2 as first insulator layer between the channel and the mixed SU8-QDs insulator (figure 4.24) to confirm the carrier's trapping mechanism and the influence of the distance to the channel.

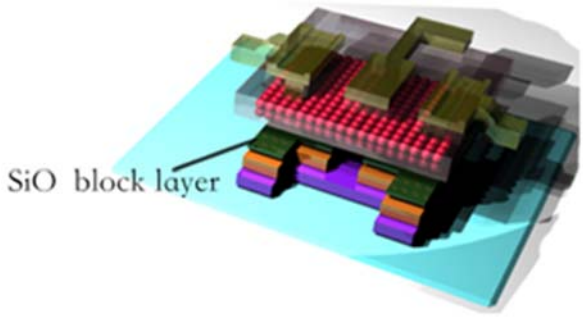

Figure 4.24 The device schematic of the QDs-embedded transistor with SiO_2 electron-injection block layer

This very thin SiO2 layer was deposited by RIE plasma process. Oxygen O_2 gas is used as the plasma gas. The gas flow is 30 sccm, pressure is 10 mTorr, power is 60W and plasma reaction time is 10min.

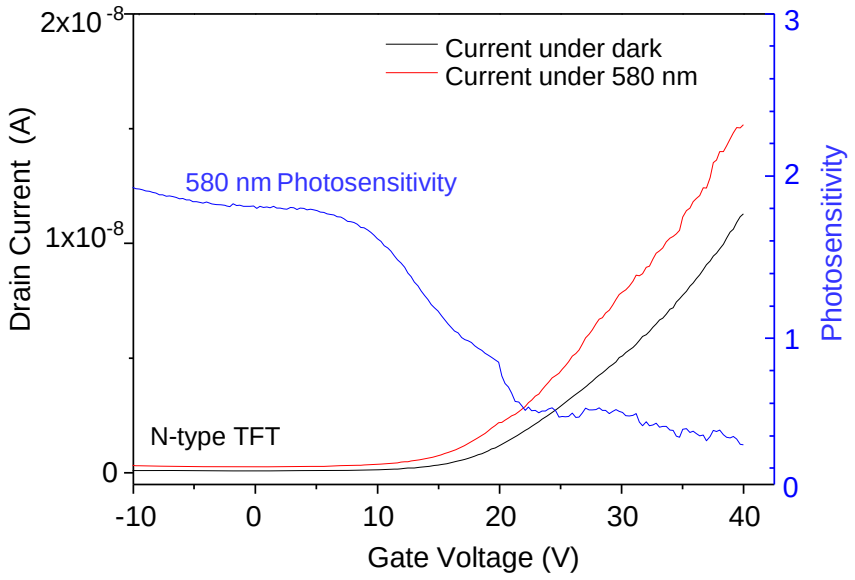

Figure 4.25 Transfer characteristics under dark and under lighting at 580 nm of TFTs with double (SiO_2+ mixed QDs-SU8) gate insulator layer, and their photosensitivity.

Contrary to previous TFTs without barrier film, no noticeable change in the threshold voltage between these characteristics can be detected as illustrated in figure 4.25. Low photosensitivity under visible light (580nm) is measured also. As explained for previous TFTs with 150nm thick SU8 barrier, the low sensitivity under visible light is due to the intrinsic absorption by silicon active layer of the TFT.

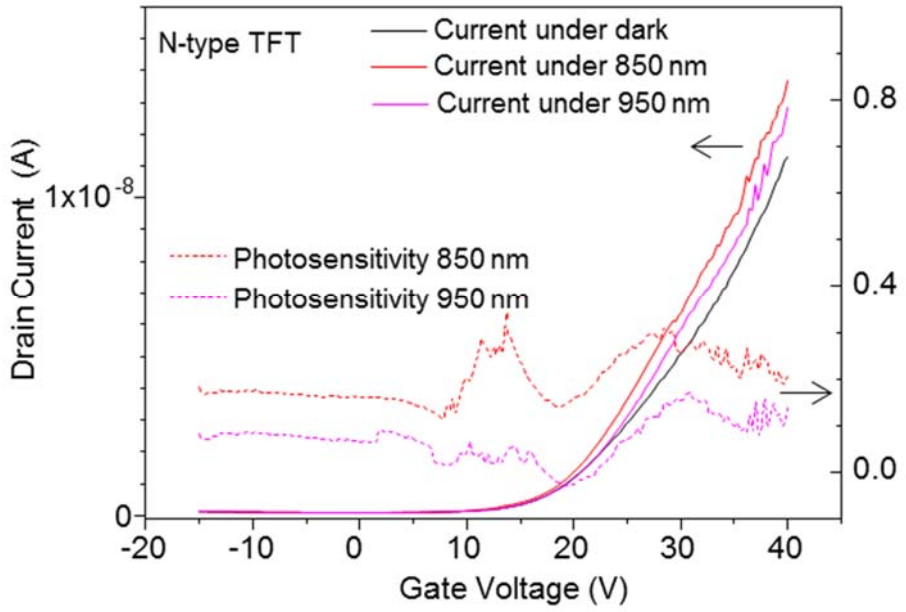

Figure 4.26 Transfer characteristics under dark and under lighting at 850 nm and 950 nm of TFTs with double (SiO_2 + mixed QDs-SU8) gate insulator layer, and their photosensitivity.

At longer wavelength (850nm and 950 nm), the absorption by silicon is much lower inducing no photosensitivity (figure 4.26). The more important observation is the loss of the photosensitivity at long wavelength of the present TFTs in comparison of TFTs without barrier film. This result clearly supports previous result obtained by using 150nm thick SU8 barrier.

Then any insulating layer between the channel and the mixed QDs-SU8 film, even 150 nm thick SU8 or 15 nm thick SiO_2, removes the photosensitivity at near infrared

wavelength. This means that the photosensitivity is not due to a direct carrier's injection from the photosensing gate insulator but really a charge accumulation from the photo-carrier's trapping (close to the interface). Furthermore, the bad interface between SU8 and Si active layer can facilitate this trapping process and lead to a shift of the threshold voltage and then to the increase of the current under light.

4.3 Dynamic optical-electrical performance of phototransistor

At this step of thesis, we can claim that we developed here new phototransistor able to detect and to quantify a light from the visible wavelength to near-IR still 1.3 μm with high responsivity from 1800 A/W at 760 nm to 13 A/W at 1.3 μm. Its fabrication is very easy using only any technique in solution (spin-coating, printing,…) to deposit the sensing layer. It is fully compatible with any usual microelectronic technology, MOSFET technology, large area electronics technology and new flexible electronics. The deposition of the sensing layer is made after all the steps of the fabrication of a device (MOSFET or TFT based device).

4.3.1 Answer of phototransistor under pulsed incident light signal

The other important parameter, which is useful to check, is the response time of the present photosensor under pulsed light. The photo-detector especially in the infrared waveband is widely used in the fiber telecommunication system, real-time scanning signal process and some other high speed signal diagnosis applications [12-14]. As a consequence, the rapid-speed response to the incident photo-modulating signal is an essential capability for photodetector to diminish the signal distortion and symbol error rate (SER). With comparison of the on/off incident modulated light signal and the significant current increase/decrease in the drain-source channel, the photocurrent shows a more serious signal noise interference though has a better photo-responsivity. The answer of N-type and P-type photo-TFTs to pulsed light is presented in figure 4.27 (a) and (b). The power of the light was 0.2 mW/cm^2 and its wavelength fixed to 850

nm.

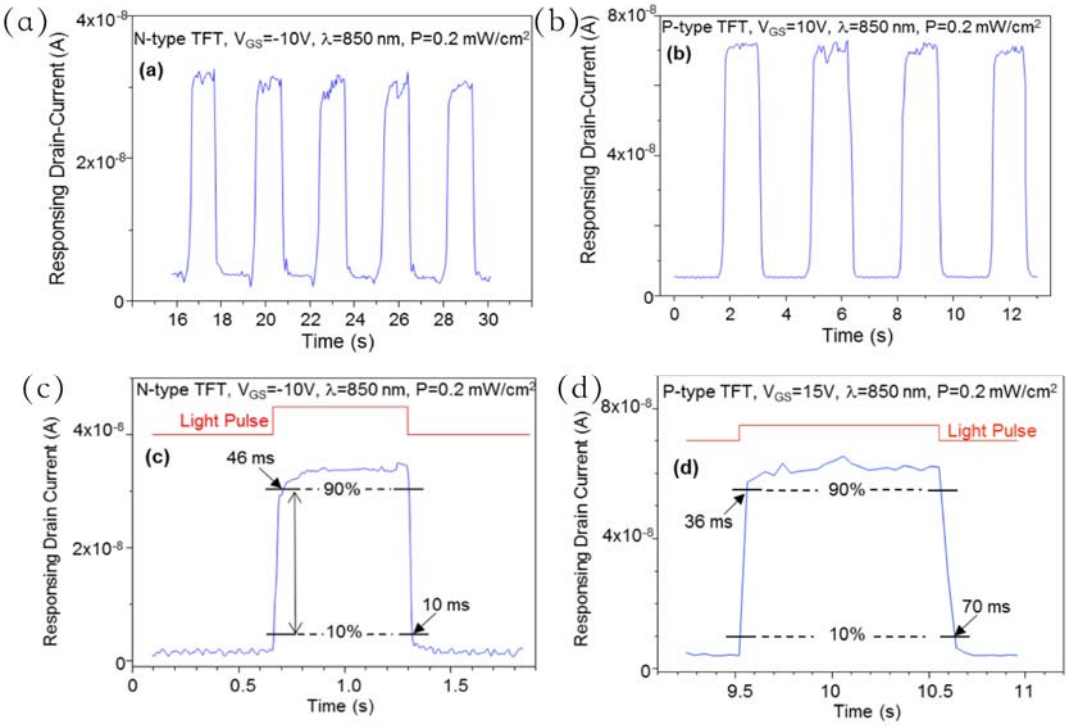

Figure 4.27 Answer of N-type (a) and P-type (b) TFTs to 1.5 s period light pulse. The answer to one pulse is given in (c) for N-type TFT and in (d) for P-type TFT. The rise time is 46 ms for N-type and 36 ms for P-type. The fall time 10 ms for N-type and 70 ms for P-type. These times are calculated as usual from 10% to 90% of the maximum value.

The answer time of these TFTs can be checked trough figure 4.26 c and d where the response to one pulse only is presented. The rise time, as usually defined by the time between 10% and 90% of the maximum value, is 46 ms only (it is 33 ms if defined by the time to reach 80% from 0%) for N-type TFTs and 36 ms for P-type ones. The fall time is much lower, 10 ms, for N-type TFTs and 70 ms for P-type ones. The very quick response can be compared to the values given for PbS QDs based graphene devices [8] where the same 80% to reach the maximum defined rise time was 260 ms and the fall time much higher.

The answer time of average 50 ms will lead to conclude that present photo-TFTs

can answer to less than 1 s pulse and then to a frequency higher than 1 Hz.

4.3.2 Phototransistor's detectivity performance

The other important figure of merit of a photodetector is the detectivity. It is useful to calculate the detectivity of the present devices for comparison with the literature. The detectivity D* is the ability of the sensor to detect a weak signal. It characterizes the sensor in comparison of its noise. The detectivity is given before by:

$$D^* = \frac{A^{1/2}R}{(2\,e\,I_{Dark})^{1/2}} \quad (cmHz^{1/2}W^{-1}, Jones)$$

where e is the elementary charge, A is the active area, I_{Dark} is the dark current and R is the responsivity. The calculated detectivity values at 850 nm are summarized in Table I for both N-type and P-type TFTs in off-regime and in on-regime.

Table 1: Responsivity and Detectivity of N-type and P-type TFTs in off and on regimes to 850 nm wavelength and 0.2 mW/cm^2 power light. The active area for both TFTs is 800 μm^2.

	Regime	Dark Current	Responsivity	Detectivity
N-type TFT	Off (-15V)	500 pA	5.3 A/W	1.2×10^{12} Jones
	On (+33V)	400 nA	1250 A/W	1.0×10^{13} Jones
P-type TFT	Off (+15V)	200 pA	1.5 A/W	5.3×10^{11} Jones
	On (-25V)	3 nA	7.5 A/W	6.8×10^{11} Jones

As shown in table 1, the detectivity of the N-type TFT device is as high as 1×10^{13} Jones. This high specific detectivity can resolve the low light intensity. The detectivity of N-type TFTs is at the level of highest detectivity values already published [15-18]. However, the response time is much lower for the present devices.

5. Conclusion

In summary, we had developed an easy method to fabricate broadband, in the range of visible-NIR, photo-transistor. The fabrication is compatible with all the present microelectronics technologies and with new flexible electronics technology. It can be directly implemented in any process without too much change. High photoresponsivity with fast response time were demonstrated.

6. Reference

[1] S. Cosentino, Pei Liu, Son T. Le, S. Lee, D. Paine, A. Zaslavsky, D. Pacifici, S. Mirabella, M. Miritello, I. Crupi, and A. Terrasi, "High-Efficiency Silicon-Compatible Photodetectors Based on Ge Quantum Dots", Applied Physics Letters, Vol. 98, No. 22, (2011), p. 221107.

[2] C. Y. Chien, W. T. Lai, Y. J. Chang, C. C. Wang, M. H. Kuo, and P. W. Li, "Size Tunable Ge Quantum Dots for Near-Ultraviolet to Near-Infrared Photosensing with High Figures of Merit", Nanoscale, Vol. 6, No. 10, (2014), pp. 5303-8.

[3] H. Zhao, Z. Fan, H. Liang, G. S. Selopal, B. A. Gonfa, L. Jin, A. Soudi, D. Cui, F. Enrichi, M. M. Natile, I. Concina, D. Ma, A. O. Govorov, F. Rosei, and A. Vomiero, "Controlling Photoinduced Electron Transfer from PbS@CdS Core@Shell Quantum Dots to Metal Oxide Nanostructured Thin Films", Nanoscale, Vol. 6, No. 12, (2014), pp. 7004-11.

[4] T. Mohammed-Brahim, M. Sarret, D. Briand, K. Kis-Sion, L. Haji, O. Bonnaud, D.Louër and A. Hadjadj, "Effect of the starting amorphous structure on the solid phase crystallization of silicon", Philosophical Magazine, Vol. 76, No. 2, (1997), pp.193-212.

[5] Z. Sun, Z. Liu, J. Li, G. A. Tai, S. P. Lau, and F. Yan, "Infrared Photodetectors Based on CVD-Grown Graphene and PbS Quantum Dots with Ultrahigh Responsivity", Advanced Materials, Vol. 24, No. 43, (2012), pp. 5878-83.

[6] R. Wang, Y. Zhang, H. Wang, X. Song, L. Jin, and J. Yao, “Wide Spectral Response Field Effect Phototransistor Based on Graphene-Quantum Dot Hybrid”, IEEE Photonics Journal, Vol. 7, No. 2, (2015), pp. 1-1.

[7] C. P. Ho, P. Pitchappa, P. Kropelnicki, J. Wang, Y. Gu, and C. Lee, “Development of Polycrystalline Silicon Based Photonic Crystal Membrane for Mid-Infrared Applications.”, IEEE Journal of Selected Topics in Quantum Electronics, Vol. 20, No.4, (2014), p. 4900107.

[8] J. M. Serra, R. Gamboa, A. M. Vallera, “Opical Absorption Coefficient of Polycrystalline Silicon with very High Oxygen Conten.” Materials Science and Engineering, Vol. 36, No. 1-3, (1996), pp. 73-76.

[9] D. Zhang, L. Gan, Y. Cao, Q. Wang, L. Qi, and X. Guo, “Understanding Charge Transfer at PbS-Decorated Graphene Surfaces toward a Tunable Photosensor”, Advanced Materials, Vol. 24, No. 20, (2012), pp. 2715-20.

[10] D. Padilla, G. Zhai, A. J. Breeze, D. Zhang, G. B. Alers, and S. A. Carter, “Thermal Properties of TiO2/PbS Nanoparticle Solar cells.”, Nanomaterials and Nanotechnology, Vol. 2, (2012), pp. 1-5.

[11] J. A. Aranovich, D. Golmayo, A. L. Fahrenbruch, and R. H. Bube, 'Photovoltaic Properties of Zno/Cdte Heterojunctions Prepared by Spray Pyrolysis', Journal of Applied Physics, Vol. 51, No. 8, (1980), pp. 4260-8.

[12] K. Preston, Y. H. D. Lee, M. Zhang, and M. Lipson, “Waveguide-integrated telecom-wavelength photodiode in deposited silicon.”, Optics Letters, Vol. 36, No. 1, (2001), pp. 52-54

[13] P. Martyniuk, and A. Rogalski, “Quantum-Dot Infrared Photodetectors: Status and Outlook”, Progress in Quantum Electronics, Vol. 32, No. 3-4, (2008), pp. 89-120.

[14] Z. Wang, Ü. Sakoğlu, S. Annamalai, N. Weisse-Bernstein, P. Dowd, J. S. Tyo, M. M. Hayat, S. Krishn, “Real-time implementation of matched filtering algorithms using

adaptive focal-plane array technology", Proceeding of SPIE, Vol. 5546, (2004), pp. 73-83.

[15] D. Kufer, I. Nikitskiy, T. Lasanta, G. Navickaite, F. H. Koppens, and G. Konstantatos, "Hybrid 2d-0d Mos2 -Pbs Quantum Dot Photodetectors", Advanced Materials, Vol. 27, No. 1, (2015), pp. 176-80.

[16] L. H. Zeng, M. Z. Wang, H. Hu, B. Nie, Y. Q. Yu, C. Y. Wu, L. Wang, J. G. Hu, C. Xie, F. X. Liang, and L. B. Luo, "Monolayer Graphene/Germanium Schottky Junction as High-Performance Self-Driven Infrared Light Photodetector", ACS Applied Materials & Interfaces, Vol. 5, No. 19, (2013), pp. 9362-6.

[17] S. W. Shin, K. H. Lee, J. S. Park, and S. J. Kang, "Highly Transparent, Visible-Light Photodetector Based on Oxide Semiconductors and Quantum Dots", ACS Applied Materials & Interfaces, Vol. 7, No. 35, (2015), pp. 19666-71.

[18] Y. Zhang, X. Song, R. Wang, M. Cao, H. Wang, Y. Che, X. Ding, and J. Yao, "Comparison of Photoresponse of Transistors Based on Graphene-Quantum Dot Hybrids with Layered and Bulk Heterojunctions", Nanotechnology, Vol. 26, No. 33, (2015), p. 335201.

Conclusion

This thesis fully uses quantum dots' (QDs) unique optical-electrical properties, for example, quantum confinement, size-tunable and photoconductivity effects. It can be combined with the self-amplifying and integration intrinsic characters of the transistors to fabricate phototransistors. In particular, with the development of QDs' chemical synthesis, easy solution processes can be utilized, which is feasibly compatible with all the present microelectronic technologies and with new flexible electronics technologies. In this thesis, we researched the factors affecting device performances, for instance, materials' optical spectrum, electrical parameters, and optical-electrical converting properties. These experiments can be used to evaluate device's overall performances, explore device's physics and optimize the fabrication. The research achievements can be concluded as follows:

Firstly, for evaluating the performance of Low-Temperature-Poly-silicon (LTPS) TFT, we fabricated N-type LTPS TFT gated with inorganic SiO_2 insulator. The SiO_2 gated LTPS TFT has excellent electrical performances such as high on/off ratio (~10^6), small subthreshold slope (0.65 V/Dec) and high mobility (13 $cm^2\ v^{-1}s^{-1}$). Afterward, this LTPS TFT is also explored in deep with organic SU8 insulator which can be functioned as the future photo-sensing hybrid insulator. The SU8 insulator already provides an excellent insulating property (1 nA leakage current). Moreover, using SU8 as gate insulator, TFTs present enough mobility (3.1 cm^2/Vs), stable electrical characteristics, reasonable on/off current ratio (~10^{-5}) and low subthreshold slope (3.2 V/Dec). Then SU8 will be an alternative gate insulator for LTPS TFT's.

Secondly, the hot injection synthesis method was employed in this thesis to fabricate PbS QDs with 5.5 nm diameter which have uniform size, are well dispersed in the solution. Moreover, obvious absorption peak in the IR waveband was detected. We point out that the surface passivation of the PbS QDs will influence the carrier transfer in the nano-composite. The characters of PbS QDs with different ligands (pyridine, OA, TOPO and PANI) were also researched. The short chain pyridine ligand with better conductivity was chosen for providing efficient charge transfer between PbS

QDs and SU8 insulators. In addition, the IR absorbance of QDs alone, SU8 alone and the mixture of QDs and SU8 was measured. The presence of hybrid material's absorbance with weaker amplitude indicates that there are charges' transfer process between QDs and SU8 interface.

Afterward, MIS devices with different concentrations of QDs inside the SU8 insulator were characterized. 2.5 mg/ml concentration of QDs was chosen an optimum mean between high photosensitivity and low leakage current inside the insulator. At this concentration, the leakage dark current is 10 nA with 0.1 mm^2 area of the MIS structure. Considering the channel area of the fabricated TFTs, the leakage current of the TFTs can be in the order of 100-500 pA.

Finally, TFTs were fabricated and characterized by using 2.5 mg/ml QDs diluted in SU8 as gate insulator. Remarkably, high responsivity can be obtained for N-type TFT reaching 1800 A/W at 760 nm. More important is the not negligible responsivity at 1.3 μm that reaches 13 A/W, implying a broad detecting ability in IR waveband. For better exploring the device physics, two very thin carrier-injection block layers (150 nm thick SU8 or 15 nm thick SiO_2) between channel and hybrid insulator were deposited forming two sandwich structures' devices. These insulating block layers diminished the photosensitivity at near infrared wavelength. This means that the photosensitivity is not due to a charge accumulation inside the gate insulator but really a charge injection from the insulator to the channel.

Moreover, when exposed to the incident pulsed IR photo signal, the answer time of this phototransistor can reach 46 ms for rise time and only 10 ms for recovery time. The answer time of average 50 ms will lead to conclude that present photo-TFTs can answer to less than 1 s pulse and then to a frequency higher than 1 Hz. As for another important parameters, the detectivity of the N-type TFT device is as high as 1×10^{13} Jones. This high specific detectivity is useful when detecting low light intensity. The detectivity of N-type TFTs is at the level of highest detectivity values already published.

Perspective

In this thesis, we fabricated NIR phototransistors with QDs embedded in the SU8 gate insulator and analyze deeply their electrical and detecting properties. The understanding of their functioning together with the encouraging experimental results conduct to propose some ways to improve the properties:

(1) Due to the bad contact between organic SU8 insulator and inorganic Si active layer, the surface of silicon can be functionalized before depositing the organic gate insulator. Other organic or inorganic semiconductors, more compatible with SU8, can replace silicon. Other than SU8 deposited in solution organic insulators can be checked also. Interestingly is the use of solution deposited insulator will provide large number of possibilities to improve the results.

(2) Present phot-TFTs have to be integrated with other devices leading to functional circuit.

(3) Finally, present NIR range of detection can be enlarged by using other QDs using the main idea developed in this work: embedding QDs in solution deposited gate insulator.

Résumé en Français

Dans le développement actuel de la technologie de l'information, les photo-détecteurs dans le domaine de l'infrarouge ont un rôle vital dans de nombreuses applications telles que l'opto-communication, le contrôle, l'imagerie infra-rouge et la navigation.

Les photo-détecteurs IR conventionnels utilisent des matériaux de grande consommation énergétique et une connexion très complexe de différents composants. Les nouveaux matériaux constitués de nano-particules (Quantum Dots ou QDs) avec leur propriétés particulières, dues à l'effet de taille, attirent un grand nombre de convoitises.

D'un autre côté, la structure de transistor à effet de champ (Field Effect Transistor ou FET), par son avantage d'amplification propre, peut offrir l'intérêt de regrouper dans un même composant la détection de la lumière et l'amplification du signal de détection.

Ce regroupement constitue l'objectif premier de ce travail de thèse. Un phototransistor utilisant des nanoparticules pour la détection, intégrées dans une structure transistor, est conçu, fabriqué et caractérisé. Un modèle de fonctionnement est établi en conséquence.

Une description schématique est donnée en figure 1.

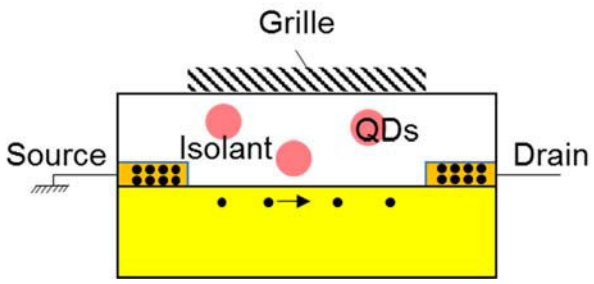

Figure 1. Description schématique d'un phototransistor à structure FET utilisant des nanoparticules (QDs) pour la détection de lumière.

La structure habituelle d'un transistor en couche mince (TFT) dite LTPS (Low-Temperature Polysilicon et utilisée couramment pour l'adressage actif de points image (pixels) d'un écran plat est prise ici comme structure de base du phototransistor. La

structure particulière prise ici est dite « Top-Gate, Top-Contact ». Le contact de grille et les contacts de drain et de source sont placés au-dessus de l'isolant et au-dessus de la couche de canal respectivement. Le dopage N ou P des régions de source et de drain définit le type N, transport d'électrons entre source et drain, ou P, transport de trous entre source et drain, TFT.

L'isolant utilisé habituellement est l'oxyde de silicium (SiO_2) qui est l'oxyde naturel du silicium et qui forme donc une interface presque sans défauts avec le silicium.

Le but de la thèse étant de transformer ce TFT en phototransistor détectant une lumière infrarouge grâce à des nanoparticules intégrées, une des manières considérée ici est de les intégrer dans l'isolant. Pour cela, un isolant pouvant être déposé liquide a été choisi dans ce but. Cette particularité permet de mélanger les nanoparticules avec l'isolant en solution et de déposer la solution mixée. Un isolant organique constitué d'une photorésine dite SU8 et qui a montré par ailleurs des propriétés d'isolant de grille de transistor intéressantes, a été choisi.

Ses propriétés d'isolant de grille ont été vérifiées en fabriquant 2 transistors similaires différentiés uniquement par leur isolant de grille. Pour l'un une couche habituelle de SiO_2 a été utilisé et pour l'autre cette couche de SiO_2 est remplacée par une couche de SU8 déposée en solution. La figure 2 montre les caractéristiques de transfert de ces 2 transistors.

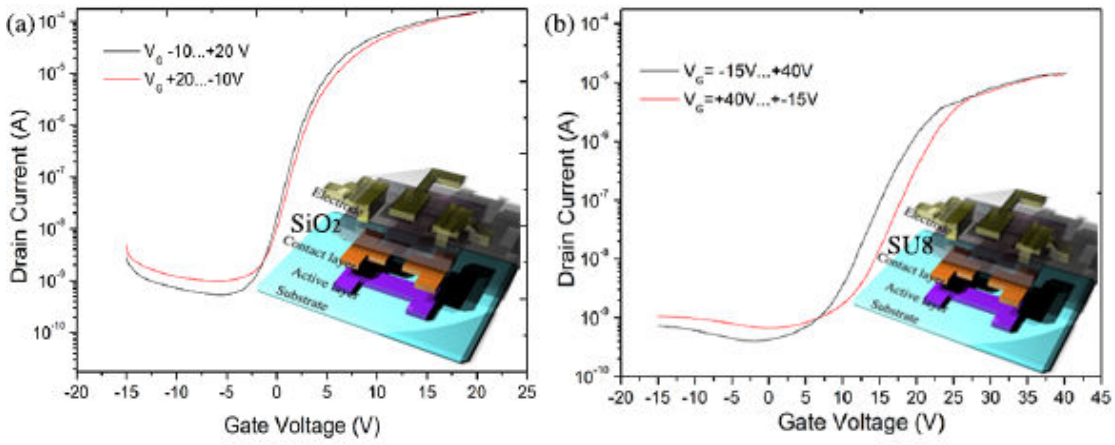

Figure 2. Caractéristiques de Transfert d'un TFT avec SiO_2 comme isolant de grille (a) et d'un TFT utilisant un isolant organique SU8 (b).

Les paramètres du transistor avec SiO_2 déterminés à partir de la caractéristique de transfert donnent une mobilité d'électrons de 13 cm^2/Vs, un rapport courant direct sur courant inverse de 10^6, une pente sous le seuil de 0.67V/De cet une tension de seuil de 5.5 V. Les paramètres du TFT avec SU8 sont moins bons comme attendu à partir de la plus mauvaise interface SU8-silicium. La mobilité d'électrons est de 3.1 cm^2/Vs, le rapport courant direct sur courant inverse de 10^5, la pente sous le seuil de 3.2V/Dec et et la tension de seuil de 20 V. Le transistor ne devant pas être utilisé pour ses performances électroniques mais pour sa capacité à détecter une lumière infrarouge avec suffisamment de sensibilité et de rapidité, ces paramètres peuvent s'avérer suffisants même si de meilleurs auraient été plus intéressants. Une des perspectives de ce travail de thèse est d'améliorer les performances électroniques comme nous le verrons plus tard.

Pour la detection de lumière dans le proche infrarouge, des particules de PbS (sulfure de plomb) de diamètre convenable ont été choisies. Elles ont été synthétisées lors d'une étape d'optimisation par la méthode chimique d'injection chaude et d'échange de ligand. La figure 3(a) montre que les nanoparticules sont sphériques avec un diamètre uniforme et sont bien dispersées dans la solution. La figure 3(c) montre

une analyse EDS de la composition d'une couche de particules déposées sur une plaquette de silicium oxydée. Ces figures montrent qu'on peut bien déposer une couche de nanoparticules en solution par « spin-coating ».

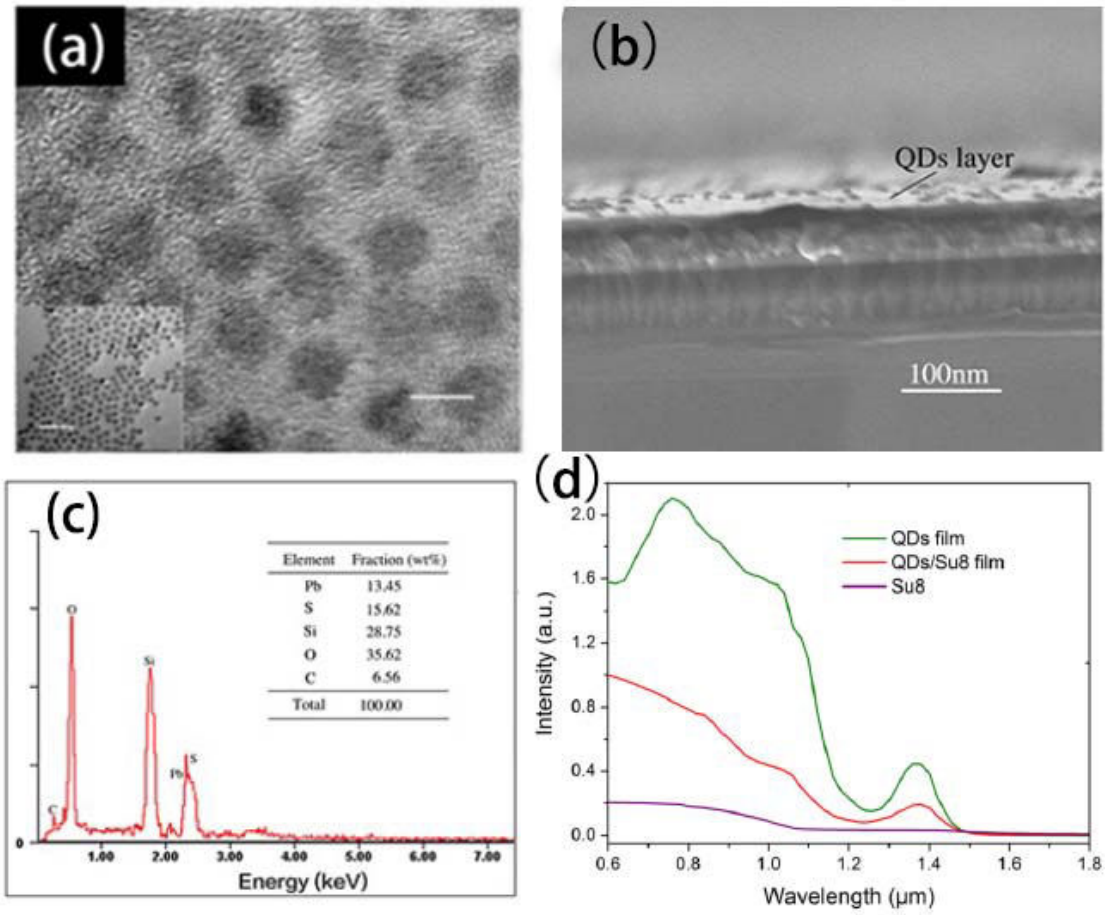

Figure 3. Caractérisation de couches contenant des nanoparticules. (a) Image par Microscope Electronique à Transmission de Haute resolution (HRTEM) barre d'échelle: 5nm (et 20nm pour l'insert). (b) Image de la tranche d'une couche de nanoparticules déposée sur silicium oxydé. (c) Composants de la structure determinés par EDS. (d) Absorbance de couches de nanoparticules, nanoparticules seules, mélange nanoparticules/SU8, et SU8 seule.

Enfin, la figure 3(d) montre le spectre d'absorption de couches de SU8 seule, de nanoparticules seules et de particules mélangées à la SU8. Ces couches sont déposées sur verre pour mesurer la transmission optique et en déduire l'absorption. L'absorption de la couche mixée décroit dans le visible vers l'infrarouge mais présente une bande d'absorption centrée sur 1300nm, typique de l'absorption de particules de PbS de diamètre de 5nm.

La figure 4 présente les spectres de photoluminescence (PL) résolue en temps pour ces 3 couches. La décroissance de la luminescence peut être exprimée par une fonction exponentielle $\mathrm{I}(t) = \mathrm{Aexp}\left(-\frac{\mathrm{t}}{\tau}\right) + \mathrm{B}$.

La pente de la décroissance permet de calculer le temps τ qui est égal 1.65ns, 1.35ns et 0.21ns pour les couches de nanoparticules seules, de particules mélangées à la SU8 et de SU8 seule respectivement. Le temps pour la couche mixée très légèrement inférieur à celui de nanoparticules seules montrent le bon transfert de charges ente les nanoparticules et la SU8.

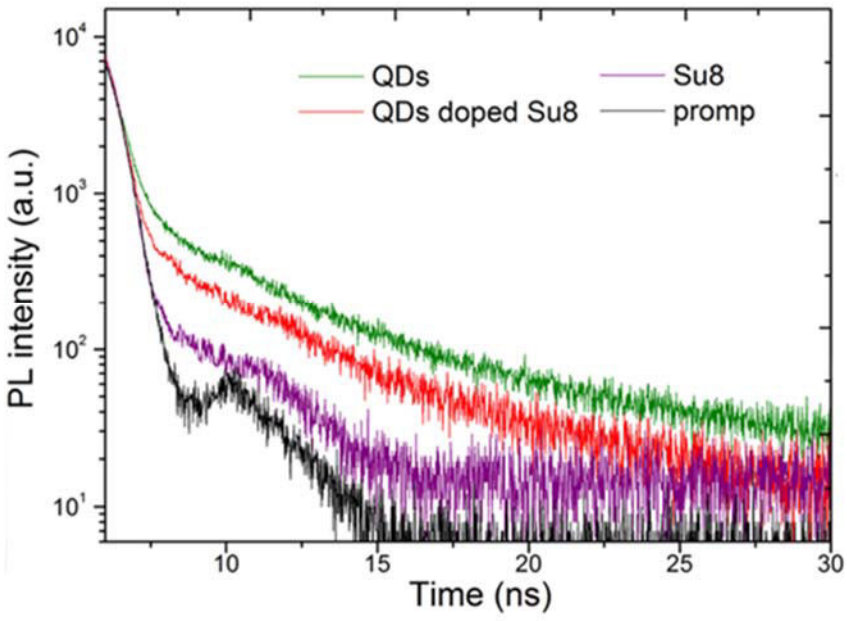

Figure 4. Courbes de décroissance de la photoluminescence (PL) des couches de

nanoparticules seules (QDs), de particules mélangées à la SU8 (QDs doped SU8) et de SU8 seule (SU8).

Après la synthèse et la caractérisation de la couche mixée, une caractérisation électrique de ses propriétés d'isolation électrique a été menée. Il est en effet important que cette couche jour pleinement son rôle d'isolant de grille même en présence de lumière absorbée. Pour cela des structures Metal-Isolant-Semiconducteur (couche transparente de ZnO servant comme électrode-couche mixée QDs/SU8-silicium monocristallin) ont été fabriquées et caractérisées. Des couches mixées issues de solution contenant différentes concentration de nanoparticules ont été utilisées comme isolant dans ces structures MIS. La figure 5(a) montre la variation du courant circulant dans la structure MIS en fonction de la concentration de nanoparticules en l'absence de lumière. La figure 5(b) donne la photosensitivité de cette structure pour une lumière de longueur d'onde 0.85µm et d'intensité 0.2 mW/cm^2. La photosensitivité est définie par le rapport de la différence entre le courant sous lumière et le courant à l'obscurité (I_{light}-I_{dark}) et le courant à l'obscurité (I_{dark}).

Quand la concentration de nanoparticules augmente, le courant en l'absence de lumière reste constant et faible jusqu'à 1.5 mg/ml. Le courant augmente ensuite à partir de cette concentration, atteignant 16 nA à 3 mg/ml. Sous lumière le courant ne devient supérieur au courant d'obscurité seulement si la concentration est supérieure à 1.5 mg/ml. La photosensitivité est ainsi pratiquement nulle avant 1.5 mg/ml. Elle augmente aux plus grandes concentrations.

Pour expliquer l'augmentation du courant sous obscurité à des concentrations supérieures à 1.5 mg/ml, nous pouvons invoquer la possibilité d'un effet tunnel de porteurs de charges entre nanoparticules séparées par la SU8. Aux concentrations supérieures à 1.5mg/ml, la devient suffisamment faible induisant une augmentation sensible de la probabilité de passage par effet de tunnel.

Dans la suite du travail, nous avons choisi une concentration de 2.5mg/ml pour profiter d'une bonne sensibilité à la lumière sans trop augmenter le courant de fuite à travers l'isolant.

Des transistors de type N et de type P ont été fabriqués avec un isolant de grille constitué d'une couche mixée QDs/SU8 obtenue à partir d'une solution contenant 2.5 mg/ml nanoparticules. Leurs caractéristiques de transfert sous obscurité et sous lumière à différentes longueurs d'onde sont présentées dans la figure 6. Les responsivités calculées sont données dans la figure 7. La responsivité caractérise la capacité du détecteur à transformer une lumière en un courant. Elle est définie comme le rapport du courant sous lumière à l'intensité de la lumière.

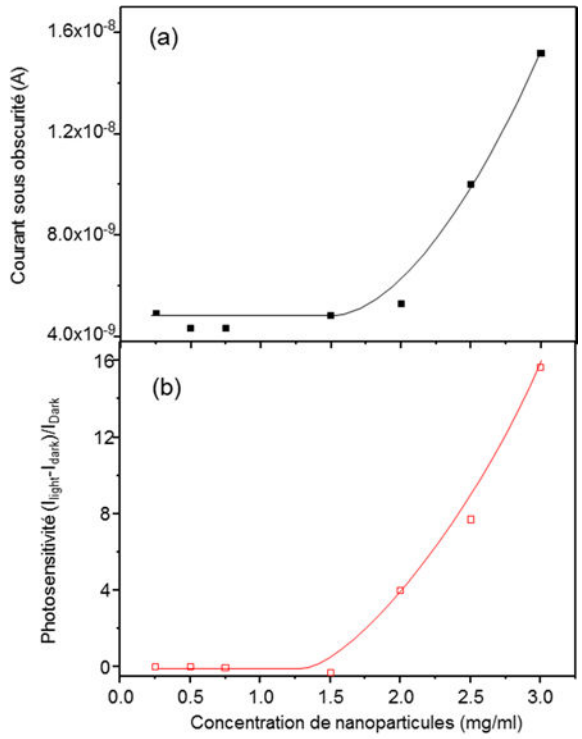

Figure 5. Variation du courant circulant dans la structure MIS en fonction de la concentration de nanoparticules en l'absence de lumière (a) Photosensitivité de cette structure pour une lumière de longueur d'onde 0.85µm et d'intensité 0.2 mW/cm^2 (b).

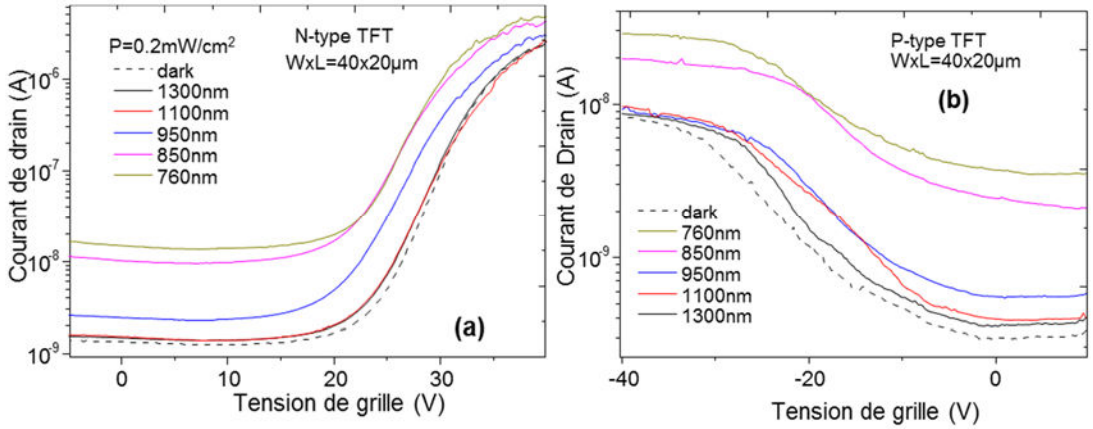

Figure 6: Caractéristiques de transfert de transistors de type N et de type P sous obscurité et sous lumière à différentes longueurs d'onde.

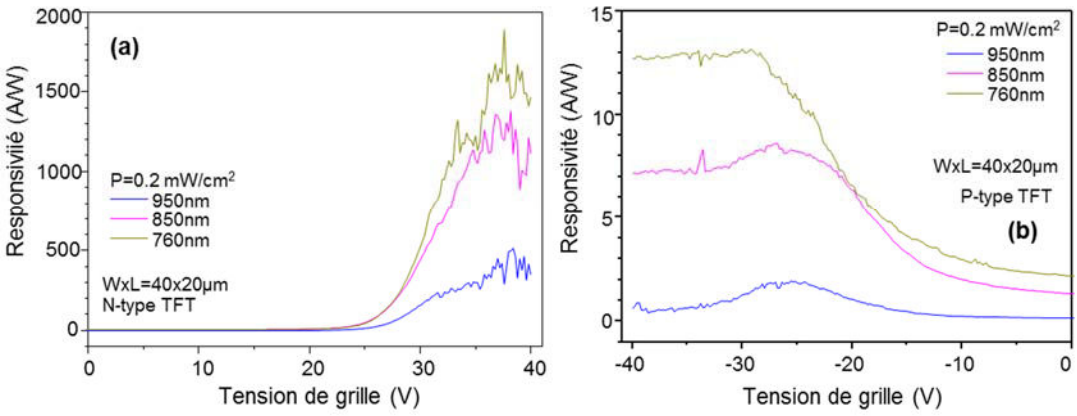

Figure 7: Responsivités des transistors de type N et de type P à la lumière à différentes longueurs d'onde.

Du fait de l'efficacité d'absorption par les nanoparticules et du bon transfert de charge, une responsivité de 1800 A/W est obtenu à 760 nm et est même non négligeable, 13 A/W, à 1300nm.

Afin de comprendre le phénomène aboutissant à cette bonne responsivité, nous pouvons invoquer 2 possibilités. La première consiste en une séparation des charges

photogénérées par le champ de grille et leur piégeage dans l'isolant. L'apparition d'une charge fixe dans l'isolant change la tension de seuil du transistor amenant une variation du courant de drain.

L'autre possibilité est l'injection des charges photogénérées directement dans le canal, augmentant ainsi le courant de drain.

Afin de privilégier une des 2 voies, des transistors identiques aux précédents ont été fabriqués. Ils comportent en plus une couche isolante de 150nm de SU8 sans nanoparticules ou une couche de très fine de 15 nm de SiO_2 entre le canal et la couche mixée SU8/nanoparticules. Ces transistors n'ont montré aucune sensibilité à la lumière infrarouge. L'effet de charges piégées dans l'isolant sans injection dans le canal a pu ainsi être écarté. Seule une injection directe de charges dans le canal est responsable de la responsivité des transistors.

Le schéma de bandes d'énergie donné dans la figure 8 montre bien la possibilité de porteurs de charges photogénérés dans les nanoparticules et passant par effet tunnel assisté par le champ électrique de grille d'une nanoparticule à la voisine et atteignant le canal pour participer au courant de drain.

Le schéma descriptif de la structure des TFTs de type N et de type P polarisés en direct ou en inverse explique bien le principe de détection par ces transistors/

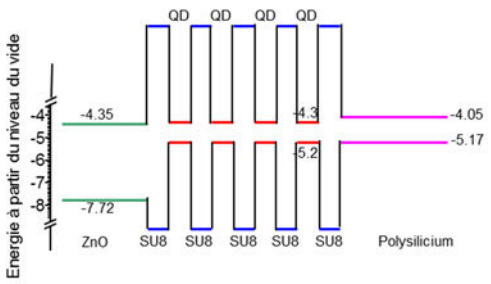

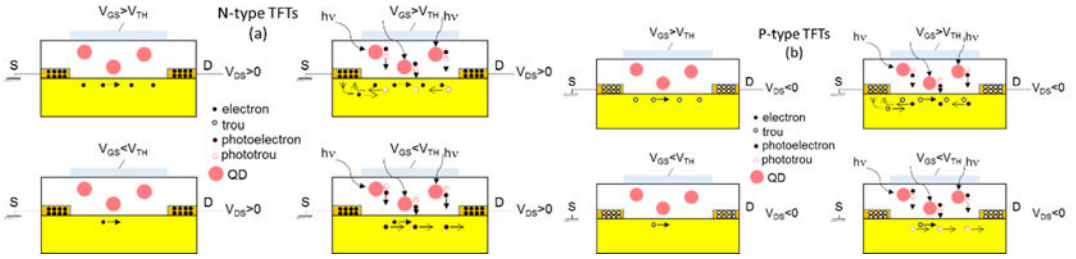

Figure 8 : Schéma de bandes d'énergie entre le contact grill (ZnO) et le silicium polycristallin et Schéma descriptif des transistors de type N et de type P montrant le principe de détection de la lumière quand ils sont polarisés en direct ou en inverse.

En dernière partie de cette thèse, la réponse de ces transistors à une lumière pulsée a été étudiée. La figure 9 montre leur réponse à un pulse de lumière de 850 nm de longueur d'onde et de 1.5 s de durée. Le temps de montée est de 46 ms pour le type N et de 36 ms pour le type P. temps de descente est de 10 ms pour le type N et 70 ms pour le type. Le temps de réponse de 50 ms montre que ces phototransistors répondent à une impulsion de lumière de 1s et donc à une fréquence supéreure à 1Hz.

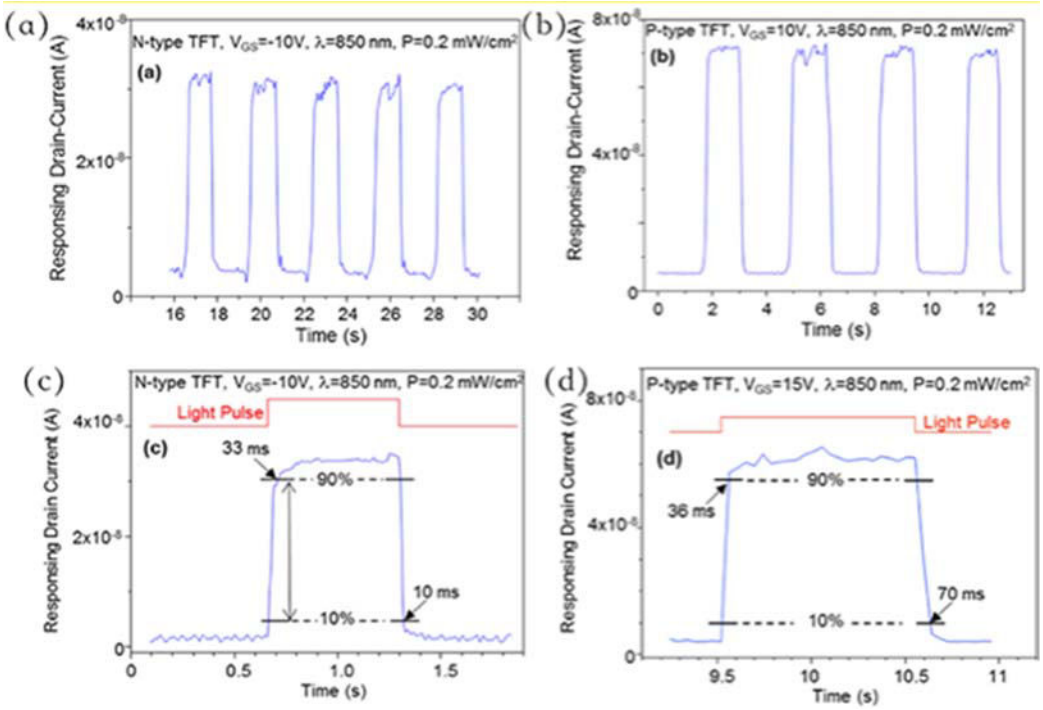

Figure.9 Réponse des TFTs de type N (a) et de type P (b) TFTs à une lumière pulsée de période 1.5 s. La réponse à une impulsion est donnée en (c) et en (d) pour le type P.

En résumé un procédé simple de fabrication d'un photodétecteur de lumière proche infrarouge a été mis au point. Le photodétecteur a montré des propriétés de détection très intéressantes avec une grande photo-responsivité et ue réponse rapide . De plus, le procédé est compatible avec toutes les technologies microélectroniques actuelles. Il peut être introduit directement dans les procédés de fabrication actuels.